

**Effect of radiation and co-culture with fibroblasts on  
growth characteristics and invasiveness of 3D  
breast cancer models**

Dissertation zur Erlangung des Naturwissenschaftlichen Doktorgrades „Dr.rer.nat.“ der  
Fakultät für Biologie der Ludwig-Maximilians-Universität München



Jia Mei

München, 2022

Diese Dissertation wurde angefertigt  
im Bereich von unter der Leitung von PD Anna A. Friedl  
an der Klinik und Poliklinik für Strahlentherapie und Radioonkologie des Klinikums der  
Ludwig-Maximilians-Universität München

Ersgutachter/in: PD Dr. Anna A. Friedl  
Zweitgutachter/in: Prof. Dr. Heinrich Leonhardt

Tag der Abgabe: 10.02.2022

Tag der mündlichen Prüfung: 28.11.2022

### **EIDESSTATTLICHE RKLÄRUNG**

Ich versichere hiermit an Eides statt, dass meine Dissertation selbständig und ohne unerlaubte Hilfsmittel angefertigt worden ist.

Die vorliegende Dissertation wurde weder ganz, noch teilweise bei einer anderen Prüfungskommission vorgelegt.

Ich habe noch zu keinem früheren Zeitpunkt versucht, eine Dissertation einzureichen oder an einer Doktorprüfung teilzunehmen.

München, den

10.02.2022

Jia Mei

# Tables of Contents

Tables of Contents.....	III
Publications.....	VI
Abstract.....	VII
Zusammenfassung.....	VIII
1. Introduction.....	1
Mammary carcinoma .....	1
Treatment strategy of breast cancer in clinic .....	2
DNA repair mechanism .....	3
Tumor micro-environment.....	5
Three-dimensional (3D) culture of cells .....	7
EMT transition.....	10
Migration, invasion and metastasis.....	10
<i>Migration</i> .....	11
<i>Invasion</i> .....	12
<i>Traditional Assay for migration and invasion</i> .....	13
Metabolism and Mitochondria.....	14
<i>Structure of Mitochondria</i> .....	14
<i>Function of Mitochondria</i> .....	15
Fluorescence microscopy and two-photon excitation fluorescence (TPEF).....	17
Fluorescence life-time imaging microscopy (FLIM).....	19
Tasks of my research .....	22
2. Material.....	24
2.1 Cell lines .....	24
2.2 Plasmids .....	25
2.3 Cell culture materials .....	26
2.4 X-ray irradiation.....	27
2.5 Western Blot .....	27
2.6 Immunofluorescence staining .....	29
2.7 HE staining assay.....	30
2.8 Invasion Assay .....	30
2.9 Mitochondria staining Assay .....	31
2.10 Investigation of metabolism dynamic by FLIM microscopy.....	31
2.11 NSC treatment assay .....	32
2.12 Microscopy .....	32
A. Fluorescent Microscopes: .....	32

B. Two-photon excitation FLIM Microscopy: .....	34
2.13 Data Analysis Software.....	34
3. Methods.....	36
3.1 Cell culture 2D.....	36
3.2 Cell culture 3D.....	38
3.3 Invasion of fibroblasts into cancer cell spheroids.....	40
3.4 Invasion into invasion matrix.....	42
3.5 Foci counting assay .....	43
3.6 Cryosection of mammary carcinoma cell spheroids and HE staining .....	44
3.7 Immunofluorescence staining of 2D tissue culture.....	45
3.8 Western Blot .....	46
3.9 Mitochondria staining assay .....	48
3.10 Investigation of metabolic state by multi-model microscopy.....	49
3.11 Data Analysis .....	51
3.11.1 Analysis of size of spheroids.....	51
3.11.2 Analysis of invasion area .....	52
3.11.3 Analysis of Invasion distance radius .....	53
3.11.4 Analysis of FLIM images with SPCImage .....	55
3.11.5 Analysis of Mitochondrial morphology .....	56
4. Results.....	57
4.1 Characterization of growth characteristics of mammary carcinoma cell lines MCF-7, BT474, MDA-MB-231 and SkBr3 .....	57
4.1.1 Different morphology of mammary carcinoma lines cultured in 2D ...	57
4.1.2 Different morphology of mammary carcinoma lines cultured in 3D ...	58
4.1.3 Western Blot detection of EMT marker proteins in 2D and 3D cultured mammary carcinoma cells .....	62
4.1.4 Invasiveness of breast cancer cell lines into a basal membrane-like matrix .....	64
4.2 Characterization of spheroids obtained by co-culture of breast cancer cells and fibroblasts.....	65
4.2.1 Characterization of BJ1-hTert foreskin or HDF skin fibroblasts.....	66
4.2.2 Morphology and growth of fibroblast lines cultured in 3D .....	67
4.2.3 Characterization of spheroids obtained by coculture of breast cancer cells with BJ1-hTert or HDF fibroblasts in 3D ULA plates.....	68
4.3 Radiation effects on growth of breast cancer cell monoculture and in coculture spheroids .....	70
4.3.1 Radiation effects on spheroid size .....	70
4.3.2 Repair of double-strand breaks in MCF-7 monoculture and MCF-7 +	

BJ1-hTert coculture 3D spheroids .....	74
4.4 Migration of fibroblasts into mammary carcinoma spheroids .....	76
4.4.1 Migration of fibroblasts into MCF-7 and BT474 spheroids .....	76
4.4.2 The effects of ROCK-inhibitor on the migration behavior of fibroblasts .....	83
4.4.3 The radiation effects on the migration behavior of fibroblasts .....	85
4.5 Fibroblast-mediated invasion of mammary carcinoma cells .....	88
4.5.1 Low- and high-resolution imaging of fibroblast-led invasion model ...	88
4.6 Radiation effects on fibroblast-led invasion .....	91
4.6.1 Radiation effects on the number of invading cells.....	91
4.6.2. Radiation effects on invasion distance.....	93
4.6.3 Sensitivity to DSB induction by NCS treatment in BJ1-hTert and HDF fibroblasts.....	96
4.7 Investigation of invasion and radiation effects with non-linear optical methods – proof of concept studies .....	99
4.7.1 Investigation of the collective invasion model by FLIM.....	100
4.7.2 Radiation effects on NAD(P)H and FAD fluorescence lifetime.....	102
4.7.3 Radiation effects on mitochondrial morphology .....	107
5. Discussion.....	116
5.1 Choosing of 3D cell culture methods.....	116
5.2 EMT marker expression vs. features of 3D spheroids .....	117
5.3 Influence on carcinoma cell lines of co-culture with normal fibroblasts.....	119
5.4 Dosages of radiation treatment .....	121
5.5 New methods for estimating proliferation of spheroids and invasion in 3D model.....	121
5.6 Imaging of 3D structures .....	122
5.7 Imaging of NAD(P)H and FAD.....	123
6. Prospects .....	125
7. Reference .....	127
8. Abbreviation.....	138
9. List of figures and tables.....	140
9.1 Figures.....	140
9.2 Table .....	143
10. Appendix .....	144
10.1 Phasor plots of FLIM data on radiation effects .....	144
10.2 Migration Movie .....	147

## Publications

Parts of the work are published in:

Jia Mei, Claudia Böhland, Anika Geiger, Iris Baur, Kristina Berner, Steffen Heuer, Xue Liu, Laura Mataite, M. Camila Melo-Narváez, Erdem Özkaya, Anna Rupp, Christian Siebenwirth, Felix Thoma, Matthias F. Kling & Anna A. Friedl (2021): Development of a model for fibroblast-led collective migration from breast cancer cell spheroids to study radiation effects on invasiveness.

In *Radiation Oncology*, 16, Article number: 159 (2021).

DOI: [doi.org/10.1186/s13014-021-01883-6](https://doi.org/10.1186/s13014-021-01883-6)

## **Abstract**

Invasiveness is a major factor contributing to cancer metastasis. Given the broad variety and plasticity of invasion mechanisms, assessing potential metastasis-promoting effects of irradiation for specific mechanisms is important for further understanding of potential adverse effects of radiotherapy. Previous investigations of radiation effects on invasion were mainly done by 2D methods that cannot differentiate different invasion mechanisms. In fibroblasts-led collective invasion mechanisms, fibroblasts degrade the extracellular matrix and produce tracks for cancer cells with epithelial traits to follow. A major goal of the present work was to establish a model for this invasion mechanism and to study the effect of radiation on it.

After verifying their epithelial-like, non-invasive characteristics, breast cancer cells (MCF-7 and BT474) were co-cultured in ultra-low adhesion plates with human normal fibroblasts (BJ1-hTert and HDF). Cocultivation with fibroblasts had little effects on spheroid growth, radiation-induced growth delay and repair of DNA damage. Epithelial-like MCF-7 and BT474 cells gain ability to invade into matrix if cocultured with normal fibroblasts. High-resolution imaging showed features of fibroblast-led collective invasion. This new model was used to investigate radiation effects on invasiveness. Irradiation reduced the number of invading cells in models using BJ1-hTert, but not HDF. However, sensitivity to the radiomimetic drug neocarzinostatin was comparable in both fibroblast strains. Radiation had little effects on invasion distance, showing that with this model effects on number of invading cells and distance can be uncoupled. In conclusion, no invasion-promoting effect of irradiation could be found with this model.

In proof-of-concept studies, analysis of NAD(P)H and FAD autofluorescence via TPEF and FLIM was tested as tool for label-free differentiation of cancer cells and fibroblasts in 3D situations, including invasion experiments. In addition, preliminary FLIM data suggest that MCF-7 cells undergo a transient metabolic shift towards oxidative phosphorylation after irradiation, which could be verified by mitochondrial staining experiments.

## Zusammenfassung

Invasivität ist ein Hauptfaktor bei der Metastasierung von Krebszellen. Angesichts der vielen unterschiedlichen und plastischen Invasionsmechanismen ist es wichtig, mögliche Metastase-fördernde Effekte von Strahlenbehandlung für spezifische Invasionsmechanismen zu untersuchen, um mögliche schädliche Einflüsse von Strahlentherapie besser zu verstehen. Bisher wurden Strahleneffekte auf Invasivität hauptsächlich mit 2D-Methoden untersucht, die nicht zwischen verschiedenen Mechanismen unterscheiden können. Bei der Fibroblasten-geführten kollektiven Invasion degradieren Fibroblasten die extrazelluläre Matrix und bilden Kanäle, in welchen Krebszellen mit epithelialen Eigenschaften folgen können. Hauptziel der vorliegenden Arbeit war die Etablierung eines Modells für Fibroblasten-geführte kollektive Invasion und die Untersuchung von Strahleneffekten auf dieses Modell.

Nach Verifizierung ihrer epithelialen, nicht-invasiven Eigenschaften wurden die Brustkrebslinien MCF-7 und BT474 in *ultra-low adhesion* Zellkulturplatten mit normalen Fibroblasten (BJ1-hTert und HDF) kokultiviert. Die Kokultur mit Fibroblasten hatte nur wenig Einfluss auf Sphäroidwachstum, strahleninduzierte Wachstumsverzögerung und Reparatur von DNA-Schäden. Epithel-ähnliche MCF-7- und BT474-Zellen erlangen bei Kokultur mit normalen Fibroblasten die Fähigkeit zur Invasion in Matrix. Mittels hochauflösender Mikroskopie wurden Eigenschaften von Fibroblasten-geführter kollektiver Invasion nachgewiesen. Dieses neue Invasionsmodell wurde dann genutzt, um Strahleneffekte zu untersuchen. Bestrahlung verringerte die Anzahl invadierender Zellen in Modellen mit BJ1-hTert, aber nicht mit HDF. Die Empfindlichkeit gegenüber der radiomimetischen Substanz Neokarzinostatin unterschied sich jedoch nicht in beiden Fibroblasten-Stämmen. Strahlung hatte kaum Effekte hinsichtlich der Invasionsdistanz, was zeigte, dass Anzahl invadierender Zellen und Invasionsdistanz mit diesem Modell entkoppelt werden können. Insgesamt konnte in diesem Modell kein Invasions-fördernder Effekt von Bestrahlung gefunden werden.

In ersten proof-of-concept Studien wurde zudem untersucht, ob sich die Analyse von NAD(P)H- und FAD-Autofluoreszenz mittels TPEF und FLIM nutzen lassen kann, um markierungsfrei in 3D-Situation, inklusive Invasionsexperimenten, zwischen Tumorzellen und Fibroblasten zu unterscheiden. In vorläufigen FLIM-Experimenten wurde zudem eine transiente metabolische Verlagerung hin zu oxidativer Phosphorylierung in MCF-7-Zellen beobachtet, welche durch Mitochondrienfärbung bestätigt werden konnte.

# **Effect of radiation and co-culture with fibroblasts on growth characteristics and invasiveness of 3D breast cancer models**

## **1. Introduction**

### **Mammary carcinoma**

Mammary carcinoma, also known as breast cancer, is the first ranking cancer threatening the health of women and the second most common cancer overall. Breast cancer occurrence was estimated to be around 2.7 million new cases, which alone accounts for thirty percent of female cancers, and 42 thousand deaths, according to the *cancer statistics 2020* (Siegel et al. 2020).

Using different ways of classification, breast cancer can be divided into different types, for example, based on location and aggressiveness. All breast cancers are tested for estrogen receptor (ER), progesterone receptor (PR) and human epidermal growth factor receptor (HER2) protein expression by immunohistochemistry methods. Based on expression patterns, four main subtypes are described: Luminal A, Luminal B, HER2-positive and triple negative/basal-like breast cancer (Eliyatkin et al. 2015). Among all invasive breast cancers, the Luminal A type (ER, PR positive and HER2 negative) dominates with 50 % of invasive breast cancers, and is characterized by expression of luminal cytokeratins, and high expression of hormone receptors and related genes. Compared to Luminal A type, Luminal B type (ER, PR positive and HER2 positive) shows a similar gene expression pattern and clinical and biologic properties, but higher proliferation and higher histologic grade than the Luminal A type. This type represents about 20 % of invasive breast cancers (Schnitt 2010). The third type, HER2-positive cancers, is characterized by high expression of HER2 and low expression of ER and related genes and shows high proliferation and histologic grade. Basal-like cancers are hormone-receptor negative and HER2 negative and show high

expression of basal epithelial markers and basal cytokeratin. These tumors, which are also known as triple negative type, exhibit high grade invasiveness, high proliferation and TP53 mutations and DNA repair defects e.g., BRCA1 dysfunction (Correa and Reis-Filho 2009). On the basis of molecular differences and biological properties, different types of breast cancer vary with respect to sensitivity to the treatment and prognosis, thus challenging the therapy. Therefore, the choice of therapy methods should be based on the pathological features of each individual case.

### **Treatment strategy of breast cancer in clinic**

Methods developed to reduce the death rate of breast cancer can be divided into 1) Local treatments including local surgery and radiation therapy; and 2) Systemic therapy, like chemotherapy, endocrine/hormone therapy, targeted therapy and immunotherapy, where the drug after oral or parenteral application can reach almost anywhere in the body (Palumbo et al. 2013).

Radiation therapy is a cancer treatment which uses high-energy ionizing radiation (photons or charged particles) to control or kill malignant cells and shrink tumor volumes. Its primary effect is the introduction of various lesions in the DNA of cancerous cells. Radiation is integral to the management of most cancer types (Atun et al. 2015) and is a standard in breast cancer therapy, especially after breast-conserving therapy or mastectomy. Overall, radiation therapy improves local control and patients' recurrence-free survival (Orth et al. 2014), but there are concerns that in some cases irradiation may contribute to increased aggressiveness of tumor cells. In particular, it has been suggested that radiotherapy may increase the metastatic potential of cells (Fujita et al. 2015) (Monchamont et al. 2014) (Blyth et al. 2018). Studying such effects of irradiation and finding proper models for investigation of radiation effects on tumor behavior is thus of highest interest in improving radiation therapy in general.

## DNA repair mechanism

Radiation can lead to various types of DNA damage. A large amount of evidence supports that double-stranded breaks (DSBs) of nuclear DNA confer the most important effects of cells upon radiation, as inaccurately repaired or unrepaired DSB can cause mutations and genomic rearrangements, including generation of lethal chromosomal aberrations, cell apoptosis, and eventually cell death (Willers et al. 2004).

In order to keep the integrity of the genome, cells possess DNA damage-induced checkpoint mechanisms during the cell cycle that inspect the genome for damage (Dasika et al. 1999). In eukaryotic cells, there are mainly three checkpoints: G1, G2/M and metaphase checkpoints (M checkpoint). Once the DNA damage is detected, the cell cycle is arrested and repair mechanisms are activated (Houtgraaf et al. 2006).

For repair of DSBs there are two principal pathways: homologous recombination (HR) and non-homologous end-joining (NHEJ). Due to its simplicity, NHEJ is an error-prone repair pathway which can occur in all cell cycle phases (Seluanov et al. 2004). HR maintains somatic genomic stability by promoting accurate repair of DSBs induced by ionizing radiation and other agents. When DSBs are repaired by HR, an undamaged complementary molecule which contains homologous DNA information, like a sister chromatid, is required as template. Therefore, HR can only be used in the S and G2 phases of the cell cycle (Zhao et al. 2020). When DSBs occur in eukaryotes, the stage of the cell cycle determines, among other factors, which repair mechanism will be chosen.

During the highly regulated process of HR, three main stages are distinguished. After the recognition of the DSB, the first step is 5'-3' resection. By nucleolytic degradation of the 5'-strands, which is catalyzed by endonucleases like the MRN complex (including Mre11, Rad50, and Nbs1) and CtIP (Krajewska et al. 2015), 3'-single-stranded DNA (ssDNA) ends are generated. In the second step, proteins including Exo1, DNA2 and Sgs1 are recruited to the ssDNA sites to

further reinforce the resection. Subsequently, replication protein A (RPA) filaments are gathering around the ssDNA-ends. RPA is the major protein that binds to ssDNA in eukaryotic cells. The function of RPA is to prevent ssDNA from binding to itself and forming DNA hairpins and to coordinate DNA end resection (Chen et al. 2013). This leaves the ssDNA site open for further proteins to coat and proceed HR. Finally, human BRCA1 and BRCA2 can promote Rad51 filament formation, replacing the existing RPA cover on the ssDNA sites. BRCA1 and BRCA2 are tumor suppressors (Liu J et al. 2010), which, in the process of HR, regulate and facilitate the homology search and DNA strand invasion to the sister chromatids (Krajewska et al. 2015).

An early cellular response to DSBs is the phosphorylation of the Ser-139 residue of the histone variant H2AX to form  $\gamma$ H2AX, which is now regarded as a marker indicating DNA double-strand breaks. Immunofluorescent staining of  $\gamma$ H2AX in Mbp-regions surrounding DSBs, so-called foci, and their quantification are considered as gold standard for the evaluation of the efficiency of radiation or of some drugs in inducing DSBs (Mah et al. 2010). In addition the proteins 53BP1, originally identified as a DNA damage checkpoint protein (Markova et al. 2007), and BRCA1, a well-known tumor suppressor, were found co-localized with  $\gamma$ H2AX foci at the radiation-induced DSB sites. BRCA1 and 53BP1 are at the center of the processes choosing between the two repair pathways, HR or NHEJ (Daley and Sung 2014). 53BP1 works as an antagonist of BRCA1 and was shown to restrict resection in G1 phase, thus inhibiting homologous recombination and promoting NHEJ (Bothmer et al. 2010). It promotes classical non-homologous end joining (c-NHEJ) by recruiting RIF1 to inhibit BRCA1 recruitment to break sites, thereby antagonizing BRCA1-CtIP-mediated end resection and blocking BRCA2/RAD51-mediated homologous recombination (Zhao et al. 2020). In a BRCA1 mutant mice model, 53BP1 promotes genomic instability and mammary tumorigenesis. Inactivation of 53BP1 partially restores homologous recombination in BRCA1 deficient cells (Bunting et al. 2010) (Cao et al. 2009). BRCA1 was shown to suppress cancer by promoting the HR repair process (Nakamura et al. 2010). The presence of BRCA1 leads to removal of 53BP1 in S phase and allows the resection (Bunting et al. 2010). Therefore, these two proteins are critical for choosing of DNA repair

pathways and important for maintenance of integrity of genomes, Figure 1.1.

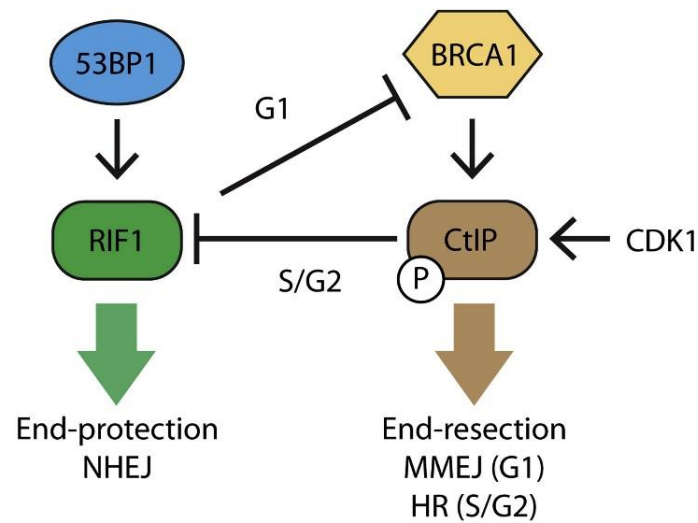


**Figure 1.1:** Model of the regulatory circuit controlling DSB repair pathway choice (Escribano-Díaz et al. 2013).

## Tumor micro-environment

Formation and development of cancer is considered to be a multi-step process. Tumoral microenvironment (TME) is composed of cellular and non-cellular components. In addition to the tumor cells, TME contains abundant stromal cells, immune infiltrate and the vascular network. These components work coordinately and form the microenvironment of solid tumors *in vivo*. Among the cellular components, cancer associated fibroblasts (CAFs), pericytes, immune, inflammatory cells and blood vessels are also considered to participate in proliferation and progression of cancer (Koontongkaew 2013). Specifically, TME components may play important roles during oncogenesis, migration, invasion, metastasis, metabolic interactions and response to therapies (Quail and Joyce 2013).

CAFs are the predominant cell type in the stroma and mainly responsible for the stroma production and maintenance (Buchsbaum and Oh 2016). The main

function of CAFs is secreting the extracellular molecules like key proteins (collagen, elastin), hyaluronic acid and vesicles which constitute the extracellular matrix (ECM) (Alkasalias et al. 2018). Also, CAFs produce various growth factors and cytokines which can regulate the function of immune cells in the tumor microenvironment and eventually result in tumor invasion or metastasis and introduce therapy resistance. Therefore, revealing the interaction of cancer cells and CAFs is critical for cancer therapy strategies.

The existence of CAFs promotes tumorigenesis. Human prostatic CAFs co-cultured together with initiated human prostate epithelial cells has been shown to promote growth and reconstruct the histology of epithelial populations *in vitro* and in a mouse model (Olumi et al. 1999). CAFs are also related to tumor angiogenesis. In the hypoxic microenvironment, to satisfy the needs of the high proliferative rate of tumor cells, tumors need to develop a vascular network. The tumor blood vessel growth is caused in part by abnormal levels of growth factors e.g. vascular endothelial growth factors (VEGF) or transforming growth factors (TGF- $\beta$ ) which are secreted by both tumor cells and cancer-associated fibroblasts (Viallard and Larrivée 2017).

In addition, Akira reported that stromal cell-derived factor-1 (SDF-1) secreted by CAFs enhances the growth (Orimo et al. 2005) and improves the remote transfer of carcinoma cells. Mammalian Diaphanous-related formin2 (mDia2), which can assemble a dynamic F-actin cyto-skeleton, is involved in tumor cell migration and invasion. CAF-derived secretion of CXCL12/ SDF-1, which down-regulates mDia2 protein levels, disturbs the F-actin cell skeleton and enhances the motility of MDA-MB-231 breast cancer cells (Dvorak et al. 2018). The facts that CAFs can promote metastasis and drive the invasion of carcinoma cells has been reported by many researches (Gaggioli et al. 2007) (Hooper et al. 2010) (Labernadie et al. 2017). The promoted effect is also reported in 3D cultured spheroid model on a microfluidic device (Liu T et al. 2010).

CAFs were also described to adjust the radio-sensitivity of tumor cells. By 2D and 3D coculture of mouse tumor cells and skin or embryonal fibroblast, it was

observed that the impact of fibroblasts on tumor cell proliferation and radiosensitivity depends on the specific combination, that is fibroblasts can either act in a pro-tumorigenic and pro-resistance manner, or an anti-tumorigenic manner (Steer et al. 2019). CAFs themselves have been shown to be comparably radioresistant, rather going into senescence than dying, and to alter their secretion profiles after irradiation, thus influencing tumor cell behavior (Ansems and Span 2020).

In conclusion, by establishing *in vitro* co-culture models of malignant cells plus fibroblasts, the pathways how fibroblasts affect cancer cells can be further elucidated, finally leading to novel conceptions for cancer remedy.

### **Three-dimensional (3D) culture of cells**

In the past few decades, two-dimensional (2D) monolayer cell culture on the flat bottom surface has been the most common cell culture technique in biology research. However, in recent years, researchers more and more prefer 3D cell culture models, such as spheroids, as a kind of novel cell culture method which can represent more realistically the microenvironment as is found in the body. 3D cell culture introduces more cell-cell connections and communication of cells to neighboring cells and/ or to ECM (Lin and Chang 2008) (Kunz-Schughart et al. 1998). Many researches revealed different properties between cells cultured in 2D and 3D regarding characteristics and functions like cell growth rate, cell cycle (Li et al. 2003), cell communication, differentiation (Xu et al. 2020), invasion, sensitivity to radiation or chemicals, metabolism (Chitcholtan et al. 2013) and gene expression (Bott et al. 2010). Not surprisingly, testing of anti-tumor compounds in 2D culture has not always been found to be predictive.

Spheroids of cancer cells can be divided into 3 parts, the necrotic zone, the quiescent viable cell zone and the proliferating zone. A schematic diagram of zones inside 3D spheroids is shown in Figure 1.2. Due to the accumulation of waste and carbon dioxide and lack of oxygen and nutrients in the spheroid

center, the cells localized closer to the core start to show growth inhibition and, eventually, necrosis, but the cells in the outer layer can still keep on proliferating. This heterogeneity makes 3D spherical models more similar to solid tumors in natural situations. Due to vascular insufficiency and low intratumor blood flow, low levels of oxygenation exist in malignant solid tumors (Mueller-Klieser 1984). Many researches point out that hypoxia within solid tumors could be a critical reason for radio-resistance and anti-cancer drugs resistance (Gaedtker et al. 2007), since molecular oxygen is a potent radiosensitizer involved in mediating DNA damage. Lack of  $O_2$  would reduce DNA damage induced by irradiation and lead to radio-resistance (Rockwell et al. 2009).

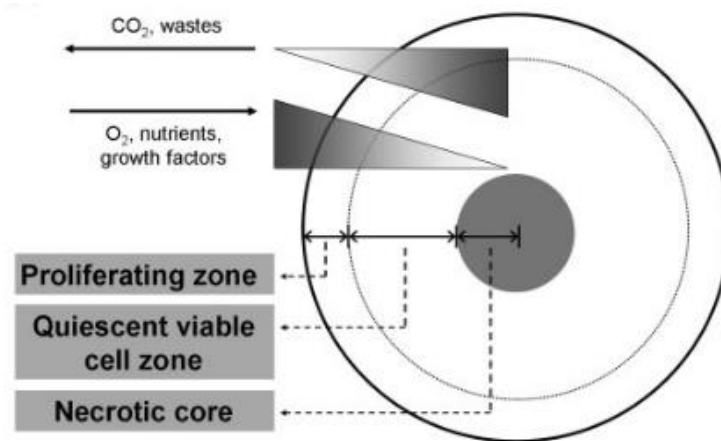


**Figure 1.2:** Scheme of heterogeneous insight of 3D cultured spheroid (Lin and Chang 2008).

Although the advantages of 3D models are clear, several factors so far have limited their application. 3D culture is more expensive and time-consuming, more difficult for live cell imaging, and there is a lack of established methods and protocols. Current approaches are divided into those using scaffolds and scaffold-free techniques. Multicellular spheroids are simple three-dimensional models that can be generated easily from a wide range of cell types due to the tendency of adherent cells to aggregate. Scaffold-free techniques include U-bottom non-adhesive plates, magnetic levitation (Souza et al. 2010), microfluidic devices (Zhang and Nagrath 2013), hanging drop methods

(Timmins et al. 2005) and rotating culture (Pampaloni et al. 2007).

Referring to scaffold-based methods, more than 100 types of matrices and scaffolds of both organic and inorganic nature are being currently used for obtaining such cultures. 3D scaffolds are generated using various natural (collagen, gelatin, elastin, fibrin, etc.) and synthetic polymers. These composites mimic the native extracellular matrix. The choice of matrix type is based on the cell type and on the nature of the study (Ravi et al. 2015). Type I collagen matrix is the most commonly used in matrix-based 3D culture system.

Another advantage of 3D culture is that it is more convenient for generating co-culture models than traditional flat 2D culture. The mixture of different kinds of cells simulates the natural tumor and its microenvironment, representing a closer model to the *in vivo* solid tumors. Although both monoculture and coculture spheroids are easy to generate, their complexity and response to chemotherapy, radiotherapy or other kinds of treatment is more representative and realistic than the 2D cultures.

Cadherins play an important role for spheroid formation. For example, in L929 cells, spheroid formation capability, size and speed depend on the expression of N-cadherin. Along with increasing the expression of N-cadherin, cells aggregate much faster and form larger clusters, whereas untransfected L929 cannot form spheroids when cultured in 3D. Furthermore, the localization of cells within the coculture spheroid appears to depend on the molecule expression. It was reported that 4 hours after coculturing, cells with different levels of N-cadherin still mixed randomly into a loose cluster; while after 24 hours in 3D coculture models, cells which express lower N-cadherin localize at the periphery of the 3D structure, and those with higher level of N-cadherin expression were compressed into a cohesive core in the middle. But when those two cell lines had similar expression level of cadherins, their intermixed cells failed to separate (Foty and Steinberg 2005). Other results pointed out that the expression of E-cadherin rather than N-cadherin is strongly correlated with the formation of compact aggregates in 3D culture. Inhibiting the activity of E-cadherin on HepG2 cells by EGTA or E-cadherin-blocking antibodies, the cell

compaction was delayed and corresponded to a loose aggregate morphology, failing to undergo further compaction into spheroids (Lin et al. 2006).

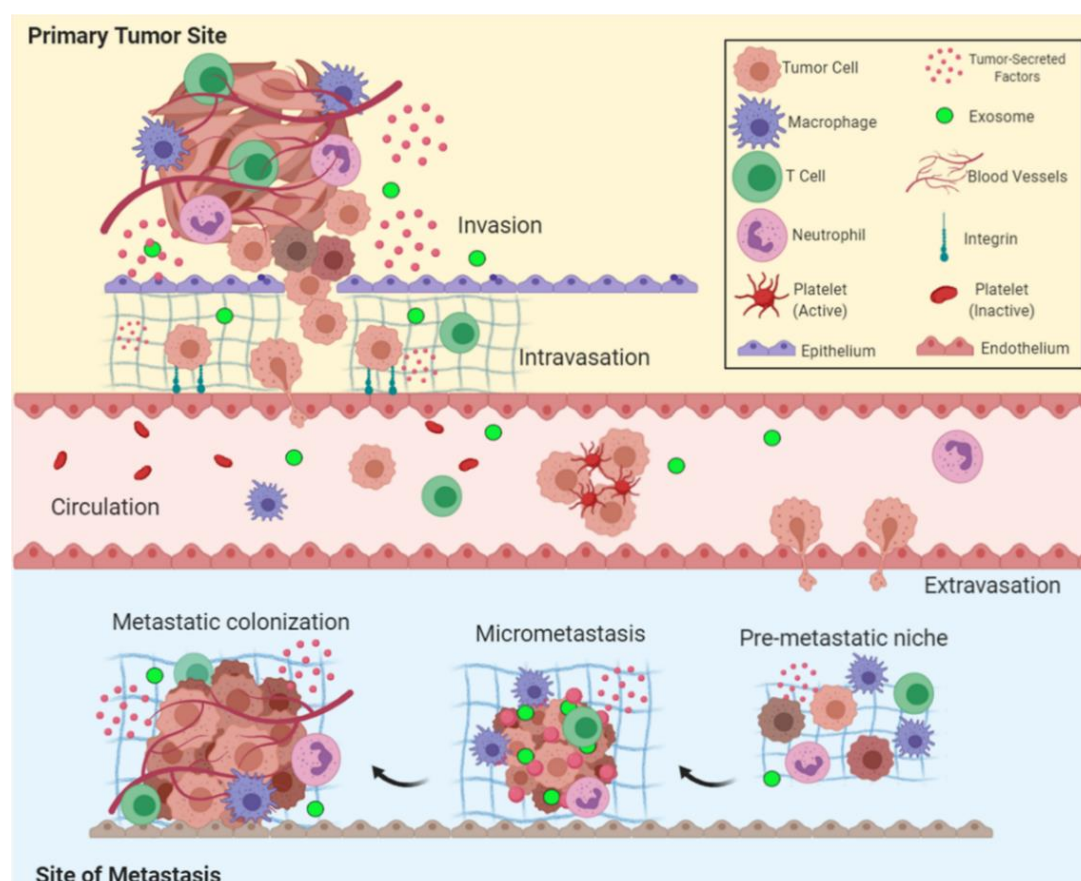
### **EMT transition**

The epithelial-mesenchymal transition (EMT) provides mechanisms for epithelial cells to overcome the physical constraints and adopt a motile phenotype. This EMT transition has been shown to play important roles in many biological processes, for example, in wound healing processes and organ fibrosis (Stone et al. 2016), and in the initiation of metastasis in cancer (Thiery 2002). It is believed that invasive epithelial cells always exhibit some mesenchymal characteristics. During the process of EMT transition, epithelial cells lose features like polarity and epithelial plasticity and reduce intercellular cell-cell adhesion. This is associated with down-regulation of epithelial markers such as E-cadherin and  $\alpha$ -catenin and upregulation of mesenchymal markers including fibronectin, N-cadherin and vimentin (Grünert et al. 2003). Often this process is accompanied by a more spindle-shaped morphology (Birchmeier and Behrens 1994).

E-cadherin is considered as a hallmark protein expressed in epithelial cells, playing an important role in the maintenance of intercellular junctions, and localizing strongly at the cell-cell boundaries. E-cadherin is an invasion suppressor and loss of expression of E-cadherins was early on believed as a marker of cancer metastasis and malignancy which promotes migration and invasion (Schipper et al. 1991).

### **Migration, invasion and metastasis**

Metastasis is a multi-step process where cancerous cells first invade into the basement membrane and surrounding tissue, intravasate into blood vessels, and finally localize, survive and grow at remote sites. Migration and invasion are the most important steps (Fig 1.3). To manage all these steps, coordination of cell movement and matrix remodeling are essential (Bravo-Cordero et al. 2012).

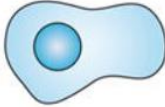


**Figure 1.3:** Current and emerging targets for the management of breast cancer bone metastasis (Rose and Siegel 2010).

### Migration

Cell migration is shown involved in many pathological processes, like immune response (Madri and Graesser 2000) and tumor progression (Wu et al. 2021). Cellular motility performed in 3D means that migrating cells are continuously embedded in a cellular or ECM context (Yamada and Sixt 2019). This is a highly integrated process that includes development of cytoplasmic protrusions, attachment and traction (Tahtamouni et al. 2019). The major categories of 3D cell migration are mesenchymal, amoeboid (Poincloux et al. 2011), or collective migration and streaming. Mesenchymal and amoeboid migration are the two best characterized modes for single cell migration. Mesenchymal cells display elongated morphology, while in amoeboid migration, cell constantly change

shape and form pseudopods by rapidly protruding and retracting extensions. For multi-cellular migration, collective migration and streaming are observed. In most types of collective migration, the leading cells of moving cell protrusions modify or degrade the stroma tissue along the migration path, allowing follower cells to move in tracks thus generated (Fig 1.4) (Roussos et al. 2011).

	Single cell migration		Multicellular migration	
	Amoeboid	Mesenchymal	Collective or chain migration	Streaming
Movement type				
Cell types	<ul style="list-style-type: none"> <li>• Dictyostelium discoideum</li> <li>• Leukocytes</li> <li>• Tumour cells</li> </ul>	<ul style="list-style-type: none"> <li>• Fibroblasts</li> <li>• Neural crest endothelium</li> <li>• Tumour cells</li> </ul>	<ul style="list-style-type: none"> <li>• Border cells in <i>Drosophila melanogaster</i></li> <li>• Epithelial-like cells in zebrafish and <i>D. discoideum</i></li> <li>• Mammalian cells involved in gastrulation, wound healing and cancer</li> </ul>	<ul style="list-style-type: none"> <li>• <i>D. discoideum</i></li> <li>• Tumour cells</li> <li>• Developing neural crest cells</li> </ul>

**Fig 1.4:** Types of cell migration and typical cell types (Roussos et al. 2011).

## Invasion

About 81 % of breast cancers are invasive or infiltrating, which means that these mammary carcinoma cells have penetrated into neighboring adjacent tissues. Local invasion of tumor cells is the first step of metastasis. Usually, cancer cells utilize different ways of invasion behavior under different environmental conditions. Pathology studies show that there are mainly three modes of invasion: 1) Migrating as single cells, in which cells lack cell-cell interaction. Single cell migration is the best studied mechanism of cell movement contributing to cancer metastasis, 2) as multicellular loosely-attached cell streaming, in which several cells migrate along the same path and 3) as migration in a well-organized, adherent collective manner, where cells

move as strands lead by leader cells (Clark and Vignjevic 2015).

In the recent years, the role of fibroblasts for invasion capability of cancer cells has increasingly been acknowledged. They can influence the cancer cell phenotype by paracrine communication, which e.g., can induce mesenchymal traits in the cancer cells. Especially, CAFs in the stroma produce many kinds of growth factors and cytokines which can regulate the many behaviors of carcinoma cells including proliferation and metastasis (Quail and Joyce 2013). In addition, invasion-promoting activity of fibroblasts can be linked to their ECM remodeling ability (Koontongkaew 2013). Stromal fibroblasts as a key type of extracellular cell components are reported to be involved in a collective invasion mechanism (Cao et al. 2016), which enables cancer cells with epithelial traits, which cannot invade themselves, to follow leading fibroblasts along fibroblast-produced tracks in the matrix (Gaggioli et al. 2007).

Molecular factors that have been found to modulate the migration mode and invasion during cancer progression include metalloproteases (MMPs) mediating collagenolysis in ECM remodeling (Wolf et al. 2007), the Rho-pathway linking individual migration, proliferation and invasion (Johan and Samuel 2019), and cadherins or integrins regulating collective invasion models (Wu et al. 2021), (Poincloux et al. 2011). In fibroblast-led collective invasion of squamous cell carcinoma cells, inhibition of Rho/ROCK or MMPs signaling pathway in the fibroblasts blocked the collective invasion of the cancer cells, showing that the fibroblasts need Rho/ROCK signaling to generate tracks in the matrix in which the cancer cells can follow (Gaggioli et al. 2007), (Gaggioli 2008).

### ***Traditional Assay for migration and invasion***

So far, metastasis steps can only partially be modelled *in vitro*, e.g., by migration or invasion assays (Justus et al. 2014). The migration behavior in 2D is measured by transwell migration assays (Boyden chamber assays) or wound healing assays. In contrast to migration assays, invasion assays require that

the tumor cells pass a layer resembling the basement membrane or the extracellular matrix. Nevertheless, in the recent years, the more *in vivo*-like three-dimensional 3D multicellular tumor spheroids have increasingly been applied to investigate cell motility. If spheroids are embedded in matrix, invasion of individual cells into the surrounding matrix can be observed microscopically.

### **Metabolism and Mitochondria**

In general, radiobiology focuses on the radiation-induced damage to nuclear DNA. But, nowadays, more and more observations pointed out that ionizing radiation also has effects on the mitochondrial DNA and its functions (Kam and Banati 2013).

### ***Structure of Mitochondria***

Mitochondria are membrane-bound cell organelles surrounded by a double membrane which contain their own genome. The double membrane divides the mitochondria into four structural compartments: matrix, inner-membrane, intermembrane space and outer membrane (Huang 2004).

The outer membrane is permeable for ions and small uncharged molecules. Some proteins such as pore-forming membrane proteins (porins) are embedded on the outer membrane, which allow the small molecules to traverse freely. Large proteins have to be transported through the outer membrane by special translocases (TOM complex) (Neupert and Herrmann 2007).

The inner membrane is not as smooth as outer membrane, it has many folds which form the inner boundary membrane and cristae. The inner membrane is impermeable to most ions and molecules. Specific proteins can be imported by another group of translocases (TIM complexes) (Yu et al. 2017). The intermembrane space plays a pivotal role in the coordination of mitochondrial activities with other cellular processes, including exchange of proteins, lipids or metal ions between the matrix and the cytosol, the regulated initiation of

apoptotic cascades, signaling pathways that regulate respiration and metabolic functions, the prevention of reactive oxygen species produced by the respiratory chain, or the control of mitochondrial morphogenesis (Herrmann and Riemer 2010). The inner compartment which is surrounded by the inner membrane, is the mitochondrial matrix. The pH value of the matrix is around 7.9 to 8.0. The high pH of the mitochondrial matrix creates the transmembrane electrochemical gradient that drives ATP synthesis. Within the matrix, the replication transcription, protein biosynthesis and numerous enzymatic reactions take place (Alberts et al. 2002).

### ***Function of Mitochondria***

Within most of the eukaryotes, the main function of mitochondria is to be the place where the adenosine triphosphate (ATP) is produced through respiration to be used as the energy currency for cells. The cellular respiration converts the large molecules (glucose, amino acids and fatty acids) into smaller ones through catabolic reactions to produce energy and then release waste.

There are mainly three steps for cellular respiration in normal cells. First is the glycolysis which takes place in the cytosol and splits glucose into two molecules of pyruvate. Under aerobic conditions in normal cells, the pyruvates are fed into the citric acid cycle, also called Krebs cycle, which generates reduced electron carrier molecules. The final step is oxidation of these reduced molecules to generate ATP. This oxidative phosphorylation (OXPHOS) step relies on the electron transport chain (ETC) which transfers electrons from a series of proteins and organic molecules found on the inner membrane of mitochondria which finally reduce oxygen into H<sub>2</sub>O (Bratic and Trifunovic 2010). The electron transport chain is composed of complexes I-V, which represent NADH dehydrogenase, succinate dehydrogenase, cytochrome c reductase, cytochrome c oxidase and ATP synthase, respectively (Kühlbrandt 2015).

During the electron exchange processes, there are two kinds of electron carriers involved, reduced nicotinamide adenine dinucleotide (NADH) and flavin

adenine dinucleotide ( $\text{FADH}_2$ ). Reduced NADH carries energy to complex I of ETC and FAD is a bound part of complex II. At the inner mitochondrial membrane, electrons from NADH and  $\text{FADH}_2$  pass through the electron transport chain to oxygen, which is finally reduced to water. ATP synthase uses the thus generated proton gradient to produce ATP. Oxidative phosphorylation generates 36 to 38 molecules of ATP per glucose molecule during cellular respiration (Figure 1.5).

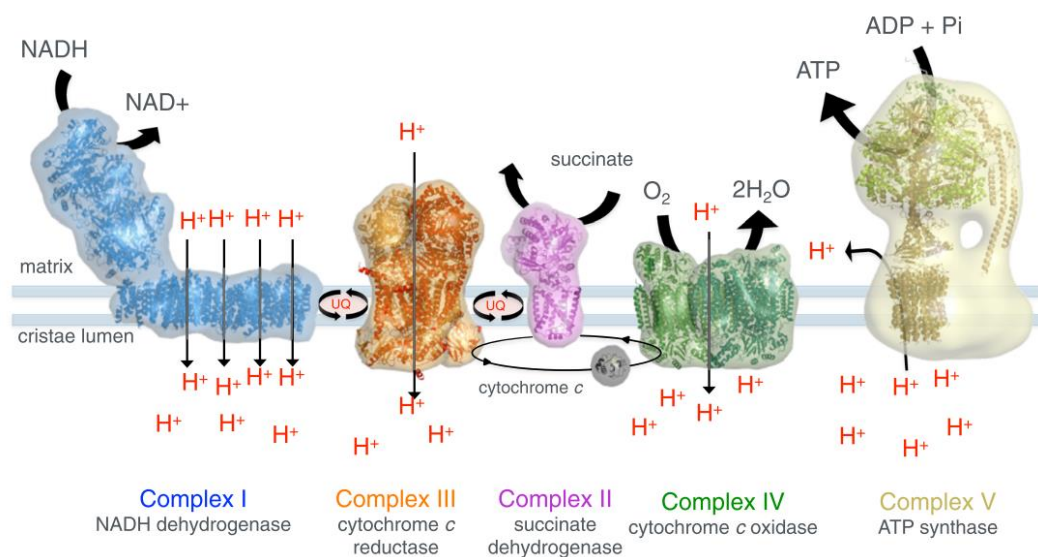


**Figure 1.5:** Scheme of membrane protein complex of electron transport chain embedded in the inner mitochondrial membrane (Kühlbrandt 2015).

In various cancers, OXPHOS is reduced and aerobic glycolysis dominates as the main method for ATP production. During glycolysis one molecule of glucose only produces two molecules of ATP. A shift to aerobic glycolysis was first proposed by Warburg (Warburg 1924). Some following researches indicated that cancer cells prefer glycolytic energy production even in the presence of sufficient oxygen within cancer cells (Smolková et al. 2011). This low-efficient of ATP production leads to huge demand of glucose in tumorous cells.

In addition to energy production, mitochondria participate in many biological processes, including cell cycle progression, differentiation, immune responses,

lipid and calcium homeostasis and apoptosis. These diverse roles of mitochondria are intimately connected to the structure and cellular context of the essential organelle. The shape and cellular distribution of the mitochondrial network is maintained in large part by the conserved activities of mitochondrial division, fusion, motility and tethering (Lackner 2014). Mitochondria are highly dynamic. The rapid morphology changes of mitochondria are correlated with the metabolic changing of cells. By fusion of mitochondria, tubular-like networks are formed, which by fission separate into individual smaller mitochondria again. Fission and fusion are carried out by a large number of dynamin-related GTPases (Kühlbrandt 2015). Fission and fusion are the regulators of mitochondrial connectivity. The lengths of mitochondria are determined by the balance between fusion and fission. When the mitochondria are damaged by some negative effects, to buffer the defects, mitochondria fuse together to facilitate communication and sharing of contents; the fission process enables the functionally defected parts of mitochondria to be eliminated (Lackner 2014). Furthermore, high OXPHOS activity correlates with mitochondrial elongation, suggesting that mitochondrial networks are more efficient at energy generation (Mishra and Chan 2016). Therefore, the dynamic of morphology changes of mitochondria can serve as another indicator to reflect the state of metabolism in the sub-cellular level.

### **Fluorescence microscopy and two-photon excitation fluorescence (TPEF)**

Our knowledge about the localization of specific molecules within cells and tissues has mainly been shaped by the use of fluorescence microscopy, where the molecules in question are labeled with a fluorescent chromophore, mostly by using immunolabeling or by expression of fluorescent proteins. Fluorescence occurs when a fluorescing molecule absorbs the light energy from one photon, which results in excitation, followed by the emission of some of this light energy shortly after. Because some energy is lost in this process, the emitted photon has less energy and longer wavelength than the absorbed photon. This change is called the Stokes shift. Because of the Stokes shift, excitation of most currently used fluorophores requires rather short

wavelengths, resulting in limited penetration depths. Therefore, for the analysis of thicker 3D samples, multiphoton microscopy is of advantage, where the fluorophore simultaneously absorbs the energy from multiple photons, but only emits one photon. In the case of two-photon excited microscopy (TPEF) two photons are required with each about half of the energy required in one-photon excitation (Benninger and Piston 2013). The energy of each of the two absorbed photons is then lower than the energy of the emitted photon, allowing for long excitation wavelengths in the red or far-red region of the spectrum. Simultaneous absorption requires a very high spatial and temporal density of photons, which can be achieved by high-powered, pulsed lasers.

Using infrared light excitation can reduce the scattering in the tissue. Due to the multiphoton absorption, the background signal is strongly suppressed. Both effects lead to an increased penetration depth for this technique (Svoboda and Yasuda 2006). The detection depth of TPEF can reach to several millimeters (Rubart 2004). In addition, by using lower energy photons, TPEF causes less photobleaching.

Cells and tissues contain a variety of auto-fluorescent molecules which allow a label-free imaging. Among the most important is NADH, which exhibits autofluorescence in its reduced form, whereas the oxidized form is not fluorescent. Methods based on NADH autofluorescence have been widely used to monitor cellular redox state and indirectly also energy metabolism (review by Schaefer et al. 2019). NADH also has a good two-photon cross section, allowing analysis via TPEF. Since NADPH autofluorescence cannot be differentiated from NADH autofluorescence, however, one talks about NAD(P)H measurement. In the case of FAD, the oxidized form exhibits autofluorescence while the reduced form does not. Based on autofluorescence of NAD(P)H and FAD, TPEF microscopy allows determining an optical redox ratio (ORR), defined as the TPEF intensity of FAD/ [NAD(P)H+FAD] (Varone et al. 2014). A disadvantage of fluorescence intensity-based evaluations is, however, that these are prone to experimental artifacts. Fluorescence lifetime imaging microscopy enables metabolic imaging that is not affected by intensity issues.

## Fluorescence life-time imaging microscopy (FLIM)

Fluorescence lifetime ( $\tau$ ) of a fluorophore is defined as the time that the molecule remains in the activated state after excitation before decaying to the ground state. Fluorescence lifetime of a fluorophore depends on its local micro-environment and is independent of the intensity. Decay times can be measured by time-correlated single photon counting (TCSPC) units. For FLIM imaging, images are firstly mapped from the total photons that are counted in each pixel, to obtain an intensity image. For each pixel then an intensity decay curve is determined (Figure 1.6), which can be fitted to one-component or multi-component exponential decay curves. For visualization, the mean lifetime ( $\tau_m$ ) for each pixel is calculated and color-mapped. Since the fluorescence lifetime does not depend on concentration, absorption by the fluorophores, sample thickness and photo-bleaching, this method is more robust than intensity-based methods (Becker 2010).

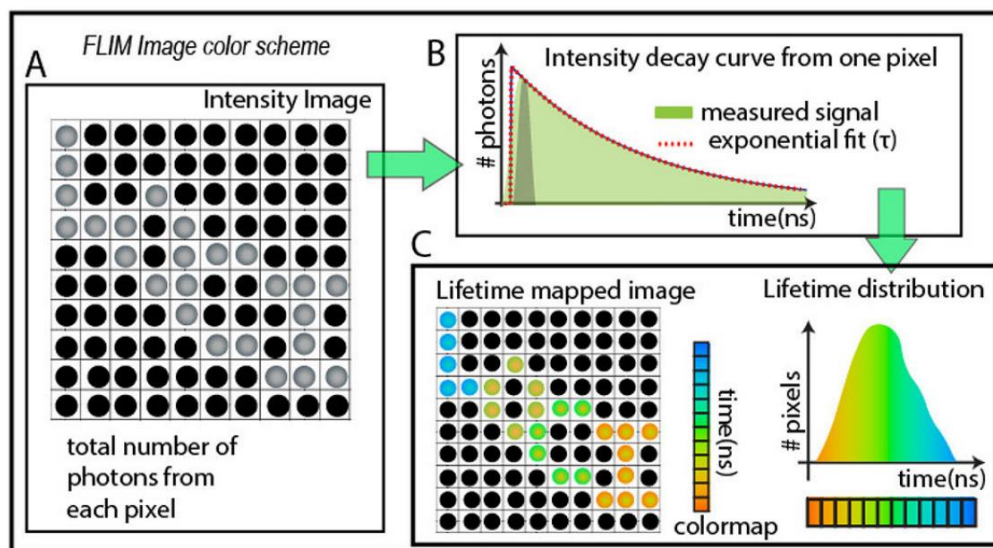


**Figure 1.6:** (A) mapping of intensity FLIM images. (B) Intensity decay curve fitted to an exponential function to determine the lifetime of each pixel. (C) color-mapped FLIM images according to the varieties of mean lifetime of the molecule detected (Chacko and Eliceiri 2019).

FLIM has also been verified as a robust and powerful method to monitor the

dynamic changes of the endogenous metabolic cofactors, NAD(P)H and FAD in cells or in tissues. For these molecules lifetime depends on whether they are in a free state or protein-bound. For NAD(P)H, the free component has a short lifetime of about 0.3 to 0.4 ns, whereas the protein-bound NAD(P)H decays slower than the free NAD(P)H. Depending on different types of proteins, the lifetime of protein-bound NAD(P)H varies from 2.0 ns to 2.3 ns. In the case of FAD, protein-bound FAD decays faster than free FAD, with a few 100 ps of lifetime for protein-bound and a few ns for free FAD (table 1.1).

Endogenous fluorophore	Excitation (nm)	Emission (nm)	Lifetime (ns)
NAD(P)H	300-380	450-500	0.3 (free), 2.0-2.3 (bound)
FAD	420-500	520-570	2.3 to 2.9 (free), <0.01 ns (bound)

**Table 1.1:** Spectral characteristics and lifetimes of endogenous fluorophores (Berezin and Achilefu 2010).

In FLIM data analysis, the fast and slow components can be separated by double-exponential decay analysis. The mean lifetime ( $\tau_m$ ) of 2 components is calculated as  $\tau_m = \tau_1 \cdot a_1 + \tau_2 \cdot a_2$ . The ratio of the amplitudes of two components,  $a_1/a_2$ , directly represents to the ratio of unbound/bound NAD(P)H or bound/unbound FAD. Since the pool of protein-bound NADH in cells is quite stable, a shift in  $\tau_m$  is thought to reflect the ratio of NADH to  $\text{NAD}^+$ , as depicted in Figure 1.7 (Schaefer et al. 2019). That is, shortening of  $\tau_m$  is associated with a shift towards glycolytic energy generation, while lengthening is associated with oxidative phosphorylation.

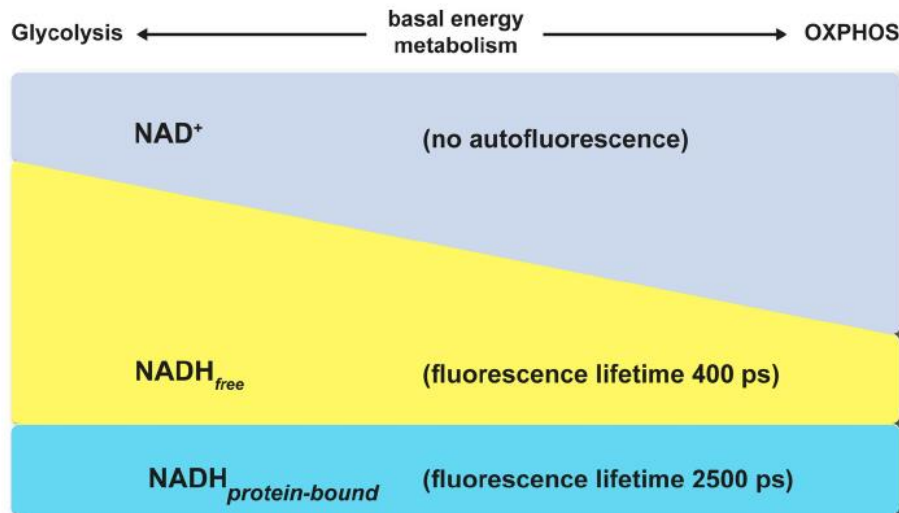


**Figure 1.7:** Determination from metabolic state from NADH lifetimes (Schaefer et al. 2019).

Skala et. al revealed that multiphoton FLIM can be used for precancer diagnosis through the lifetime shifts of NADH. Low-grade and high-grade pre-cancers exhibit decreased NADH lifetimes compared to normal tissues. Inhibition of glycolysis increased NADH lifetime and inhibition of oxidative phosphorylation decreased the lifetime. Therefore, they concluded that lifetime shortening, associated with an increase in free NADH, is correlated with a metabolic shift from oxidative phosphorylation towards glycolysis (Skala et al. 2007). FAD fluorescence lifetime alterations are less well characterized than NAD(P)H fluorescence lifetime alterations. Free FAD, which has longer lifetimes than protein-bound FAD, has been associated by some authors with oxidative phosphorylation, but its association with glycolytic metabolism has also been proposed (Kalinina et al. 2021).

Data recorded by the TCSPC system can also be analyzed by a phasor plot analysis. The phasor plot provides a visualized view of the FLIM data that does not require fitting. Each pixel in the images will be reflected as a point in the phasor plot, Figure 1.8. The lifetime of a species with mono-exponential decay curve lies on the universal semi-circle line in the phasor plot; Species with two

exponential decay curves yield lifetime signals inside the circle and on the linear combination of their single exponential lifetime components. The ratio of two component for a double-exponential lifetime determines the position of mean lifetime between 2 single exponential components.

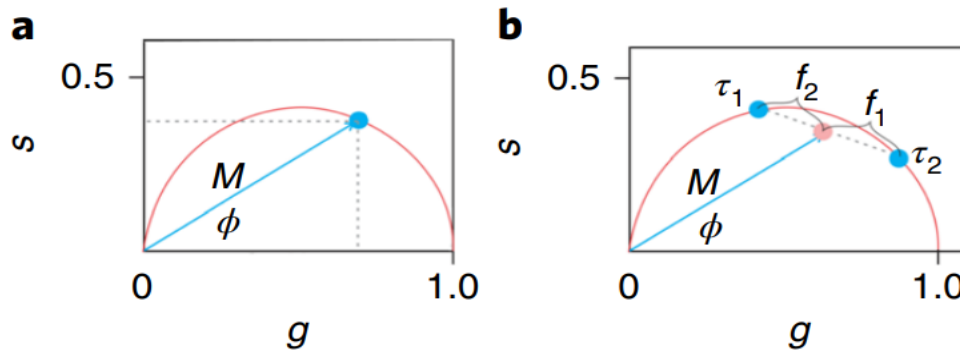


**Figure 1.8:** Theoretical positions of fluorescence lifetimes in phasor plot. A. distribution of mono-component is on the circle B. Two single exponential lifetimes determined by the ratio of the linear combination for a multi-exponential lifetime (Ranjit et al. 2018).

### Tasks of my research

While radiotherapy aims to destroy tumor cells by inducing DNA damage, it may also induce signal pathways that promote a more aggressive phenotype, including invasiveness. Therefore, a better understanding of the effects radiation has on invasion mechanisms is important. There are a variety of different invasion mechanisms, but so far, the methods used to study radiation effects on invasion, such as the Boyden chamber approach, did not try to differentiate between different invasion mechanisms.

The aim of this thesis was to develop a 3D model system for fibroblast-led invasion of breast cancer cells with epithelial phenotype. Four different breast cancer cell lines, namely BT474, MCF-7 and SkBr3 characterized as luminal cell lines with more epithelial-like phenotype, and MDA-MB-231 characterized as basal-like breast cancer cell lines with mesenchymal phenotype, should be

characterized with regard to their ability to generate 3D spheroids and their ability to invade into invasion matrix. Then the effect of coculture with fibroblasts should be investigated with regard to fibroblast recruitment, spheroid formation, radiation sensitivity, and, importantly, invasive behavior. Skin fibroblasts should be used rather than cancer-associated fibroblasts to minimize endocrine interactions between fibroblasts and cancer cells. After establishing a model for fibroblast-led cancer cell invasion, the effect of radiation on this process should be evaluated. In addition, label-free imaging methods to study radiation effects on metabolism in cellular level, as well as invasive processes, should be established in collaboration with the group of Prof. Popp, Jena. While the pandemic situation strongly inhibited this part of the work, at least some proof-of-principle or preliminary data could be generated and benchmarked.

A deeper understanding of the radiation influence on the 3D spherical models bridges the gap of traditional 2D cell culture to *in vivo* investigations and provides valuable information for further research to improve the therapeutic strategy for patients in the clinic.

## 2. Material

### 2.1 Cell lines

#### Mammary carcinoma cell lines

Cell line	Origin	Tissue	Culture Medium	Culture Condition
MCF-7 (HMGU)	DMSZ, via Horst Zitzelsberger HU	Human, breast cancer	RPMI-1640+ 10 % FBS + 1 % Pen/Strep	5 % CO <sub>2</sub> , 37 °C and air humidity 95 %
BT474	CLS, via Kirsten Lauber, University Hospital of LMU Munich	Human, breast cancer	RPMI-1640+ 10 % FBS + 1 % Pen/Strep	5 % CO <sub>2</sub> , 37 °C and air humidity 95 %
SkBr3	CLS, via Kirsten Lauber, University Hospital of LMU Munich	Human, breast cancer	DMEM+ 10 % FBS + 1 % Pen/Strep + 1 % L-Glutamine	10 % CO <sub>2</sub> , 37 °C and air humidity 95 %
MDA-MB-231	Sigma-Aldrich, ECACC	Human, breast cancer	DMEM + 10 % FBS + 1 % Pen/Strep + 1 % L-Glutamine	10 % CO <sub>2</sub> , 37 °C and air humidity 95 %
MCF-7 (HMGU) pMcc-tagRFP-PN-6#	Strain collection AG Friedl	Human, breast cancer	RPMI-1640+ 10 % FBS + 1 % Pen/Strep + 0.3 µg puromycin/ mL	5 % CO <sub>2</sub> , 37 °C and air humidity 95 %
MCF-7 (HMGU) pMcc-GFP-PN 1#	Strain collection AG Friedl	Human, breast cancer	RPMI-1640 + 10 % FBS + 1 % Pen/Strep + 0.3 µg puromycin/ mL	5 % CO <sub>2</sub> , 37 °C and air humidity 95 %
MCF-7	This work	Human,	RPMI-1640 + 10 %	5 % CO <sub>2</sub> ,

(HMGU) pMcc- GFP- 53BP1- PN-L#		breast cancer	FBS + 1 % Pen/Strep + 0.3 µg puromycin/ mL	37 °C and air humidity 95 %
--------------------------------------------	--	------------------	--------------------------------------------------	-----------------------------------

### Fibroblasts

Cell line	Origin	Tissue	Culture Medium	Culture Condition
BJ1- hTert	BD Clonotech	Human, skin, immortalized fibroblasts	DMEM + 10 % FBS+ 1 % Pen/Strep+ 1 % L- Glutamine	10 % CO <sub>2</sub> , 37 °C and air humidity 95 %
HDF	Sigma- Aldrich, ECACC; Lot # 1993 and Lot # 1515	Human, skin, primary human dermal fibroblasts	Fibroblast Basal Medium (cell) + 10 % FBS	5 % CO <sub>2</sub> , 37 °C and air humidity 95 %
PDF	ATCC Lot # 70015187	Human skin, human primary fibroblasts	Fibroblast Basal Medium (ATCC) (supplemented with Fibroblast Growth Kit-Low serum)	5 % CO <sub>2</sub> , 37 °C and air humidity 95 %
FH20-2	Strain collection, AG Friedl	Human fibroblasts	DMEM + 10 % FBS + 1 % Pen/Strep + 1 % L-Glutamine	10 % CO <sub>2</sub> , 37 °C and air humidity 95 %
GM637	Strain collection, AG Friedl	Human fibroblasts	DMEM + 10 % FBS + 1 % Pen/Strep + 1 % L-Glutamine	10 % CO <sub>2</sub> , 37 °C and air humidity 95 %

### 2.2 Plasmids

Plasmid	Resource
pMcc-tagRFP-PN	AG Friedl
pMcc-GFP-53BP1-PN	AG Friedl

## 2.3 Cell culture materials

### Cell culture medium:

Reagent	Company	Product number
Dulbecco's Modified Eagle's Medium (DMEM)	Sigma-Aldrich	D6429
Roswell Park Memorial Institute Medium (RPMI)-1640 (1x)	Sigma-Aldrich	R8758
Fetal Bovine Serum (FBS)	Sigma-Aldrich	F7524 Lot# BCBQ7892V
L-Glutamine solution	Sigma-Aldrich	G7513
Penicillin-Streptomycin	Sigma-Aldrich	P0781
Dulbecco's Phosphate Buffered Saline (PBS) in 10 L dH <sub>2</sub> O dissolved & autoclaved	Sigma-Aldrich	D5652
TripLE™ Express Enzyme (1X), no phenol red	Thermo Fisher Scientific	12604-013
Trypsin/EDTA solution	Sigma-Aldrich	T3924
Fibroblast Basal Medium	ATCC	PCS-201-030
Fibroblast Basal Medium	Cell Applications	115-500
Fibroblast Growth Kit- Low serum	ATCC	PCS-201-041

### Transfection reagents:

Reagent	Company	Product number
Opti-MEM I Reduced-Serum Medium	GIBCO	31985-070
Lipofectamine 2000	Invitrogen by Thermo Fisher Scientific	11668-027

**Cell culture platforms:**

Plate	Supplier	Product number
Cellstar Cell Culture Dish, PS, 100 mm * 20 mm	Greiner Bio-One	664160
T25 Cell Culture Flask, PS	Greiner Bio-One	690175
Nunclon™ Sphera™ Microplates, 96 U Bottom	Thermo Fisher Scientific	174925
Corning 96 well Spheroid Multiplates	Corning	4515
6-well cell culture plate	Falcon	353046
VitroGel 3D High Concentration	TheWell Bioscience	TWG001
3D CoSeedis™ System	abc biopply	P/N 22-UB-V0817

**2.4 X-ray irradiation**

For X-ray irradiation with 6 MV photons an Elekta Synergy linear accelerator was used. Multi-well plates were covered with a 2 cm water-equivalent layer. Plates were positioned in the center of the beam with a source-surface distance of 100 cm. Dose was applied in single fractions with a dose rate of 6 Gy/ min. The beam was operated by Mr. Winklhofer at Department of Radiation Oncology, University Hospital of LMU Munich.

**2.5 Western Blot****Cell lysis buffer**

Chemicals/ Equipment	Components
RIPA buffer	40 mL Tris-HCl Solution (0.3 g Tris, 1 M HCl, pH=8.0) + 0.45 g NaCl + 1 g SDS + 0.25 g Sodium Deoxycholate + 500 µL NP-40 + ddH <sub>2</sub> O up to 50 mL
7x Protease inhibitor	1.5 mL PBS buffer + 1 tablet of complete Mini protease inhibitor cocktail (Roche)

10x Phosphatase inhibitor	1 mL PBS + 1 tablet of PhosSTOP EASYpack phosphatase inhibitor cocktail (Roche)
Centrifuge	Hettich Centrifuge, Universal 320R

### SDS-PAGE Gel electrophoresis and membrane transfer

Chemicals/ Equipment	Components/ Catalog
10x Tris/Glycine/SDS running buffer	BIO-RAD, Cat # 161-0723
4x Laemmli buffer (50 mL)	13.4 mL Tris (1 M, pH 8.6) + 8 % SDS (4 g) + 20 % Glycerin (10 mL) + 0.4 % bromophenol blue (0.2 g) + 10 % 2-mercaptoethanol (10 mL) + ddH <sub>2</sub> O to 50 mL
1x Transfer buffer (2 L)	100 mL 20x NuPAGE transfer buffer (Thermo Fisher Scientific) + 200 mL methanol (Sigma-Aldrich) + 1700 mL ddH <sub>2</sub> O
Ponceau Red solution (100 mL)	5 % trichloroacetic acid (5 g) + 2 % Ponceau red (0.2 g) + ddH <sub>2</sub> O to 100 mL
4-20 %, Mini-PROTEAN TGX Stain-Free™ Protein Gel	BIO-RAD, Cat # 4568093
Amersham™ Protran™ 0.2 µm NC Nitrocellulose Blotting Membrane	GE Healthcare Life Science, 10600001
Precision Plus Protein™ Dual Color Standards	BIO-RAD, Cat# 161-0374
Mini-PROTEAN Tetra Vertical Electrophoresis Cell	BIO-RAD, Cat# 1658004

### Blotting and chemo-luminescence solutions

Solution	Brand	Product number	Components
PBST washing buffer	Sigma-Aldrich	D5652	1000 mL PBS + 0.1 % Tween 20

5 % (v/v) Milk	Carl Roth	T145.2	5 % milk powder in PBST washing buffer
10x Roti-Block	Carl Roth	A151.2	1:10 dilution in dH <sub>2</sub> O
Lumigen ECL Ultra solution	Lumigen	TMA-100	1 mL solution A + 1 mL solution B

### Primary and secondary antibodies

Name	Company	Product number
Anti E-Cadherin (24E10) Rabbit mAb	Cell Signaling	3195
Anti N-Cadherin (D4R1H) XP Rabbit mAb	Cell Signaling	13116
Anti Cytokeratin 18 (RGE53) Mouse mAb	Thermo Fisher Scientific	MA1-06326
Anti $\alpha$ -Smooth Muscle Actin (1A4) Mouse mAb	Cell Signaling	48938
Anti EpCAM (VU1D) Mouse mAb	Cell Signaling	2929
Anti Fibronectin Rabbit polyclonal	Sigma-Aldrich	F3648
Anti Vimentin (D21H3) XP Rabbit mAb	Cell Signaling	5741
Anti Histone H2B Rabbit polyclonal	Abcam	Ab1790
Goat anti-Mouse IgG-HRP	Santa Cruz Biotechnology	sc-2005
Goat anti-Rabbit IgG-HRP	Santa Cruz Biotechnology	sc-2004

### 2.6 Immunofluorescence staining

Product	Company	Product number
Bovine Serum Albumin (BSA)	Sigma-Aldrich	A2153
4'6-Diamidino-2-Phenyl (DAPI)	Sigma-Aldrich	D9564
ProLong™ Gold antifade reagent	Invitrogen	P36934
Glycine	Sigma-Aldrich	G8898
Paraformaldehyde (PFA)	Sigma-Aldrich	P6148

### Primary and Secondary Antibody

Name	Company	Product number
Anti Vimentin (D21H3) XP Rabbit mAb	Cell Signaling	5741
Goat anti-rabbit IgG, Alexa Fluor 488	Molecular Probes	A-11034

Product	Company	Product number
Tissue Tek O.C.T Compound	Sakura	4583
Tissue Tek Cryomold Biopsy Molds (10 x 10 x 5 mm)	Sakura	4565
VWR Microscope Slides with cut edges and frosted end	VWR	631-1551
Menzel-Gläser SUPERFROST Plus	Menzel via Thermo Fisher Scientific	10149870

### 2.7 HE staining assay

#### Chemicals for HE-staining

Chemical	Brand	Product number
Acetone	AppliChem	131007.1211
Eosin Y solution 0.5 % in water	Carl Roth	X883.1
Ethanol absolute	VWR	20821.310
Eukitt Quick-hardening mounting medium	Sigma-Aldrich	03989
Hemalum solution acid acc. to Mayer	Carl Roth	T865.1
Xylol	Honeywell	10315083

### 2.8 Invasion Assay

To study invasiveness, spheroids were embedded in Cultrex® Spheroid Invasion Matrix, a commercially available extracellular matrix blend of basement membrane extract from murine EHS sarcoma cells and collagen I

from bovine extensor tendons.

Product	Company	Product number
Cultrex® Spheroid Invasion Matrix	Trevigen	TRE-3500-096-03
ROCK-inhibitor Y-27632	Selleck Chemicals	S1049
Vybrant™ CFDA SE Cell Tracer Kit	Invitrogen	V12883
CellTracker™ Orange CMTMR Dye	Invitrogen	C2927

## 2.9 Mitochondria staining Assay

MitoTracker Red is a red fluorescent dye that passively diffuses across the plasma membrane and accumulates in active mitochondria. Alexa Fluor 488 phalloidin is a marker with high affinity for F-actin, which is used to allow identification of cell borders.

Product	Company	Product number
Alexa Fluor™ 488 phalloidin	Thermo Fisher Scientific	A12379
MitoTracker™ Red CMXRos	Invitrogen	M7512

## 2.10 Investigation of metabolism dynamic by FLIM microscopy

Product	Company	Product number
25 Micro-Insert 4 well FulTrac for self-insertion	ibidi	80489
Glass Bottom Dish 35 mm	ibidi	81218

## 2.11 NSC treatment assay

Neocarzinostatin is a radiomimetic drug which can lead to DNA double-strand breaks.

Product	Company	Product number
Neocarzinostatin (NCS) 0.5 mg/ mL	Sigma-Aldrich	N9162-100UG

## 2.12 Microscopy

### A. Fluorescent Microscopes:

#### 1) Zeiss Axio-Observer Z1 Inverted Phase Contrast Epifluorescence Microscope

- Model: Axio-Observer Z1 (Carl Zeiss Microscopy GmbH)
- Brightfield Illumination Type: Halogen
- Phase contrast: NA: 0.55 WD: 26 mm Phase Contrast Wheel
- Fluorescence Light source: HXP 120 (Carl Zeiss Microscopy GmbH)
- Camera: AxioCam MRm (Carl Zeiss Microscopy GmbH)
- Objectives: 2.5x, 5x, 10x, 40x, 63x objective (Carl Zeiss Microscopy GmbH)
- Filters: 01-DAPI, 13-GFP and 20-Cy3 (Carl Zeiss Microscopy GmbH)

#### 2) Zeiss Axiovert 40 CFL Trinocular Inverted Fluorescence Phase Contrast Microscopy

- Model: Zeiss Axiovert 40c Base (Carl Zeiss Microscopy GmbH)
- Brightfield Illumination Type: Halogen
- Phase contrast: Condenser NA 0.2
- Fluorescence Light source: 50w Mercury w/ power supply (Carl Zeiss Microscopy GmbH)
- Camera: AxioCam MRm (Carl Zeiss Microscopy GmbH)
- Objectives: 2.5x, 5x, 10x objective (Carl Zeiss Microscopy GmbH)
- Filters: 01-DAPI, 13-GFP and 20-Cy3 (Carl Zeiss Microscopy GmbH)

### 3) Leica TCS SP5 II Confocal Microscope

To image the Fibroblast-led collective invasion models, a Leica TCS SP5 confocal microscope was used with 10x and 20x magnification.

- Model: LSM Leica TCS-SP5 II
- Bright field illumination: Halogen 100W bulb
- Fluorescence Light source: UV laser, Ar-laser, HeNe-laser
- Detector:
  - Transmitted light detector TCS SP5 DMI 6000 for brightfield
  - 2 confocal detectors with selected noise-reduced PMTs
  - 2 Hybrid GaAsP Detector for high sensitivity high speed imaging
- Objectives: 10x, 20x, 40x, 63x objective (Leica)
- Epi-Fluorescence Filter systems:
  - DAPI (BP 240-380 nm, LP 425 nm)
  - FITC (BP 450-490 nm, LP 515 nm)
  - PC5 (BP 515-560 nm, LP 590 nm)

### 4) Leica STED TCS SP8 3X Microscope

To image the immunofluorescence of 2D cultures, a Leica STED TCS SP8 3X was used with the confocal mode of microscopy

- Model: Leica Stellaris 8 STED
- Bright field illumination: Halogen 100W bulb
- Fluorescence Light source: STED laser
- Detector:
  - Transmitted light detector TCS SP5 DMI 6000 for brightfield
  - 2 confocal detectors with selected noise-reduced PMTs
  - 2 Hybrid GaAsP Detector for high sensitivity high speed imaging
- Objectives: 10x, 20x, 40x, 63x objective (Leica)
- Epi-Fluorescence Filter systems:
  - DAPI (405 nm)
  - Alexa488 (488 nm)
  - Cy3 (545 nm)

## B. Two-photon excitation FLIM microscopy

Fluorescent lifetime images were taken in cooperation with Prof. Jürgen Popp in Friedrich-Schiller-University of Jena.

### FLIM Microscopy:

- Microscope Frame: LSM510 Meta, Zeiss, Jena Germany
- Objective: 10×/NA 0.3 EC Plan-Neofluar  
Plan 40x/0.65 Ph2 M27
- Emission Filter: short pass filter 650nm (Semrock, USA),
- Single-band bandpass filter 458/64 nm (FF01-458/64-25 nm, Semrock, USA)
- Single-band bandpass filter 525/30 nm FF01-525/30-25 nm, Semrock, USA)
- Laser: continuous-wave neodymium vanadate laser
- Ti:sapphire Oscillator: (Mira HP, Coherent)
- OPO: optical parametric Oscillator (OPO, APE, Germany)
- 2P-FLIM detector: hybrid GaAsP detector (HPM-100-40, Becker & Hickl, Germany) and a workstation containing a time correlated single photon counting (TCSPC) module (SPC-150, Becker & Hickl, Germany)
- PMT: descanned photomultiplier tubes (Hamamatsu Photonics, Japan)

## 2.13 Data Analysis Software

- Bio1D software (Vilber-Lourmart Version 15.02)
- Fiji-imageJ 1.52p
- ImageJ based Plugin for measuring size of spheres and invasion area (Anna Rupp)
- ImageJ based Macro for measuring invasion radius (Jia Mei and Christian Siebenwirth)
- ImageJ based Macro for mitochondrial morphology analysis “Mito-Morphology”, by Ruben K. Dagda, Ph.D., University of Nevada School of Medicine  
([https://imagejdocu.tudor.lu/plugin/morphology/mitochondrial\\_morphology\\_macro\\_plugin/start](https://imagejdocu.tudor.lu/plugin/morphology/mitochondrial_morphology_macro_plugin/start))
- Leica software for confocal images processing

- Zeiss LSM Image Browser Version 4.2.0.121
- SPCImage Version 6.4
- AxioVision SE64 64bit Version 4.9.1.0
- GraphPad Prism 8 Version 8.0.1

### 3. Methods

#### 3.1 Cell culture 2D

All mammary carcinoma cell lines were cultured in 100 mm x 20 mm cell culture dishes. Fibroblast lines, which sometimes show reduced growth in dishes, were cultivated in T25 flasks. All cell culture media and solutions were pre-warmed to 37 °C before use.

##### **Cell culture procedure:**

2D cultures were passaged 1-3 x per week to keep, depending on growth rate. After a microscopic check of the cell status, old medium was removed and cells were washed with PBS. Then 1 mL Trypsin/ EDTA was added to T25 flasks and 2 mL to cell culture dishes. Samples were incubated in a 37 °C incubator for 5 minutes to detach the cells and complete detachment was verified microscopically after knocking sharply against the side of the dish or flask, respectively. To stop trypsinization, a 10-fold volume of fresh medium + FBS was added and cell clusters were dispersed by pipetting the cells up and down several times with a glass pipet. Then, according to the split ratio (mostly 1:5 or 1:3), a fraction of the cell suspension was transferred to a new labeled flask or dish. Culture medium was added up to 10 mL for dishes and 5 mL for T25 flasks. Dishes and flasks were gently moved to evenly distribute the cells before they were moved to the CO<sub>2</sub> incubator (5 % or 10 % CO<sub>2</sub>, depending on cell lines).

##### **Determining cell titers:**

To count the cells for seeding certain numbers of cells for experiments, the cell suspension was collected into tubes and vortexed to scatter cells. 10 µl of the cell suspension were pipetted into a Neubauer counting chamber. All cells in 4 squares were counted and the titer was calculated by the formula:

**Cell concentration**= Number of counted cells \* dilution factor/ (Number of counted squares) \* 10<sup>4</sup> cells/ mL

### **Growth curves after NCS treatment**

50 000 cells/ well of BJ1-hTert or HDF were seeded in duplicates or triplicates in 6-well plates and incubated in a 37 °C incubator overnight. On the second day, cells were treated with 1:500 diluted Neocarcinostatin (final conc. 1 µg/ mL in complete cell culture medium) for 60 minutes to induce DNA damage. The control group was treated with 1:500 diluted DMSO. Then the medium was changed to normal medium and the cells were incubated for 8 days, before they were harvested by trypsin and counted. For quantification, the cell numbers were normalized to the control groups. The plots and statistical analysis were done by Prism software.

### **Live-cell staining**

To distinguish different cell types in the co-culture system, fibroblast lines were always stained green (Vybrant™ CFDA SE Cell Tracer Kit, V12883) and mammary breast cancer lines were stained red/orange (CellTracker™ Orange CMTMR Dye, C2927).

Briefly, live cell dyes powder was dissolved in DMSO to 10 mM stock solution, and stored at 4 °C for further use. Before staining, the stock solution was diluted 1:10 000 into 37 °C pre-warmed PBS. Then, cell culture medium was removed from 2D cultured cells and the diluted dye solution was added. Cells were incubated for 15 minutes at 37 °C, then the dye solution was replaced with fresh cell culture medium. The stained cells were allowed to recover in the 37 °C incubator overnight before further manipulated.

### **Stable transfection**

To generate cell line MCF-7 (HGMU) pMcc-GFP-53BP1-PN #L, one day before transfection, 180 000 cells/ well were seeded in 2 mL medium without Pen/Strep into 6-well plates to ensure 50 % to 70 % confluence for transfection. On the next day, 7.5 µl lipofectamine™ 2000 was added to 125 µl Opti-MEM in a safe-lock tube and mixed by pipetting. 5 µg plasmid pMcc-GFP-53BP1-PN was added to 125 µl Opti-MEM in another safe-lock tube, mixed by pipetting and incubated for 5 min. The DNA-lipid complex was prepared by mixing both vials and incubating at room temperature for 15 min. The DNA-lipid-complex was

then pipetted on top of the medium and the sample was incubated overnight in a CO<sub>2</sub> incubator. On the next day, the medium was removed and the cells were gently washed with PBS buffer. The 500 µl Trypsin/ EDTA were added to each well and samples were incubated for 5 minutes at 37 °C to detach the cells. After washing and counting, 1 % and 10 % of the cells, respectively, were transferred to new 100 mm x 20 mm dishes with 10 mL fresh RPMI-1640 + 10 % FBS containing 0.3 µg/ mL puromycin for selection. Cells were incubated for at least two weeks in order to kill untransfected cells, with refreshing the puromycin-containing medium every 3-4 days. After colonies of puromycin-resistant cells have formed, they are individually harvested by adding a small drop of trypsin on the top of colony and incubating for 5 min. By pipetting up and down with 10 µl cell culture medium each colony was transferred to one single well of a 24-well plate. After adding 1 mL cell culture medium with 0.3 µg/ mL puromycin, the colonies were incubated to expand and finally tested by fluorescence microscopy for expression of the fluorophore-tagged transgene. Three successful clones were generated, of which #L was used in the experiments.

### **3.2 Cell culture 3D**

#### **3D cell culture in the ultra-low adhesion U-bottom plate**

Spheroid growth conditions were optimized in preliminary experiments with MCF-7 which showed that seeding of 1000 cells per well in 200 µL of medium consistently gave homogeneous spheroids. These conditions were kept constant for all breast cancer cell lines in monoculture. For coculture experiments, 1000 fibroblasts were added immediately or after formation of the breast cancer spheroid, depending on experiment type, as indicated in the results section.

Spheroids were recorded by bright-field light microscopy every three days after seeding until day 14. Maximum extension at the spheroid equator was measured by plugins based on Fiji-ImageJ. Plots of area as function of time were done by GraphPad PRISM 8.

### **3D cell culture in VitroGel system**

VitroGel is a hydrogel system which lets cells attach and provides cell-matrix interactions during 3D culture. The stiffness of the matrix can be adjusted by different dilution with cell suspension.

Before use VitroGel was pre-warmed to room temperature. For each well, 40  $\mu\text{L}$  VitroGel was diluted by adding 160  $\mu\text{L}$  Dilution Solution. Then 100  $\mu\text{L}$  cell suspension was added. According to the manual, the recommended cell titer is between  $0.5 \times 10^6$  and  $2 \times 10^6$  cells/ mL. Here,  $0.5 \times 10^6$  cells/ mL were used, thus finally each well contains 50 000 cells. The mixture was transferred to a 6-well plate, and the plate was gently tilted to make sure that the mixture covers the whole bottom. Introducing air bubbles was avoided. The plate was placed at room temperature for 20 minutes for gel formation. Then additional medium (500  $\mu\text{L}$ ) was added to prevent the gel from drying out. Plates were incubated in the 37 °C incubator and the medium was changed every 2 days to provide the fresh nutrition to the cells.

### **3D cell culture in CoSeedis™ system**

CoSeedis are agarose-based chips containing an array of conical microwells to force spatially confined growth of cell aggregates.

Before use the agarose chips were put into 6-well plates and equilibrated for at least 3 h in medium. After equilibrium, medium was removed. 10 mL cell suspension ( $2.5 \times 10^4$  cells/ mL) was prepared and 9.5 mL of this suspension were added to the chip. This results in approximately 1000 cells per microwell of the chip. After seeding, cells were allowed to settle down for 20 min before the plates were put into the 37 °C incubator. Images were taken by light microscopy before harvesting.

To harvest the (pseudo-)spheroids for protein isolation, the chip was flipped upside down in the 6-well plate. Then the plates were gently knocked on the desk to let (pseudo-)spheroids drop from the microwells into the medium. The medium was collected into 1.5 mL microtubes and (pseudo-)spheroids were collected by spinning down at 4 °C, 500 rcf for 5 min. After removing the

supernatant, (pseudo-)spheroids were washed with precooled PBS and collected again by centrifugation. After removing residual medium, samples were used for lysis.

### **3.3 Invasion of fibroblasts into cancer cell spheroids**

#### **Invasion of fibroblasts into breast cancer spheroids**

To observe whether fibroblasts can migrate into the solid and compacted spheroids, MCF-7 and BT474 cells were allowed to form spheroids 2 days before adding fibroblasts.

For differential staining of cancer cells and fibroblasts, BT474 cells were stained with CellTracker Orange one day before seeding, as described above, while MCF-7 cells stable transfected with pMcc-tagRFP-PN plasmid expressed red fluorescent protein. Fibroblasts were stained green with Vybrant live cell staining dye in 6-well plates as described above, 1 day before adding to the spheroids. 1000 breast cancer cells were seeded into ULA plate and allowed to form spheres for two days before 1000 fibroblasts were added. For each combination of cancer cell line and fibroblast strain, 4 replicates were seeded. Microscopic observation of migration started 2 h after fibroblast addition by epifluorescence microscopy; further images were taken after 6 h, 1 day, 2 days, 3 days and 5 days.

#### **Live-cell imaging of migration of BJ1-hTert into MCF-7 spheroids**

To track the movement of fibroblasts after seeding, 1000 fibroblasts that had been stained in green by live-cell staining on day before were added to 1-day old spheroids from MCF-7 tag-RFP cells. The plate was placed onto the stage of an Axio-Observer Z1 epifluorescence microscope equipped with mini-incubation system. The cultivation condition was the same as used normally, with 5 % CO<sub>2</sub>, 37 °C and air humidity 95 %. The movement of fibroblasts were monitored every 30 minutes for 50 hours after seeding, i.e., 100 images were taken in total.

For a quantitative evaluation, three individual fibroblasts were traced by using the “manual tracking” plugin in Fiji ImageJ software. The trajectories were displayed, and the coordinates of each timepoint were recorded. Because the spheroids were cultured in a U-bottom plate in cell culture medium, the position of the spheroids varied a little during the whole observation period, therefore, I also tracked the centroids of the spheroids.

The distance to the centroid of each fibroblast at each timepoint was calculated by the formulation of distance between two ordinates:

$$D = \sqrt{(x_1 - x_2)^2 + (y_1 - y_2)^2}$$

### **ROCK-inhibitor treatment of fibroblasts**

To investigate whether the ROCK-inhibitor will influence the migration of fibroblasts into the solid breast cancer cell spheroids, ROCK-inhibitor Y-27632 was added at different time points and to different cell lines. The stock concentration is 10 mg/ mL in DMSO solution. Stock was added into cell culture medium at a 1:1000 ratio, thus the final working concentration was 10  $\mu$ g/ mL during the experiment.

MCF-7 tagRFP spheroids were seeded into ULA plates two days before adding of fibroblasts. Part of the spheroids were treated with 10 $\mu$ g/ mL Y-27632 one day before coculturing, or with DMSO (1:1000) to serve as solvent control. 2D cultured BJ1-hTert were stained green by live-cell staining two days before coculturing and treated with Y-27632 or DMSO one day before coculturing.

After 24 h inhibitor treatment, MCF-7 tagRFP spheroids received fresh medium and BJ1-hTert cells were detached and collected in tubes for cell counting. 100  $\mu$ L fibroblast suspension containing 1000 cells with inhibitor-treated or mock-treated, were added to MCF-7 tagRFP spheroids. Then the medium was supplemented with 10  $\mu$ g/ mL Y-27632 in part of the samples to distinguish the long-term and short-term effects. Each group had 4 replicates.

Images were documented 30 min, 6 h, 1 day, 2 days, 3 days and 6 days after coculturing through Zeiss Axiovert 40 CFL microscopy.

### **Radiation effects on the migration of BJ1-hTert into MCF-7 spheroids**

To investigate whether irradiation affects the migration behavior of BJ1-hTert cells into solid breast cancer spheroids, MCF-7 spheroids and/or BJ1-hTert fibroblasts were irradiated before co-culture.

On the day before co-seeding, stained fibroblasts and/or 2-day-old spheroids were irradiated with 5 Gy or mock-treated. Samples were then placed in the incubator for 30 min recovery.

After recovery, BJ1-hTert cells were detached with trypsin and counted. 1000 irradiated or non-irradiated fibroblasts were then added to irradiated or non-irradiated MCF-7 tagRFP spheroids, in all 4 combinations. Samples were incubated at 37 °C. Migration processes were documented by the epifluorescence microscopy 2 h, 1 day, 3 days and 5 days after co-culture.

## **3.4 Invasion into invasion matrix**

### **Radiation effects on invasion of mono-culture fibroblasts and fibroblasts-led co-culture models**

To generate the invasion model, mammary carcinoma cells were seeded into ULA plates (1000 cells/ well) to form solid spheroids one day before adding 1000 fibroblasts. Fibroblast monocultures were also seeded on the second day (1000 cells/ well). On the third day, spheroids were X-ray irradiated with 5 Gy or mock-treated and then allowed to recover for 30 min at 37°C. In the meantime, Matrigel (Cultrex® Spheroid Invasion matrix) was thawed on ice. After the 30 min recovery period the medium covering the spheroids was carefully removed and 40 µl undiluted Matrigel was added to each well. After gel solidification for 1 hour at 37 °C, 150 µL complete medium was added to each well and the spheroids were again incubated at 37 °C, with one medium exchange after 7 days. Microscopic images were taken at day 1, 4, 7, 10 and

14 after irradiation and embedding.

Brightfield and low-resolution fluorescence pictures of the spheroids were taken with a Zeiss Axiovert 40 CFL inverted fluorescence phase contrast microscope, at 2.5x magnification. “Invasion area” of all images were analyzed by the ImageJ based plugins written by Anna Rupp (Rupp 2019) and the “invasion radius” was measured by ImageJ Macro coded by Christian Siebenwirth; the details were described in the “data analysis” section. All graphs, exponential fitting and statistical analysis was done by GraphPad Prism8 software. For each experimental group, eight replicates were seeded and 3 independent experiments were performed.

### **High-resolution imaging of fibroblast-led invasion model**

For high-resolution imaging, the MCF-7 tagRFP cell line was used, and BT474 cancer cells were stained red with live-cell staining one day before seeding. BJ1-hTert and HDF fibroblasts strains were stained in green one day before seeding. To ensure the invasion protrusions, solid spheres were formed one day before adding fibroblasts. After one day co-culture, spheroids were embedded in Invasion Matrix and images were taken 5 days after embedding by confocal microscopy (Leica STED TCS SP8 3X).

### **3.5 Foci counting assay**

MCF-7 cells stably transfected with pMcc-GFP-53BP1-PN plasmid were kept under puromycin selection until the experiment. For foci analysis, 1000 cells/well MCF-7 GFP-53BP1 cells were seeded into ULA plates with or without 1000 cells/well BJ1-hTert fibroblasts. One day after seeding, spheroids were irradiated with 5 Gy X-ray or mock-treated. Then plates were incubated at 37 °C in the incubator for recovery. 24 hours after irradiation, the spheroids were first fixed with 4 % PFA for 15 min, then washed 3 times with PBS buffer. Residual 53BP1 foci were imaged by Zeiss Axio-Observer Z1 with 10x objective. Z-stack images were obtained for each region of cells. The foci from 649-736 cells were counted for each sample and the distribution of numbers of foci was depicted

with Prism software.

### **3.6 Cryosection of mammary carcinoma cell spheroids and HE staining**

To investigate the composition and structure of 3D cultured mono- and co-cultured spheroids they were transferred to a 10\*10\*5 mm Tissue Tek cryomold after removing the medium. In the mold, residual medium traces were removed and then the spheroids were covered with Tissue Tek O.C.T. compound. The mold was put at -80 °C until the Tissue Tek O.C.T became solid. Afterwards the mold was stored in aluminum foil at -20 °C until slicing. The frozen spheres were cut using the Leica CM1900 rapid sectioning cryostat of the Department of Otolaryngology, LMU Klinikum Munich with help by laboratory assistants Claudia Boehland, Darko Libl and Gisela Kranz. 5 µm thick sections were transferred onto Superfrost Plus microscopy slides. Sectioned tissue slices were dried overnight at room temperature. On the second day, the slices were fixed with -20 °C acetone for 10 min and dried at room temperature for another 10 minutes. Slides were stored in aluminum foil at -20 °C until further staining.

CoSeedis agarose inserts were cut into small pieces containing 1-2 micromolds before transferring to cryomolds and then treated as described above for spheroids.

Before HE staining, the slides were thawed for 10 minutes at room temperature and then rehydrated at room temperature for 30 minutes. Slides were incubated in hemalum solution acid acc. to Mayer for 5 minutes. Then the slides were kept under running tap water for 10 minutes to change the pH of solution in order to convert hemalum solution from red to blue. Afterwards the slides were rinsed with dH<sub>2</sub>O. Then the slides were incubated in 0.5 % Eosin Y solution for 2 minutes and washed once using dH<sub>2</sub>O, followed by short immersions in a series of ethanol solutions: 50 % EtOH → 70 % EtOH → 80 % EtOH → 96 % EtOH → 100 % EtOH. After a short dipping in xylol, several drops of Eukitt Quick-hardening mounting medium were added and a cover slip was placed on top the slide. Slides were dried overnight and stored at room temperature for further observation.

### 3.7 Immunofluorescence staining of 2D tissue culture

For immunofluorescence staining, BJ1-hTert and HDF fibroblasts were grown in 6-well plates containing sterile 22 mm coverslips in each well. After removing the medium, cells were fixed and permeabilized for 15 min in 2 mL permeabilization buffer (2 % PFA in PBS). After 3 x 5 min washing steps in PBS + 0.15 % Triton X-100, the sample was blocked with blocking buffer (1 % BSA + 0.15 % Glycine in PBS) for 3 x 10 min. After carefully removing all liquid, 75  $\mu$ L of diluted primary antibody (see table 3.1) was pipetted onto the coverslip. The samples were incubated overnight at 4 °C in a humid box. To wash out the primary antibody, the slides were rinsed 5 min with PBS, 10 min with PBS + 0.15 % Triton X 100, and 5 min with PBS, before they were blocked for 7 min with blocking buffer. Then the specimen was incubated with fluorochrome-conjugated secondary antibody diluted in blocking buffer for 45 min in a humid chamber and in the 4 °C refrigerator. After washing in PBS (2 x 5 min), PBS + Triton (1 x 10 min) and PBS (2 x 7 min), DNA was stained with diluted DAPI solution (1:10 000 in PBS buffer) for 90 sec at room temperature, followed by 2 x 2 min washing steps in PBS. After removing all liquid, a small amount (15 – 20  $\mu$ L) of Prolong Gold was dropped on a microscopy slide and the coverslip was carefully placed onto the slide avoiding bubbles. Finally, the coverslip was sealed with nail polish and stored at 4 °C fridge in the dark.

Primary Antibody	Dilution in blocking solution	Secondary antibody	Dilution in blocking solution
Vimentin (D21H3) XP Rabbit mAb	1:100	Goat anti-rabbit Alexa Fluor 488	1:500

**Table 3.1:** Antibody dilution conditions for immunofluorescence

### 3.8 Western Blot

#### **Detection of EMT marker expression in 2D- and 3D-cultured mammary carcinoma cell lines**

Cells from 2D culture were harvested by trypsinization, counted and collected by centrifugation (Hettich centrifuge with 4 °C, 1720 rpm/ min for 5 min). After removing the supernatant, the cells were washed with cold PBS and centrifuged again. Cells were resuspended in lysis buffer (20 µL lysis buffer for 100 000 cells).

To prepare spheroid lysis samples, as a minimum 10 spheres with 1000 cells initial seeding or 1 sphere with 10 000 cells were used for 1 well for western blot detection. For BJ1-hTert 10 000-20 000 cells/ well were seeded into ULA plates for generating spheres. For mammary carcinoma cells lines, 1000 cells/ well were initially seeded into ULA plates. Medium was changed once at day 7 and at day 14 the spheroids were harvested by pipetting with cut tips into 1.5 mL safe lock tubes. Spheroids were collected by centrifuging (Hettich centrifuge with 4 °C, 1720 rpm/ min for 5 min), washed with cold PBS, collected again and then resuspended in lysis buffer. The amount of lysis buffer needed was estimated depending on pellet size.

#### **Sample preparation in general:**

To prepare lysis buffer, first 10x phosphatase Inhibitor (1 mL PBS + one tablet “PhosSTOP”) and 7x protease Inhibitor (1,5 mL PBS + one tablet “Complete Mini”) were prepared. For 2 mL lysis buffer, 200 µL 10x phosphatase inhibitor and 300 µL 7x protease inhibitor were added to 1,5 mL RIPA-Buffer. Cell pellets were resuspended in appropriate volumes of lysis buffer, vortexed briefly and then incubated for 10 min on ice followed by 10 min at 100 °C. After a few seconds centrifugation at 1000 rpm to spin down drops from the lid, samples were frozen at -20 °C overnight or 20 minutes. Then frozen extracts were vortexed until the extract gets “milky” and centrifuged at 4 °C, 11 000 rpm, for 5 minutes.

12 µL of extract supernatant were transferred to a fresh sample tube. After

adding 4  $\mu$ L 4x Lämmli buffer, the sample was incubated for 10 min at 95 °C and then stored on ice until gel loading. Remaining cell extracts were frozen again at -20 °C.

#### **Gel electrophoresis:**

4-20 % TGX stain free gels from Bio-Rad were used for Western Blot. 13.5  $\mu$ L were loaded per lane and the gel was run at 120 V for 75 min in 1 x Tris/Glycine/SDS running buffer.

#### **Membrane transfer and immune detection:**

Proteins were transferred onto nitrocellulose membrane by tank blot transfer overnight at 40 V or for 2 h at 200 mA (4 °C). After transfer, the membrane was cut in horizontal stripes, depending on the size of the proteins to be detected. After a short rinsing step in PBST washing buffer, the membranes were incubated for 1 h in blocking buffer (5 % milk or 1 x Roti-Block, see table 3.2) in PBST washing buffer), followed by incubation for 1 h at room temperature or overnight (see table 3.2) at 4 °C in 2 mL primary antibody solution on a rolling mixing device. Membranes were then washed 3 x 5 min with PBST washing buffer and subsequently incubated for 1 h with 20 mL secondary antibody solution under shaking. After the membrane was washed for 3 x 5 min with washing buffer, it was stored at 4 °C until detection.

Lumigen ECL, a substrate for HRP (= horseradish peroxidase), was used to detect the bands. The reaction was detected using the Chemi-Smart 5100 Chemiluminescence system (Vilber-Lourmat). Since ECL is light-sensitive, the following steps were carried out in the dark. The ECL reaction mixture was prepared according to the manufacturer's protocol, the membrane was incubated in the solution for 5 min and then placed in a plastic bag. After the ECL signal was recorded using the built-in Chemi-Capt program, in addition a photography of the blot was taken in order to determine the position of the size markers. Pictures were merged by ImageJ and Bio1D software (Vilber-Lourmat Ver. 15.02) was used to quantify the relative expression of the markers.

Primary Antibody	Size of protein [kDa]	Dilution in blocking solution	Secondary antibody
Rb- $\alpha$ -Fibronectin	220	1:4000, 1x Roti-Block, 1 h RT	0.5 $\mu$ L/ mL blocking solution Goat- $\alpha$ -rabbit IgG HRP
Rb- $\alpha$ -E-Cadherin	135	1:1000, 5 % milk in PBST, 1 h RT	0.5 $\mu$ L/ mL blocking solution Goat- $\alpha$ -rabbit IgG HRP
M- $\alpha$ -Smooth Muscle Actin	45	1:1000, 5 % milk in PBST, 1 h RT	0.25 $\mu$ L/ mL blocking solution Goat- $\alpha$ -mouse IgG HRP
Rb- $\alpha$ -N-Cadherin	140	1:1000, 5 % milk in PBST, 1 h RT	0.5 $\mu$ L/ mL blocking solution Goat- $\alpha$ -rabbit IgG HRP
M- $\alpha$ -Cytokeratin 18	40-68	1:1000, 5 % milk in PBST, 1 h RT	0.25 $\mu$ L/ mL blocking solution Goat- $\alpha$ -mouse IgG HRP
Rb- $\alpha$ -Vimentin	58	1:4000, 1x Roti-Block, 4 °C o.n.	0.5 $\mu$ L/ mL blocking solution Goat- $\alpha$ -rabbit IgG HRP
M- $\alpha$ -EpCAM	38	1:1000, 5 % milk in PBST, 4 °C o.n.	0.25 $\mu$ L/ mL blocking solution Goat- $\alpha$ -mouse IgG HRP
Rb- $\alpha$ -Histone H2B	>25	1:5000, 5 % milk in PBST, 1 h RT	0.5 $\mu$ L/ mL blocking solution Goat- $\alpha$ -rabbit IgG HRP

**Table 3.2:** Blocking and antibody dilution conditions for Western Blot analysis.

### 3.9 Mitochondria staining assay

200 000 cells/ well were seeded on sterilized 22 mm cover slips in 6-well plates and incubated overnight. A stock solution of MitoTracker was prepared by dissolving the lyophilized MitoTracker Red CMXRos in DMSO to a final

concentration of 1 mM. For staining, this solution was freshly diluted 1:10 000 in PBS and 2 mL were given to each slide after having removed the medium. After incubation at 37 °C for 20 minutes, the cells were washed in fresh, pre-warmed growth medium twice. To fix the cells, the medium was replaced with freshly prepared, 37 °C pre-warmed growth medium with 3.7 % PFA and samples were incubated at 37 °C for another 15 min. Then the samples were washed twice with PBS. Then 2 mL PBS containing 1.5 % Triton X-100 were added to permeabilize cells. After 10 min incubation at room temperature, the slides were washed 3 times with PBS buffer.

To stain F-actin, Phalloidin solution was prepared and diluted in PBS according to the manufacturer's protocol. After staining at room temperature for 60 min, the slides were washed with PBS for 3 times. To stain the the DNA, DAPI stock solution was diluted 1:10 000 in PBS, and slides were incubated for 90 sec followed by 3 washes with PBS. Then slides with a small drop of ProLong Gold reagent to avoid bleaching of fluorescent signal were placed on top the coverslips and sealed with nail polish. Samples were dried overnight at room temperature. Images were taken using a Zeiss Axiovert 40 CFL inverted fluorescence phase contrast microscope, at 100x magnification with Immersol™ 518N Carl Zeiss immersion oil.

The images were analyzed by the plugin written by Stefan Strack, Ph.D., University of Iowa and modified and amplified by Ruben K. Dagda, Ph.D., University of Nevada School of Medicine as described in *section 3.11.5*.

Graphical display and statistical analysis were done by GraphPad Prism8 software.

### **3.10 Investigation of metabolic state by multi-model microscopy**

#### **Two-photon excitation FLIM detection setup**

All non-linear multimodal images were acquired in collaboration with the group of Prof. J. Popp, Friedrich-Schiller-University Jena.

**Imaging Description:**

In our experiment, the laser serving as the Stokes beam is a Ti:sapphire oscillator. The generated ultrashort pulse by the Ti:Sa oscillator is centered around 832 nm with 2-3 ps duration and a repetition rate of 76 MHz. Using an Optical Parametric Oscillator (OPO), the laser wavelength is then upconverted to around 1050 nm, which is also served as TPEF excitation for NAD(P)H and FAD as the double frequency/half wavelength of 418 nm overlaps with the excitation for these two components. After frequency conversion, the laser is coupled into a LSM510 laser scanning microscope and pass a 600 nm long-pass dichroic mirror before being focused on the objective. A 10x/NA 0.3 EC Plan-Neofluar or a 40x/0.65 Ph2 M27 objective have been used to observe the region of interests in 3D Invasion model or 2D irradiated samples, respectively. TPEF excited autofluorescence signals are collected by objectives and then reflected to 2P-FLIM detector by a 600 nm short pass dichroic mirror. Then 2P-FLIM signals are filtered by a 650 nm short pass filter and a 458/64 nm bandpass filter which has a bandpass spectral range of 426-490 nm for detecting NAD(P)H signal; for detecting FAD, a 525/30 nm bandpass filter is employed before the signal is detected by 2P-FLIM module.

**Images Acquisition:**

For the FLIM metabolic imaging data we used 150\*150  $\mu\text{m}$  big images with 0.29  $\mu\text{m}$  resolution, which is 512\* 512 pixel for each acquisition image. and averaging of two frames. LSM image examiner, LSM image browser and SPCImage software are applied to analyze the images.

**Detecting radiation effect on 2D cultured MCF7 and BJ1-hTert cells by fluorescent lifetime imaging (FLIM)**

To determine changes in the metabolic state after irradiation, 2D cultured MCF-7 and BJ1-hTert cells grown on coverslips were irradiated with X-rays at a dose of 15 Gy and fixed at 4 different time points (10 min, 2 h, 24 h and 48 h) post-irradiation by incubating for 2 min in 4 % para-formaldehyde, followed by two

washing steps with PBS. Mock-treated cells were also fixed on these time points. Afterwards coverslips were mounted on glass slides with a drop of Prolong Gold and sealed with transparent nail polish.

FLIM images were recorded. Two-photon fluorescence lifetime imaging was used to measure the reduced nicotinamide adenine dinucleotide (NAD(P)H), which can be separated by double-exponential decay into short lifetime component ( $a_1$ ): free NAD(P)H and long lifetime component ( $a_2$ ): protein-bound NAD(P)H. According to the distinct variations in the relative proportion of these two components before and after irradiation, we can judge whether these cells rely more on glycolysis or oxidative phosphorylation to produce energy after irradiation. Lifetime of FAD is also recorded and analyzed with double-exponential fitting.

### **Investigation of fibroblast-led invasion model**

To investigate the metabolic states in the fibroblast-led collective invasion model by FLIM, coculture spheroids were established and embedded as described above and matrix plugs were carefully taken out of the ULA plates and transferred onto 35 mm Ibidi glass bottom plates with segmentation inserts. To avoid drying out, a small drop of cell culture medium was added. The imaging process is similar as above, here using 10x objective to have larger images of fibroblast-led invasion spheroids. Both NAD(P)H and FAD lifetime were detected and analyzed for each view.

## **3.11 Data Analysis**

### **3.11.1 Analysis of size of spheroids**

For measurements of spheroid area, a plugin developed in our lab based on Fiji software (<https://imagej.net/Fiji>) was used (Rupp 2019). To measure spheroid area at the widest extension (spheroid equator), semi-automatic segmentation was used and the spheroid area determined in pixels was

converted into  $\mu\text{m}^2$ . Input parameters are the magnification and the image quality (Figure 3.1). If the image quality is very high, definition of the spheroid is based on grey-value differences. If the quality is high but entrapments are visible, definition of the spheroid is manually supported by a definition of ROI function. In case the quality is poor with suboptimal background, and manual background definition step is included.

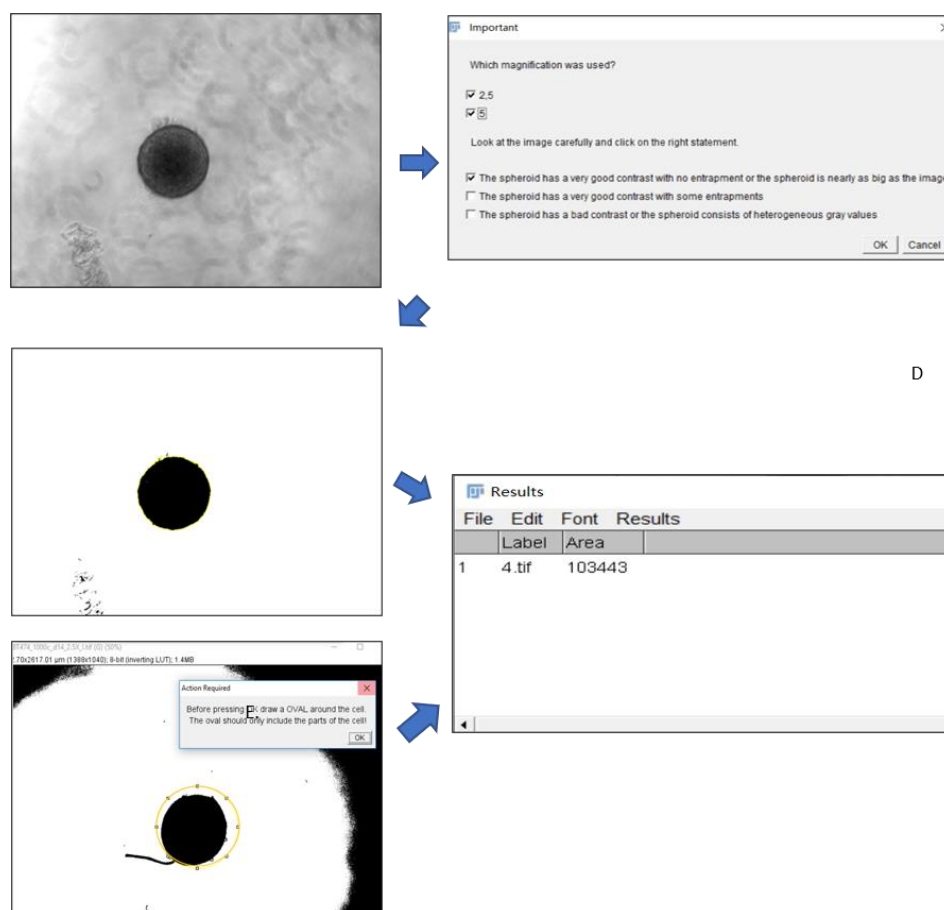


**Figure 3.1:** Schematic diagram of the ImageJ based plugins for spheroids area measurement written by our group.

### 3.11.2 Analysis of invasion area

The plugin for determination of invaded area was also developed by Rupp 2019; it is also based on Fiji software (<https://imagej.net/Fiji>). To determine invaded area, the compact spheroid core was determined by segmentation as described

in 3.11.1 and removed from the image. Then the pixels occupied by invaded cells was determined after manual threshold determination and converted into  $\mu\text{m}^2$  values. According to the equation: *Invasion area equals total area minus core area*, the area occupied by invading cells was determined. All data were then analyzed by GraphPad Prism 8 software, figure 3.2.

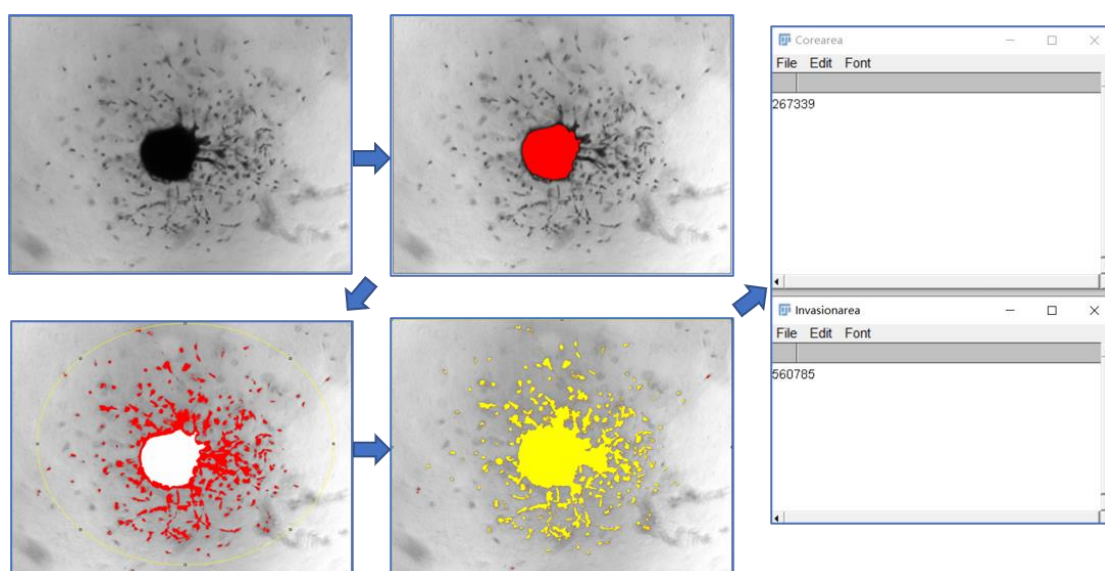


**Figure 3.2:** Schematic diagram of the ImageJ based plugins for invasion area measurement written by our group.

### 3.11.3 Analysis of Invasion distance radius

For image analysis, a self-written macro was used based on the ImageJ distribution Fiji. The image processing is briefly described here and Figure 3.3. In a first step, background/illumination correction was performed by dividing the original image by the original image blurred with a Gaussian blur filter (sigma = 40 px). In this way, uneven background, e.g., due to illumination, is leveled, while structures smaller than the spheroid core can be preserved. The corrected image was analyzed twice:

- For the determination of the spheroid center
- For the determination of the cell distribution around the spheroid center

After applying a Gaussian blur with a sigma of about half the cell size the spheroid core was homogenized, the center region was detected by the auto threshold method “Minimum” and object detection was performed by the “Analyze Particles” command. In the second processing step of the corrected image, the auto threshold method “Otsu” was used for definition of pixels representing cells (white). Polar transformation of the resulting image using the previously defined core center as center coordinates allowed then to plot the pixels (white) representing cells as a function of the radius  $r$  and angle  $\Theta$ . The relative yield of white pixels (representing cells) for the range  $\Theta = 0^\circ$  to  $360^\circ$  as function of the radius  $r$  was then plotted and used for further analysis. For these plots,  $r$  was limited to  $\leq 520$  px (half of the image height) to provide equal weighting of the cell distribution in all directions ( $\Theta$ ).

Assuming that two cell distributions contribute to this curve (core cells and invading cells), two characteristic parameters could be extracted from this plot. 1) The core radius, which was defined as the radius, from which less than 50 % of the pixels represent cells and the 2) maximum invasion radius representing the end of the curve. The latter was determined by performing a linear fit on the end of the curve and calculating the x-interception.

The core radius and the maximum invasion were determined for each replicate and group results are presented as scatterplot. All linear fitting process, graphs and plots drawing and statistical analysis are made by GraphPad Prism8 software. About 10 % of the images were excluded because strong background artefacts dominated and could not be corrected sufficiently by the illumination correction.

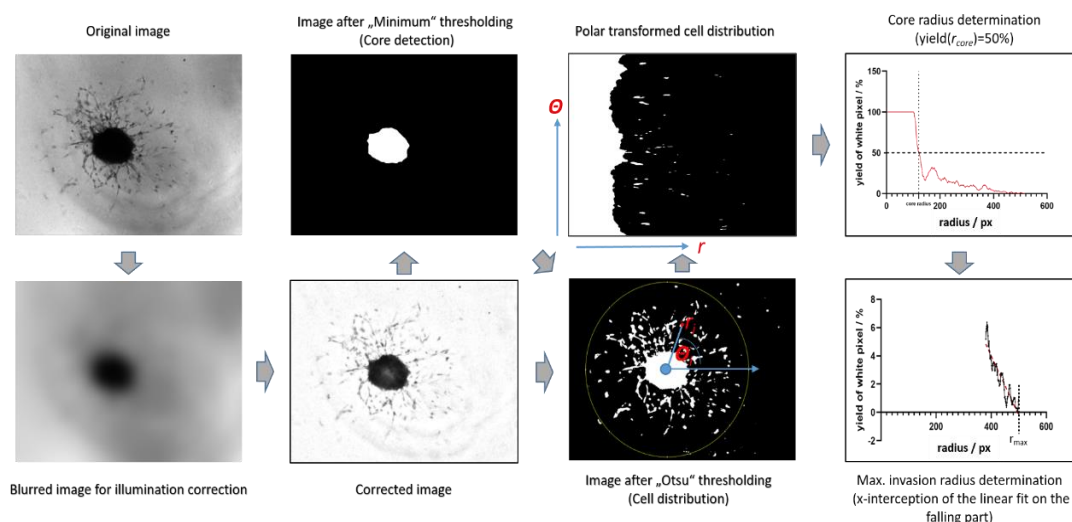


**Figure 3.3:** Schematic diagram of the ImageJ based plugins for invasion radius measurement written by our group.

### 3.11.4 Analysis of FLIM images with SPCImage

Analysis of metabolic changes through FLIM images was performed by B&H SPCImage software. Here, two ways of FLIM image analysis were introduced.

#### a) Double-exponential decay analysis

An overview of NAD(P)H or FAD lifetime was determined by a double-exponential decay analysis. Briefly, through the analysis, each molecule will be divided into two components: long lifetime component (such as, protein-bound NAD(P)H, free FAD) and short lifetime component (e.g., free NAD(P)H and protein-bound FAD). After analyzing, each pixel has the parameters as: amplitude of two components ( $a_1$ ,  $a_2$ ), long-/ short- lifetime ( $\tau_1$  and  $\tau_2$ ) and intensity of the pixel. These yield color-coded images reflecting the amplitude-weighted lifetime ( $\tau_m$ ).

#### b) Phasor plot analysis

Phasor plot analysis is also done within SPCImage Software. After double-

exponential decay analysis, the decay data of each individual pixels can be transformed and expressed as phase and amplitude values in a polar diagram (Becker 2010). Regardless the position of the pixels in the images, all dots having similar decay features form a cluster in the phasor plot. Choosing the region of interests, molecules from some specific region can be selected (e.g., cytosolic or nucleus). Image segmentation could be performed via the phasor plot. Therefore, those metabolic co-enzymes which certainly were involved in energy production can be analyzed for estimating the metabolic states. This enables us to distinguish the specific parts of molecules from overall in the whole cells.

### **3.11.5 Analysis of Mitochondrial morphology**

The macro MitoMorphology, designed by Ruben K. Dagda (2010), allows to measure the mitochondrial interconnectivity and elongation of immune-stained mitochondria within cells. This macro contains three steps: Firstly, the cell of interest is selected with the polygon selection tool; then, automatic thresholding is performed in the red channel (where the mitochondria are depicted), but the user can optimize thresholding manually. The program determines various parameters, including mitochondrial counts, total area of mitochondria, cellular area, mitochondria content, perimeter of mitochondria, circularity of mitochondria, average perimeter of mitochondria, average circularity of mitochondria, average area of mitochondria, area/perimeter, area/perimeter normalized to minor axis, minor axis and area/perimeter normalized to circularity. Circularity is used for estimating the elongation of mitochondria; and the average area/ perimeter ratio is sensitive for normal to highly interconnected mitochondria. The average area/ perimeter ratio normalized to the minor axis (assuming that mitochondria are considered as ellipses) accounts for conditions that can induce mitochondrial swelling.

## 4. Results

*All figures shown in results and appendix can also be found in the enclosed CD. Part of the presented results were published in Radiation Oncology, 2021, 16(1):159. This concerns figures 4.2, 4.6, 4.7, 4.8, 4.9, 4.10, 4.11, 4.12, 4.13, 4.14, 4.23, 4.24, 4.25, 4.26, 4.27, 4.28 and table 4.2.*

*Part of the images shown were taken by students whom I co-supervised, in an effort to prepare high quality figures for the publication.*

### 4.1 Characterization of growth characteristics of mammary carcinoma cell lines MCF-7, BT474, MDA-MB-231 and SkBr3

#### 4.1.1 Different morphology of mammary carcinoma lines cultured in 2D

BT474, MCF-7 and SkBr3 are described as luminal breast cancer cell lines, while MDA-MB-231 is a claudin-low triple-negative cell line with a more mesenchymal phenotype. All four cell lines are frequently used in breast cancer research. To verify described phenotypes, the mammary carcinoma cells were first cultivated on a traditional two-dimensional flat surface. Figure 4.1 shows the morphology of the cell lines in 2D culture. Images were taken by Anika Geiger for her Master Thesis, which I co-supervised (Geiger 2019). MCF-7 cells exhibit a polygonal morphology and form compact colonies with a cobble-stone appearance. SkBr3 cells exhibit a similar cell morphology, but form colonies that have a patchier appearance. BT474 form small but tight clusters containing several cells, which appear to display a fierce cell-cell adhesion. In contrast, MDA-MB-231 cells show an elongated and spindle-like morphology and cells have only loose contact. These growth characteristics agree with previous descriptions (Kenny et al. 2007).

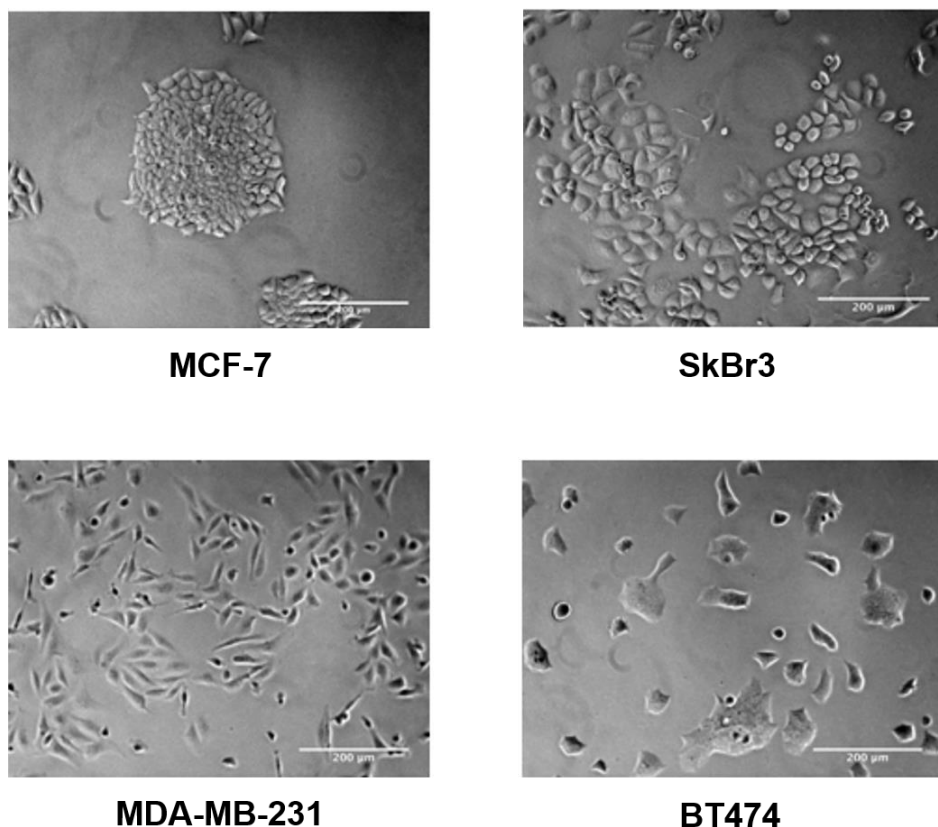


**Figure 4.1:** Transmission light images of different mammary carcinoma cell lines in 2D cell culture. Images were taken at different time points due to the different cell growth rate. Magnification: 10x, scale bar is 200  $\mu\text{m}$ .

#### 4.1.2 Different morphology of mammary carcinoma lines cultured in 3D

##### **Scaffold-free system: Ultra-low adhesion plates**

To observe the different morphologies of 3D-cultured mammary carcinoma cell lines, the four different breast cancer cell lines were seeded into ultra-low adhesion (ULA)-plates at 1000 cells/well. Seeded cells were observed photographically under light microscopy every three days until day 14 (Figure 4.2). Only two cell lines, MCF-7 and BT474, can form solid spheroids with compact margins and different appearance of rim and inner core, which may be due to necrotic regions in the core. According to the four types of classification of 3D structures of breast cancer cell lines proposed by Kenny and co-workers (Kenny et al. 2007), MCF-7 and BT474 belong to the “Mass”

growth type. Compared to the other three breast cancer cell lines, the growth velocity of MCF-7 is much faster, which is shown by the larger spheroid size. With increasing cultivation time, the shape of the MCF-7 spheroids becomes more irregular, which may indicate some heterogeneity in growth rates between individual cells and their descendants. SkBr3 and MDA-MB-231 cells can only form loose aggregates. According to Kenny et al. (2007), SkBr3 cells aggregate into grape-like structure with disorganized nucleus and poor cell-cell adhesion. The structure of the MDA-MB-231 aggregate is similar to the SkBr3 aggregate at the beginning, but with increasing incubation time the structure appears to become denser, see Figure 4.2.

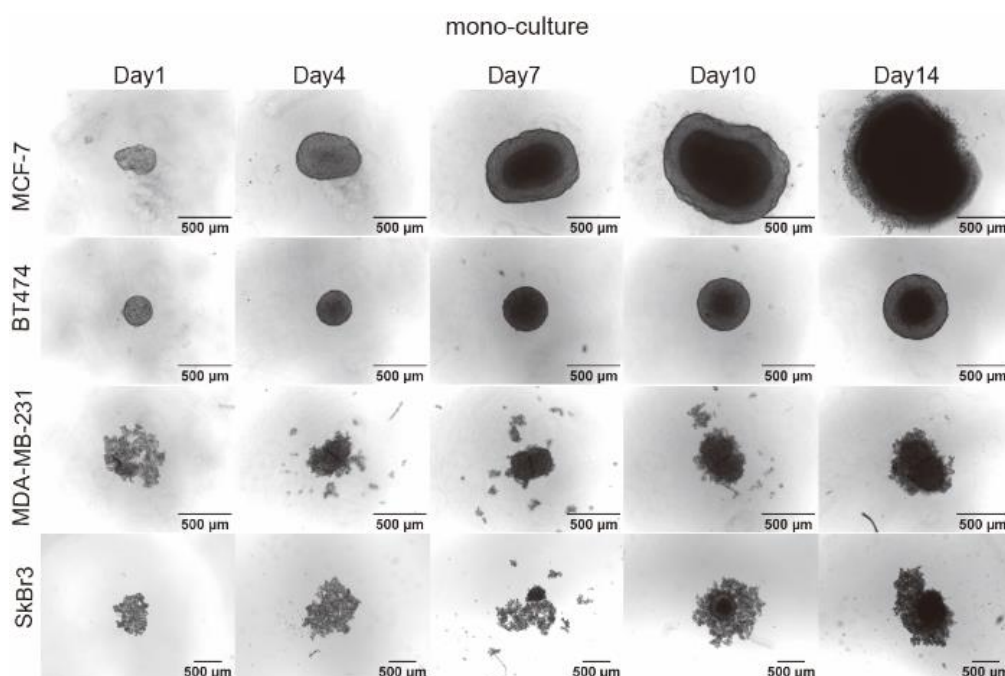


**Figure 4.2:** Spheroid formation of four breast cancer cell lines MCF-7, BT474, MDA-MB-231 and SkBr3 mono-cultured in ultra-low adhesion plates. 1000 cells per well of breast cancer cells were seeded initially. Microscopy images were taken on days 1, 4, 7, 10, 14 after seeding. Size bars are 500 µm. This figure was taken by Kristina Berner and Felix Thoma during an internship which I co-supervised.

### Scaffold-free system: CoSeedies system

3D CoSeedis™ is a scaffold-free 3D cell-culture system consisting of an

agarose-based chip containing an array of conical microwells. It allows the formation of spheroids even for non-spheroidal cell aggregates in a reproducible manner. As seen in Figure 4.3, the microwell structure enhances the aggregation of non-spheroidal cells, like MDA-MB-231 and SkBr3 cell lines.

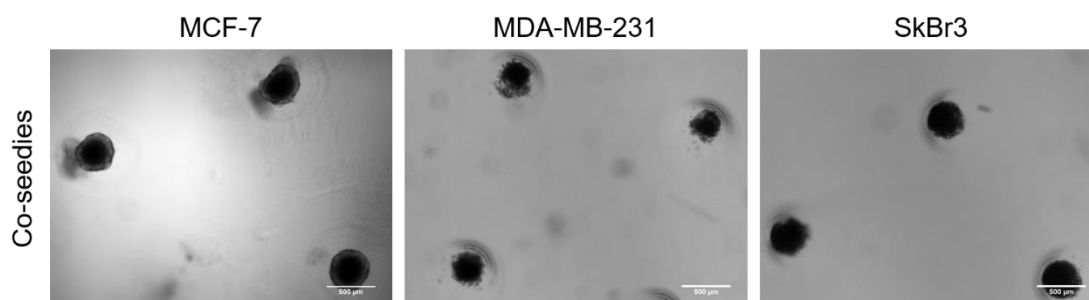


**Figure 4.3:** Spheroid formation of MCF-7, MDA-MB-231 and SkBr3 mono-cultured in 3D CoSeedies™ scaffolds. 1000 cells per well of breast cancer cells were seeded initially. Microscopy images were taken on day 9 after seeding. Size bars are 500 µm. The images were taken by Laura Mataite during a research course.

### Scaffold System: VitroGel

VitroGel 3D High Concentration is a hydrogel system which allows cells growing in a scaffold-based matrix system. The tunable concentration of VitroGel by dilution simply with water enables the cells to grow in different hydrogel strength. After optimizing the dilution ratio, here VitroGel was first diluted 1:4 with ddH<sub>2</sub>O. Then 200 µl diluted VitroGel was mixed with 100 µl MCF-7 cell suspension (containing 50000 cells in total), yielding a total volume of 300 µl /well in 24-well multi-well plates. Three days after seeding, images were taken through bright-field microscopy (Figure 4.4). Several clusters of MCF-7 cells were localized in the matrix. In VitroGel, MCF-7 spheroids exhibit the same “Mass” growth type as was observed when cultured in 3D ULA plates. Since the spheroids grow from a single cell, it takes longer to form spheroids with sizes comparable to those obtained in ULA plates. Furthermore, spheroids grown in VitroGel appear more heterogenous. Therefore, in the following experiments, ULA plates were used for generating the 3D structures to investigate their characteristics and the influence of radiation on them.

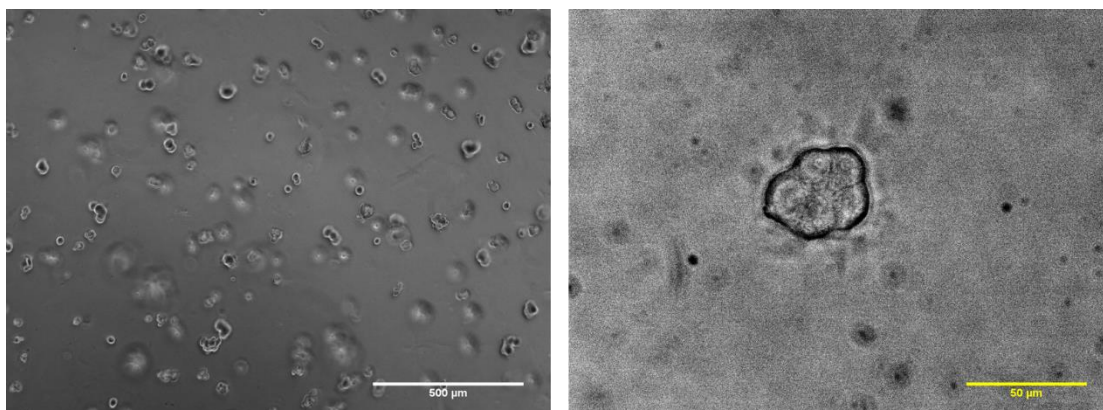


**Figure 4.4:** Spheroid formation of breast cancer cell line MCF-7 in scaffold-based 3D VitroGel™ (TheWell Bioscience) matrix. 50000 MCF-7 cells in 100  $\mu$ l cell suspension were mixed with diluted VitroGel. Microscopy images were taken on day 4 after seeding with 5x and 40x objectives. White size bar is 500  $\mu$ m, yellow size bar is 50  $\mu$ m.

### **Cryo-sectioning and HE-staining of 3D structures**

To assess the inner structure of 3D-cultured breast cancer spheroids and aggregates, cells were first grown in ULA plates or CoSeedies micromolds to form (pseudo)-spheres, then cryo-sectioned and stained using Hematoxylin-Eosin (HE)-staining. Hematoxylin binds to basophilic structures, is used as a nuclear stain and also stains rough endoplasmic reticulum, ribosomes, collagen, myelin, elastic fibers and acid mucins in blue or dark purple; Eosin stains acidophilic structures like proteins in the cytoplasm and extracellular matrix in pink. HE staining is one of the most popular methods used in histology and widely used in medical diagnosis and shows the general layout and distribution of cells and tissue structures. To confirm the inner mass of the 3D structures of solid spheres from different cell types, HE staining was performed. The results indicate that MCF-7 and BT474 cells appear more densely compacted at the outer rim of the spheroids than in the core region after cultivation on ULA-plates (Figure 4.5). SkBr3 cell pseudo-spheroids formed in CoSeedies appear more homogeneous compared with MCF-7 grown in CoSeedies. MDA-MB-231 cells grow rather poorly in CoSeedies and did not reach sufficient compactness.

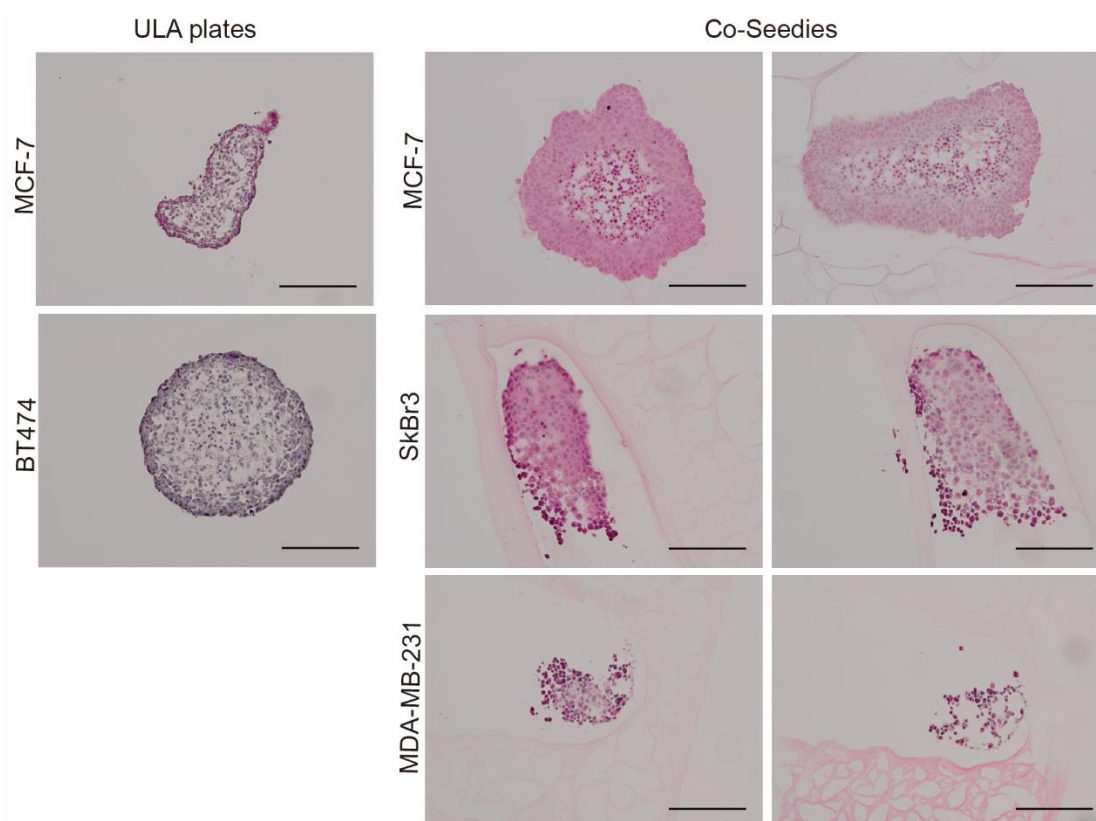


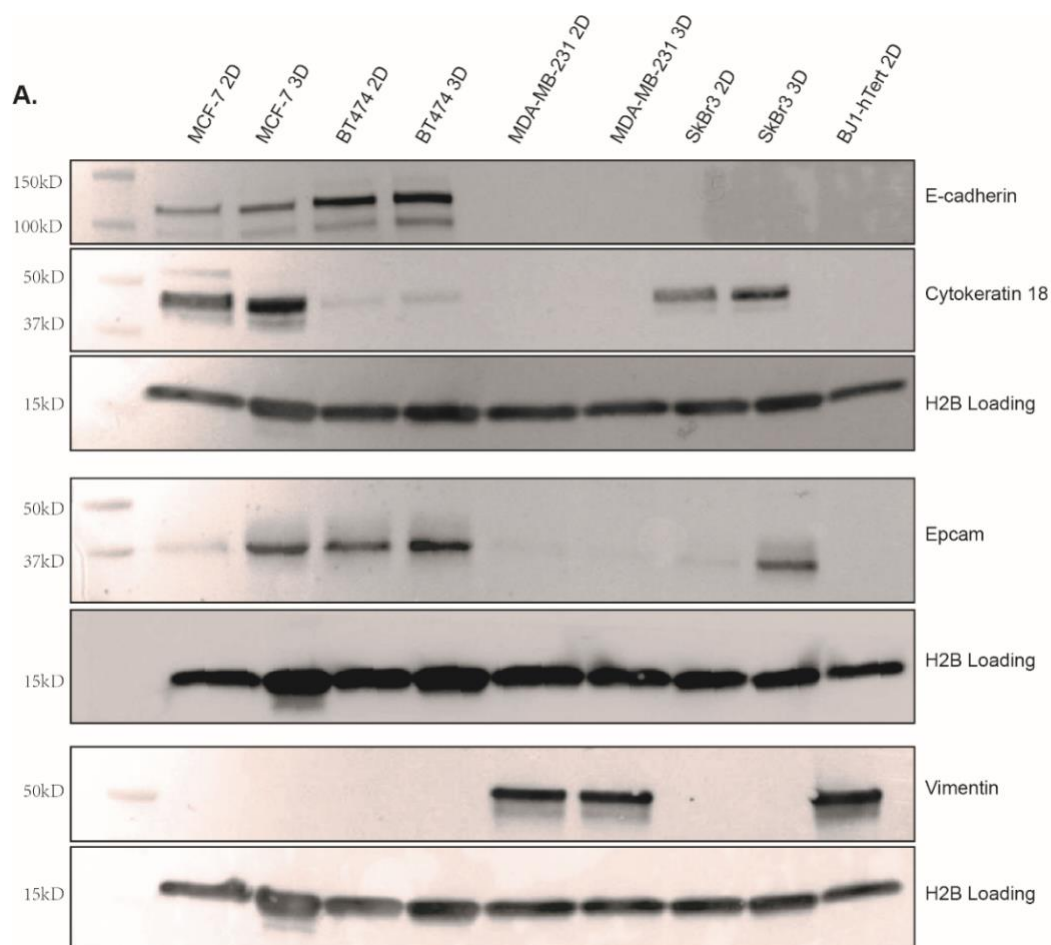
**Figure 4.5:** HE staining of cryosections of spheroids grown for 15 days on ULA plates (left) or of cell aggregates grown for 9 days in 3D CoSeedis™ scaffolds (right). Size bars are 200  $\mu\text{m}$ . The images were taken by Annika Geiger and Laura Mataite.

In conclusion, MCF-7 and BT474 cells are able to form solid spheroids. SkBr3 cells form loose aggregates in liquid, and somewhat more compact structures when forced to grow in a confined space. MDA-MB-231 cells form loose aggregates in liquid, but grow poorly in confined space.

#### 4.1.3 Western Blot detection of EMT marker proteins in 2D and 3D cultured mammary carcinoma cells

The observed differences in 2D and 3D growth characteristics may correlate with differences in the expression of surface proteins that differ between cells with more epithelial character and those with more mesenchymal character.

Some of these proteins are known as markers for epithelial-mesenchymal transitions (EMT). It has been shown that the expression of some of the EMT markers differs between 2D and 3D cultured cells (Fontana et al. 2019). Expression of several epithelial and mesenchymal marker proteins in the four breast cancer cell lines after cultivation both in 2D and 3D was assessed by western blotting. BJ1-hTert fibroblasts were used as a positive control for a mesenchymal expression type. MCF-7 and BT474 express E-cadherin and EpCAM, and MCF-7 cells in addition express cytokeratin 18 (Figure 4.6), indicating an epithelial phenotype. SkBr3 cells do not express E-cadherin, but are positive for cytokeratin 18 and EpCAM expression. In MCF-7 and SkBr3 cells, EpCAM expression increases upon 3D cultivation compared to 2D. MDA-MB-231 cells do not express these epithelial markers, but rather the mesenchymal marker vimentin (Figure 4.6). These results confirm published data that formation of compact spheroids correlates with expression of E-cadherin (Manuel Iglesias et al. 2013).



---

**Figure 4.6:** Western blot of EMT markers in mammary carcinoma cell lines MCF-7, BT474, MDA-MB-231, and SkBr3 cultured in 2D and 3D conditions. For control BJ1-hTert fibroblasts grown in 2D are introduced as typical mesenchymal cells. Detection of E-cadherin (135 kDa), cytokeratin 18 (40-68 kDa), EpCAM (38 kDa) and vimentin (58 kDa) are shown, together with Histone H2B (~25 kDa) loading controls from the respective blots. The blots shown here were prepared by Kristina Berner and Felix Thoma.

#### **4.1.4 Invasiveness of breast cancer cell lines into a basal membrane-like matrix**

To study the invasion behavior of the four mammary carcinoma cell lines, MCF-7, BT474, SkBr3 and MDA-MB-231 cells were first seeded into ULA plates and then embedded in a commercially available extracellular matrix blend comprised of basement membrane extract, derived from murine EHS sarcoma cells, and collagen I, from bovine extensor tendons (Cultrex® Spheroid Invasion Matrix). MCF-7 and BT474 cells are not able to invade into the surrounding matrix, which further confirms their epithelial-like phenotype (Figure 4.7), whereas MDA-MB-231 cells exhibit star-like protrusions and invade into the matrix. SkBr3 cells show only some cell shedding, but not star-like invasion.

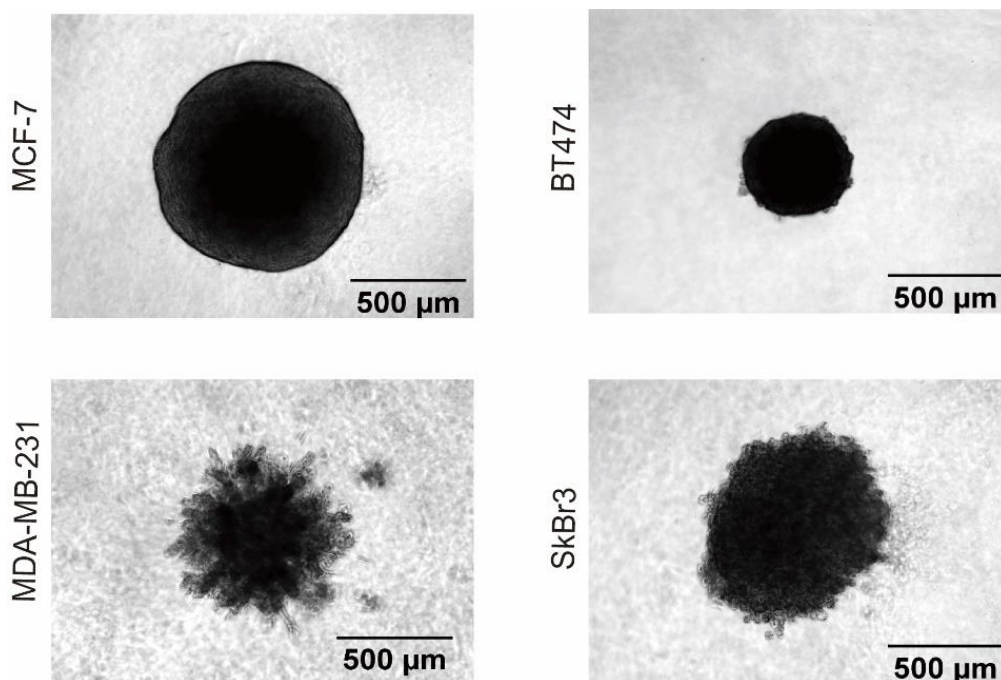


**Figure 4.7:** Invasion capability of breast cancer cells after embedding of spheroids / 3D aggregates into Spheroid Invasion Matrix. Images were taken on day 7 after embedding. Size bars are 500  $\mu\text{m}$ . The images were prepared by Kristina Berner and Felix Thoma.

### Conclusion of Chapter 4.1

MCF-7 and BT474 cells are chosen for further experiments because of their epithelial phenotype, formation of solid spheroids and inability to invade into matrix.

### 4.2 Characterization of spheroids obtained by co-culture of breast cancer cells and fibroblasts

A major aim of this work was to investigate the effect fibroblasts have on growth, radiation sensitivity and invasion capabilities of mammary carcinoma cells with epithelial characteristics. In particular, it was of interest to develop a model for

fibroblast-led invasion mechanisms where cancer cells opportunistically make use of tracks in the extracellular matrix formed by fibroblasts or even are pulled along by the fibroblasts. It is well known that cancer-associated fibroblasts affect cancer cell behavior by a variety of different mechanisms, including paracrine communication. In order to reduce the complexity of the system, normal skin fibroblasts were used here rather than cancer-associated fibroblasts.

#### 4.2.1 Characterization of BJ1-hTert foreskin or HDF skin fibroblasts

Immortalized human foreskin fibroblasts (BJ1-hTert) and human dermal fibroblasts (HDF) were used. First, their mesenchymal phenotype was confirmed by western blotting and Immunofluorescence staining. As expected, both fibroblast strains express the mesenchymal markers N-cadherin and vimentin (Figure 4.8). BJ1-hTert cells also express  $\alpha$ -SMA, which is a marker for activated fibroblasts. In addition, some fibroblasts show multipolar morphology, which is an indicator of fibroblast activation (Figure 4.9).

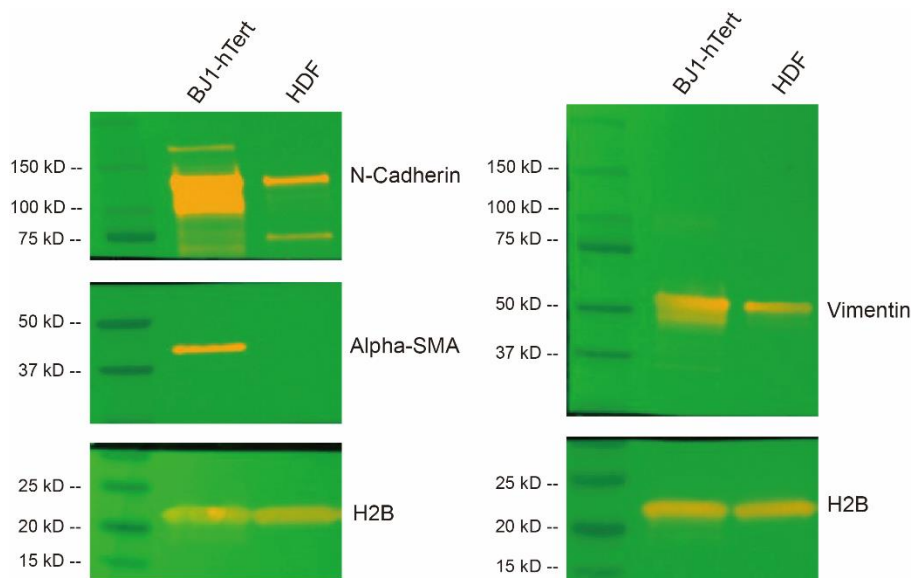


**Figure 4.8:** Expression of EMT markers vimentin (58 kDa), N-cadherin (140 kDa) and marker of fibroblast activation,  $\alpha$ -SMA (42 kDa), in BJ1-hTert and HDF fibroblasts cultivated in 2D, together with the respective Histone H2B (~25 kDa) loading controls.

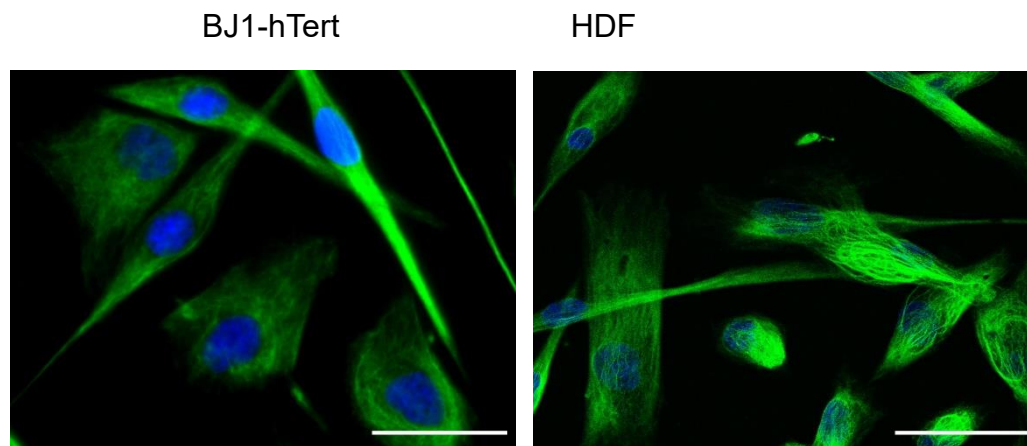


**Figure 4.9:** Expression of multi-polar growth in BJ1-hTert and HDF detected by immunofluorescence staining of vimentin and DAPI staining of cell nuclei. White size bar is 50  $\mu\text{m}$ . The HDF image was prepared by Kristina Berner and Felix Thoma.

#### 4.2.2 Morphology and growth of fibroblast lines cultured in 3D

To investigate spheroid formation and proliferation of 3D cultured fibroblasts, 1000 cells of BJ1-hTert and HDF per well were seeded in ULA plates. Both BJ1-hTert and HDF fibroblasts form compact spheroids upon cultivation in ULA plates, but they proliferate very poorly in these conditions (Figure 4.10). The spheroid size remains largely constant even 14 days after seeding.

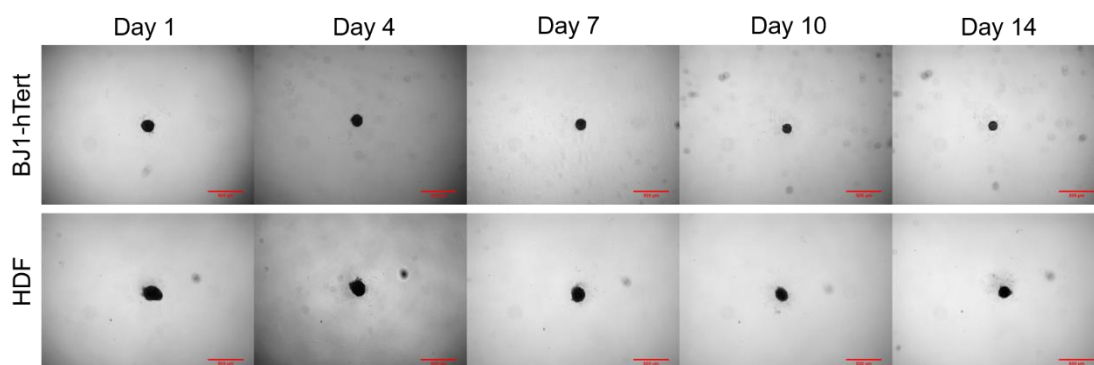


**Figure 4.10:** Spheroid growth in BJ1-hTert and HDF fibroblasts in ULA plates. 1000 fibroblasts per well were seeded in mono-culture. Microscopic images were taken on days 1, 4, 7, 10, 14 after seeding. Size bars are 500  $\mu\text{m}$ .

### **4.2.3 Characterization of spheroids obtained by coculture of breast cancer cells with BJ1-hTert or HDF fibroblasts in 3D ULA plates**

To investigate the effect of co-cultivated fibroblasts on breast cancer spheroids, the breast cancer cells were seeded into ULA plates together with BJ1-hTert foreskin or HDF skin fibroblasts. In addition to MCF-7 and BT474, which form compact spheroids, also SkBr3 and MDA-MB231 were tested in order to determine if the presence of fibroblasts alters the spheroid formation ability of these cell lines. Each 1000 cancer cells/well plus 1000 fibroblasts/well were seeded. Spheroid formation and growth was observed under light microscopy and pictures were taken every three days until day 14. Figure 4.11 shows the microscopic images and Figure 4.12 shows the growth curves. In comparison to the cancer cell monocultures (see figure 4.2) little difference in the structure and final sizes of MCF-7 and BT474 aggregates compared to the monocultures is seen. MDA-MB-231 aggregates appear more compact after addition of fibroblasts, while SkBr3 + fibroblast cocultures appear to grow better than the SkBr3 monocultures. Spheroid growth was recorded by determining the area of the spheroid at its equatorial plane from microscopic images.

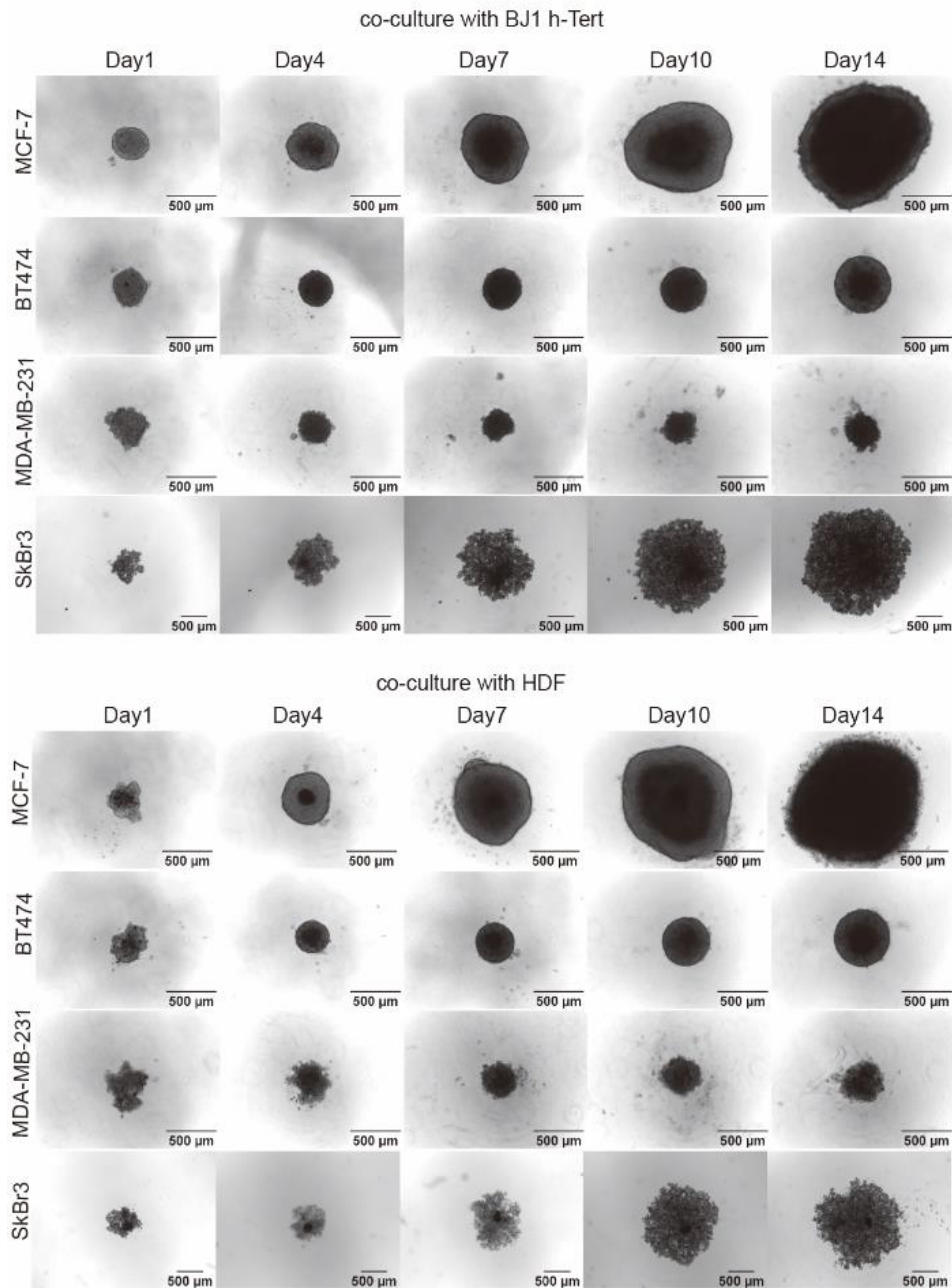


**Figure 4.11:** Spheroid growth in breast cancer cell lines MCF-7, BT474, MDA-MD-231 and SkBr3 in coculture with fibroblast strains BJ1-hTert and HDF. In co-culture 1000 cancer cells and 1000 BJ1-hTert or HDF fibroblasts were seeded together. Microscopic images were taken on days 1, 4, 7, 10, 14 after seeding. Size bars are 500  $\mu\text{m}$ . The images were prepared by Kristina Berner and Felix Thoma.

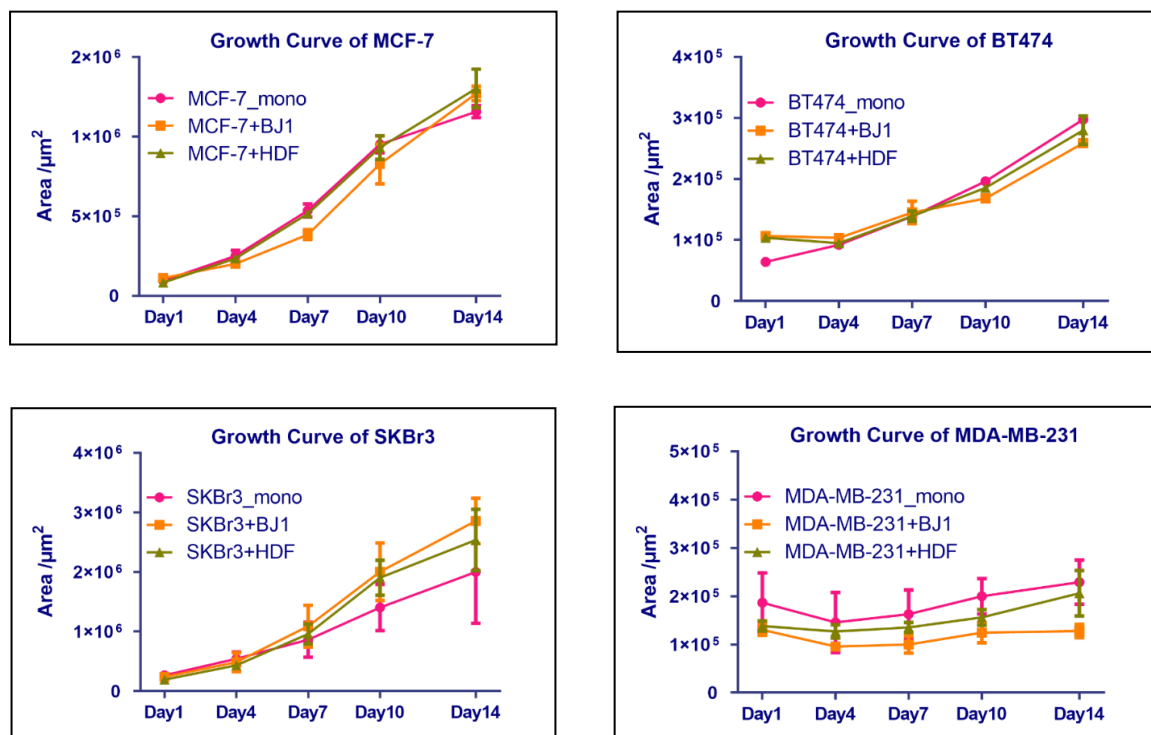


**Figure 4.12:** Growth curve of 4 mammary carcinoma cell lines in monoculture or coculture with BJ1-hTert and HDF, respectively. Mean  $\pm$  SD from three biological replicates is shown.

## Conclusion of Chapter 4.2

BJ1-hTert and HDF fibroblasts form 3D spheroids, but exhibit poor proliferation under these conditions. Cocultivation with fibroblasts has little effect on the final size of MCF-7 and BT474 spheroids.

## 4.3 Radiation effects on growth of breast cancer cell monoculture and in coculture spheroids

### 4.3.1 Radiation effects on spheroid size

To investigate the influence of irradiation on spheroid growth, spheroids were irradiated 1 day after seeding with 5 Gy, a dose in the order of fraction doses in

radiotherapy, and microscopically observed until day 14. Both mono- and coculture cancer cell spheroids exhibit a growth delay after irradiation compared to mock-treated controls (Figure 4.13). Spheroid areas at the equatorial plane were determined by image analysis (Figure 4.14 A). Unirradiated MCF-7 spheroids enter a plateau phase after day 10. Therefore, exponential fitting of spherical size data was performed for each individual MCF-7 spheroid from day 1 to day 10 to determine their growth rate ( $k$ ) and size on day 0 ( $Y_0$ ). In the case of BT474, fitting was performed from day 1 to day 14 (Figure 4.14 A). For MCF-7, spheroid sizes on day 0 (corresponding to day 1 after seeding) were not different between mono- and coculture, although 2000 cells were seeded in coculture vs 1000 cells in monoculture. This presumably reflects the fast growth of the MCF-7 cells. In contrast, the size of coculture BT474 spheroids is about 60 % larger than the size of monoculture spheroids on day 0 and this difference is significant.

Growth rates were found to be significantly smaller for cocultures compared to monoculture spheroids in spite of their comparable final sizes (Figure 4.14 B). Because of competing effects of cell number, cells size and compaction on spheroid size, the biological significance for observed differences in growth rate estimates between mono- and coculture spheroids is not clear at present.

When comparing the same type of spheroid with and without irradiation, the initial spheroid size is the same and thus when comparing the same type of spheroid with and without irradiation uncertainties associated with growth rate estimation should play a lesser role. As indicated in Figure 4.14 B, for MCF-7, mean growth rates were reduced by about 1/3 after irradiation in monoculture ( $k = (0.188 \pm 0.013)/d$  at 0 Gy and  $k = (0.124 \pm 0.009)/d$  at 5 Gy) and coculture ( $k = (0.179 \pm 0.020)/d$  at 0 Gy and  $k = (0.111 \pm 0.010)/d$  at 5 Gy). The effect of irradiation was less pronounced in the case of BT474: in monocultures, the mean growth rate was reduced by about 20 % ( $k = (0.106 \pm 0.013)/d$  at 0 Gy and  $k = (0.086 \pm 0.009)/d$  at 5 Gy), whereas in cocultures, the difference was about 30 % ( $k = (0.067 \pm 0.015)/d$  vs  $k = (0.048 \pm 0.012)/d$ ). Overall, relative growth delays appear largely comparable in mono- and coculture spheroids when the uncertainties of the analysis are taken into account.

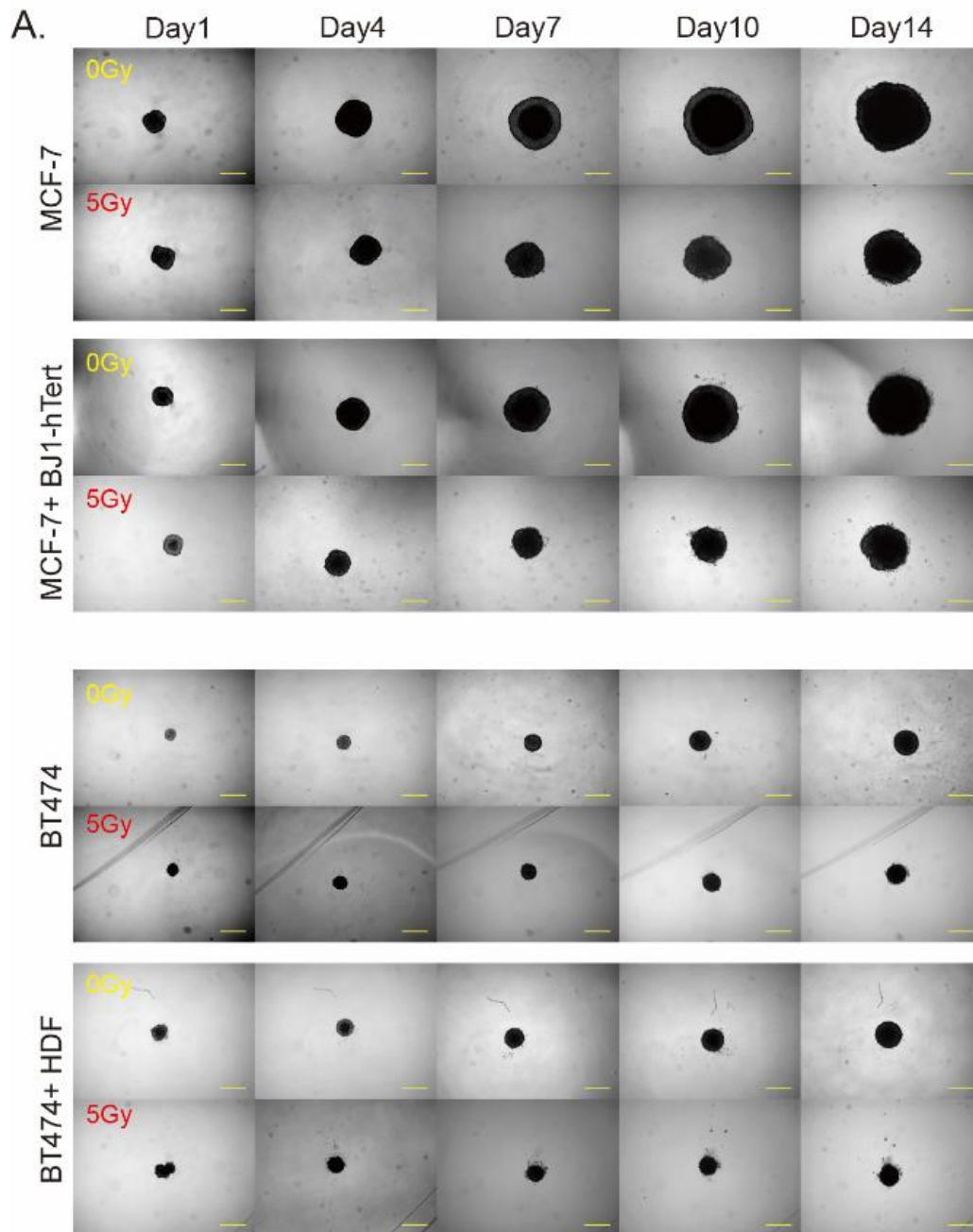


**Figure 4.13:** Spheroid growth delay after irradiation. A. Each 1000 cancer cells were seeded alone or together with 1000 fibroblasts in ULA plates to form spheroids. One day after seeding, spheroids were irradiated with 5 Gy or mock-treated. Spheroid growth was recorded over 14 days, starting on day 1 after irradiation. Size bars are 500  $\mu\text{m}$ .

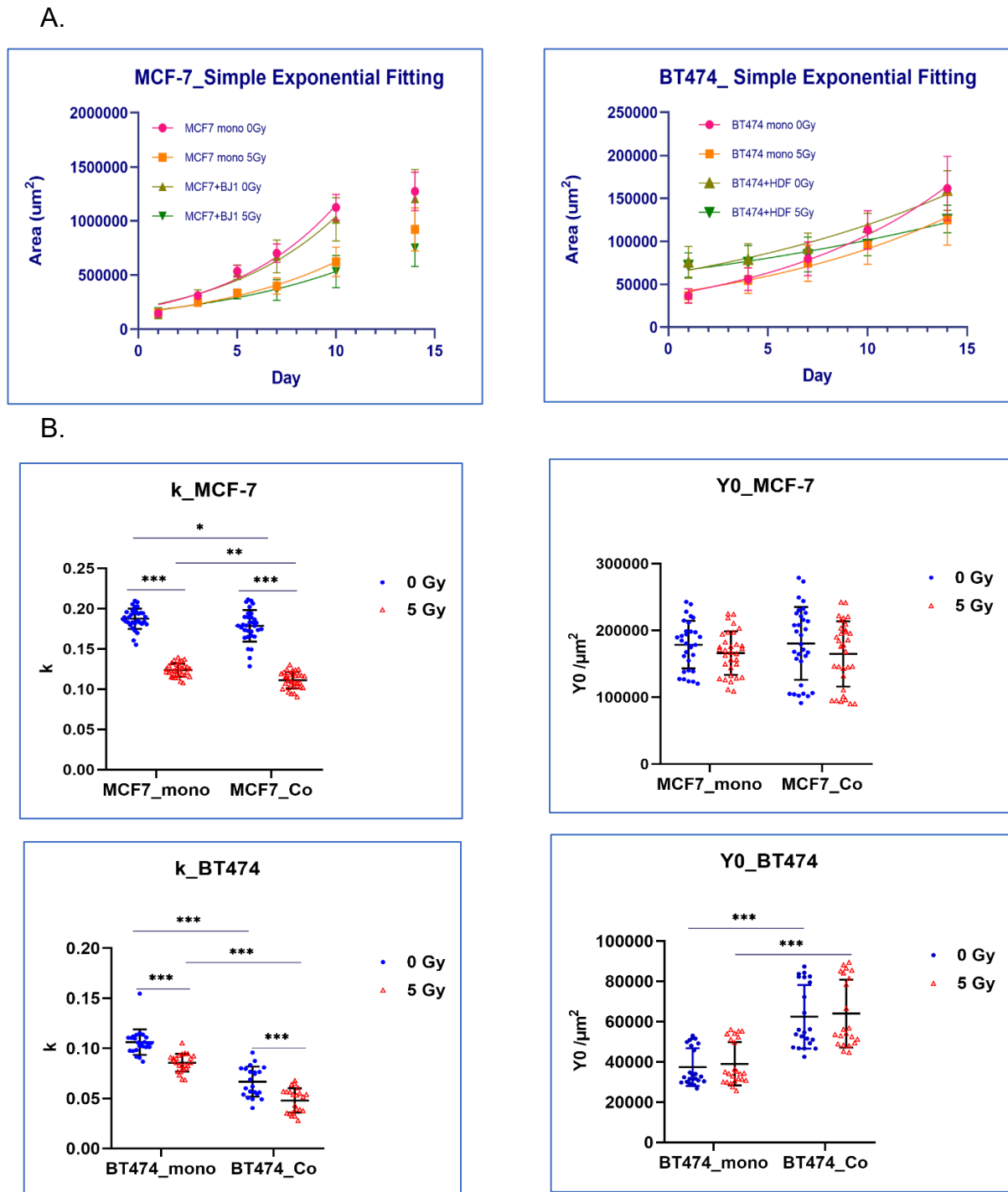


**Figure 4.14:** Spheroid area was determined by image analysis and recorded as function of time after 5 Gy irradiation. Indicated are mean and SD from 3 to 4 independent experiments with 8 replicates each. A. Growth can be described by an exponential fit (solid lines) between days 1 and 10 for MCF-7, and between days 1 and 14 for BT474. B. Results of exponential fitting of individual growth curves for each spheroid, with  $k$  indicating the growth rate and  $Y_0$  indicating spheroids size on

day 1 after irradiation. All statistical analyses were performed by Tukey multiple comparisons test following two-way ANOVA. \*, \*\*, and \*\*\* represent  $p < 0.05$ ,  $p < 0.001$  and  $p < 0.0001$ .

#### **4.3.2 Repair of double-strand breaks in MCF-7 monoculture and MCF-7 + BJ1-hTert coculture 3D spheroids**

A major factor determining the radiosensitivity of cells is their ability to repair DNA double-strand breaks (DSB). 53BP1 proteins accumulate at DSB sites to form microscopically detectable foci upon fluorescence staining or tagging and quantitation of residual 53BP1 foci after repair incubation is frequently used to measure DSB repair capacity.

To test whether DSB repair in MCF-7 cells is affected by the presence of fibroblasts, MCF-7 cells were stably transfected with plasmid pMCC-53BP1-GFP-pn. 1000 cells/ well of MCF-7 53BP1-GFP with or without 1000 cells/ well of BJ1-hTert fibroblasts were seeded in ULA plates and allowed to form spheroids for 1 day before spheroids were irradiated with 5 Gy. After recovery for 24 hours after irradiation the spheroids were fixed with 4 % PFA and then stained with DAPI for visualization of cell nuclei. Foci were observed by epifluorescence microscopy and z-stack images were taken to get the overview of residual foci (Figure 4.15). Residual foci were counted manually in 649-736 cells per sample in two independent experiments.

The results indicate that 24 hours post-irradiation only about 20-30 % of cells contain 53BP1 foci and the distribution of foci numbers is not different between monoculture and coculture cells (Sidak's multiple comparison test following two-way ANOVA was used to test the significance). Most of the cells have no foci 24 h after 5 Gy irradiation. The percentage of cells with only one residual focus in coculture is comparable to monoculture spheroids also in the remaining foci groups, no significant difference was seen between monoculture groups and coculture groups (Table 4.1 and Figure 4.16)

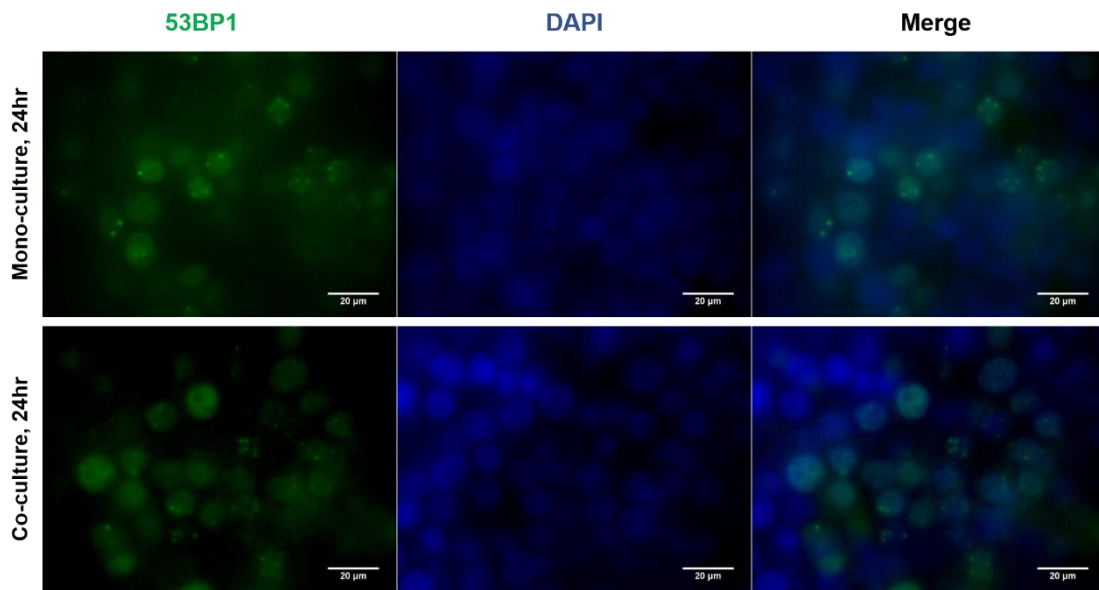


**Figure 4.15:** Foci formation 24 hours post 5 Gy irradiation treatment in MCF-7 monoculture and MCF-7 + BJ1-hTert coculture spheroids. MCF-7 cells express 53BP1-GFP and foci are depicted in green. DAPI staining shows the cell nucleus. White scale bar is 20  $\mu$ m.

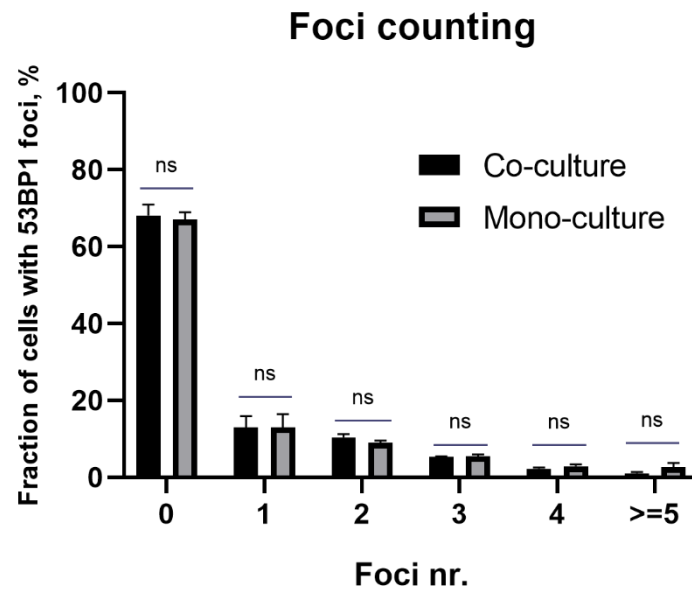
Co-culture						
Foci Nr.	0	1	2	3	4	$\geq 5$
Cell Nr_1st	491.00	76.00	69.00	38.00	17.00	9.00
Cell Nr_2nd	446.00	102.00	74.00	35.00	13.00	5.00
Cell Nr_1st %	70.14	10.86	9.86	5.43	2.43	1.29
Cell Nr_2nd %	66.07	15.11	10.96	5.19	1.93	0.74
%Average	68.11	12.98	10.41	5.31	2.18	1.01
%SD	2.88	3.01	0.78	0.17	0.36	0.39

Mono-culture						
Foci Nr.	0	1	2	3	4	$\geq 5$
Cell Nr_1st	444.00	68.00	61.00	33.00	21.00	22.00
Cell Nr_2nd	485.00	114.00	63.00	43.00	19.00	14.00
Cell Nr_1st %	68.41	10.48	9.40	5.08	3.24	3.39
Cell Nr_2nd %	65.72	15.45	8.54	5.83	2.57	1.90
%Average	67.07	12.96	8.97	5.46	2.91	2.64
%SD	1.91	3.51	0.61	0.52	0.47	1.06

**Table 4.1:** Quantification of Foci formation 24 hours post 5 Gy irradiation treatment in MCF-7 monoculture and MCF-7 + BJ1-hTert coculture spheroids. Average fraction of

cells containing a given number of foci and SD from 2 independent experiments are given.



**Figure 4.16:** Levels of residual 53BP1 foci in MCF-7 monoculture and MCF-7 + BJ1-hTert coculture spheroids. Fractions of cells with different number of foci are shown. Sidak's multiple comparisons test following two-way ANOVA was used to detect significant differences between the means of the monoculture and the coculture group. A  $p$  value  $\leq 0.05$  was considered statistically significant.

### Conclusion of chapter 4.3

In MCF7 + BJ1-hTert and BT474 + HDF, the presence of the fibroblasts has no major effect of spheroid growth after irradiation. Repair of radiation-induced DSB was not affected by the presence of BJ1-hTert in MCF-7 spheroids.

## 4.4 Migration of fibroblasts into mammary carcinoma spheroids

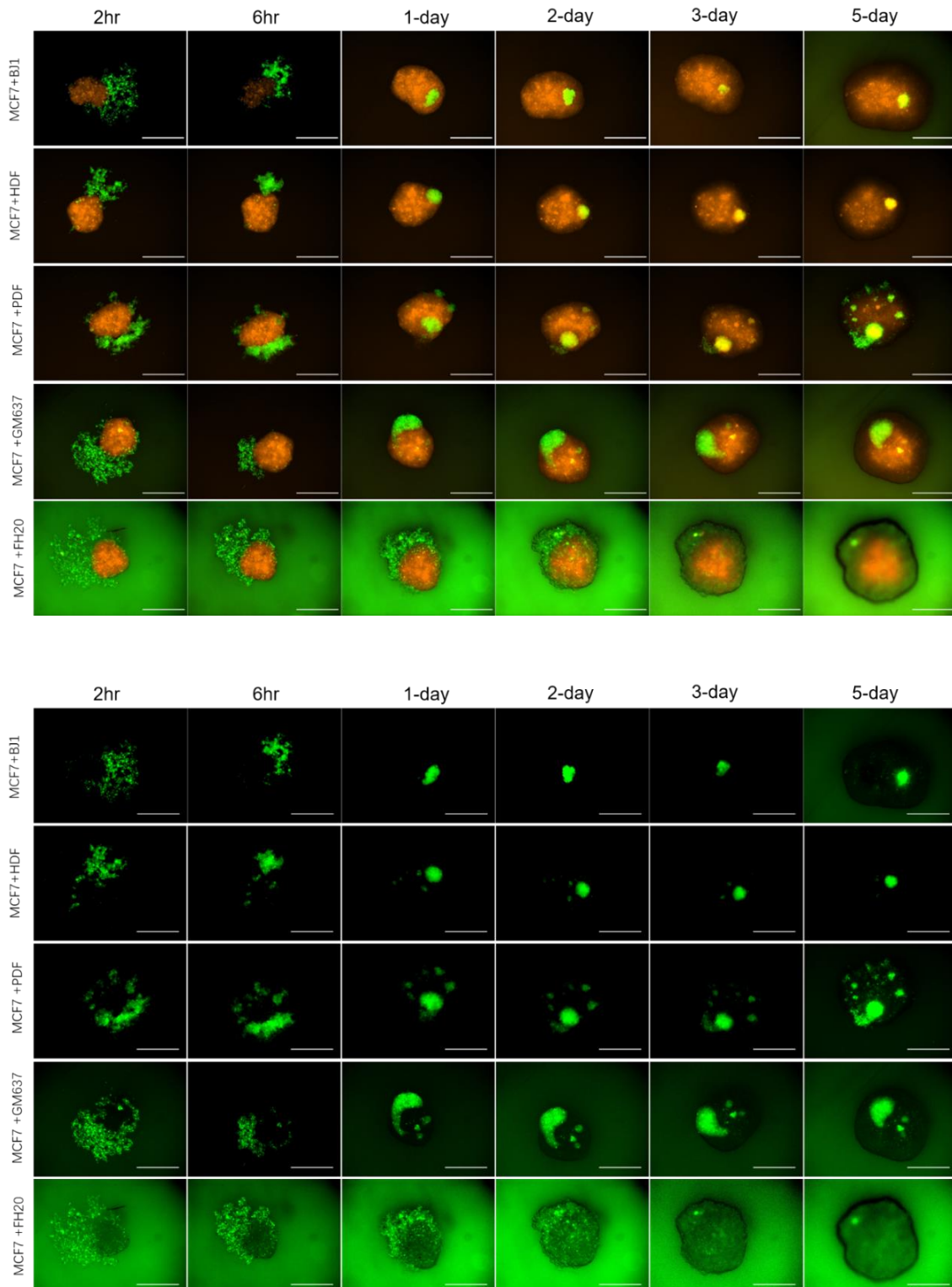
### 4.4.1 Migration of fibroblasts into MCF-7 and BT474 spheroids

Wenzel et al. (Wenzel et al. 2015) proposed coculture spheroids of fibroblasts and cancer cells as models for fibrotic invasive processes and recruitment of

---

fibroblasts to cancer cells. They identify three phases upon adding of fetal fibroblasts to T47D breast cancer spheroids on day 4 after breast cancer cell seeding: i) Fibroblasts gather as clusters on the spheroid surface, ii) fibroblast clusters are invaginated, iii) fibroblasts spread within the spheroid. They claim having observed the same phases in MCF-7 cells, albeit without showing the data.

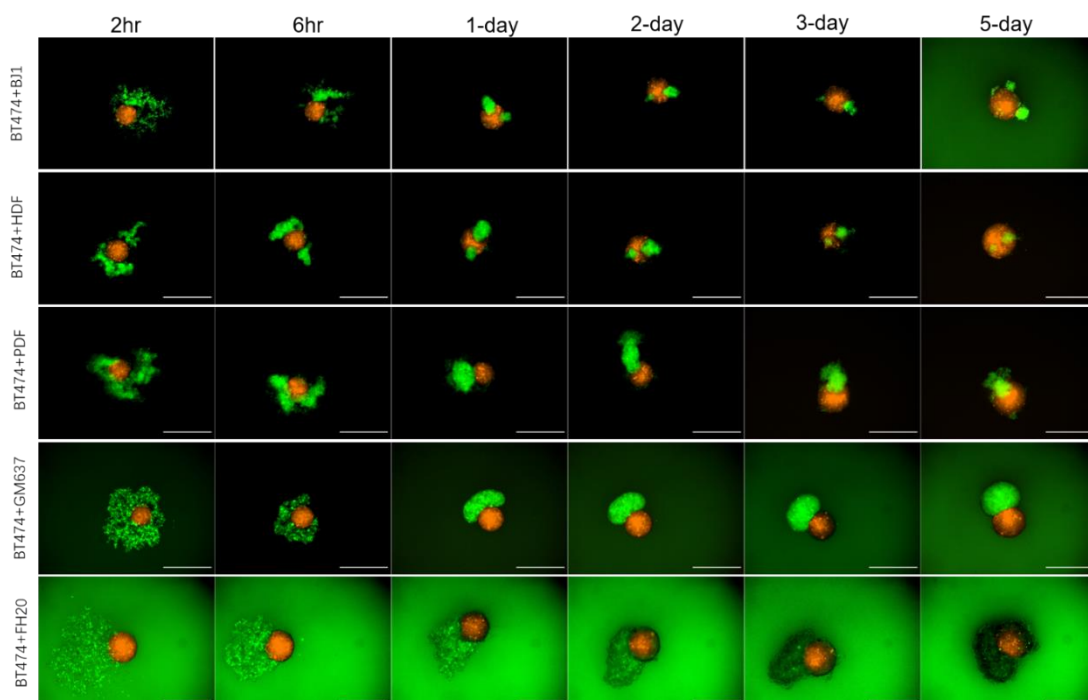
Here the migration of fibroblasts in MCF-7 und BT474 coculture models was investigated. Cell line MCF-7 tagRFP, expressing red fluorescent protein, was generated by stable transfection. MCF-7 tagRFP spheroids were generated by seeding 1000 cells in ULA plates, before adding on day 2 various strains of normal fibroblasts. The fibroblasts were stained with Vybrant™ CFDA SE Cell Tracer 1 day before adding them to the spheroids. Microscopic pictures were taken 2 h, 6 h, 1 day, 2 days, 3 days and 5 days after adding the fibroblasts. In addition to BJ1-hTert and HDF, the behavior of PDF (Human Primary Dermal Fibroblasts), and GM637 and FH20-2 skin fibroblasts was investigated (Figure 4.17). Except for FH20-2, all fibroblast lines form cell clusters on the spheroid surface after 6 h. After 1 day, most of the fibroblasts are found within a dense cluster that appears to be invaginated. At later time points some additional sub-clusters become visible, but there is no dispersion of the main fibroblast cluster, in contradiction to the description by Wenzel et al. (2015). FH20-2 cells, in contrast, appear to remain on the outer surface of the spheroid.



**Figure 4.17:** Migration behavior of BJ1-hTert, HDF, PDF, GM637 and FH20-2 fibroblasts into MCF-7 tagRFP spheroids. Upper panel shows red and green merged images, lower panel shows green channel only. All fibroblasts were stained green with Vybrant<sup>TM</sup> CFDA SE Cell Tracer 24 h before adding to the MCF-7 spheres.

*Fibroblasts were added 2 days after formation of MCF-7 spheres. Images were documented 2 h, 6 h, 1 d, 2 d, 3 d and 5 d after adding fibroblasts using epifluorescence microscopy. Magnification is 2.5x. Scale bar is 500  $\mu$ m.*

Similarly, the behavior of the 5 fibroblast lines was tested together with BT474 spheroids. Since stable transfection of BT474 to generate BT474 tagRFP was not successful, the cells were stained with CellTracker™ Orange CMTMR one day before seeding. As seen in Figure 4.18, clustering of fibroblasts within the first 6 hours appears similar with BT474 spheroids as has been seen with MCF-7 spheroids. However, in contrast to MCF-7 spheroids, the fibroblast clusters appear not to fully invaginate into the BT474 spheroids, except in the case of HDF cells on day 5, where 2 smaller fibroblast clusters have formed. These observations suggest that the apparent invagination of fibroblast clusters is at least in part the result of cancer cells overgrowing the fibroblast clusters rather than purely a migration of the fibroblasts into the spheroid core.



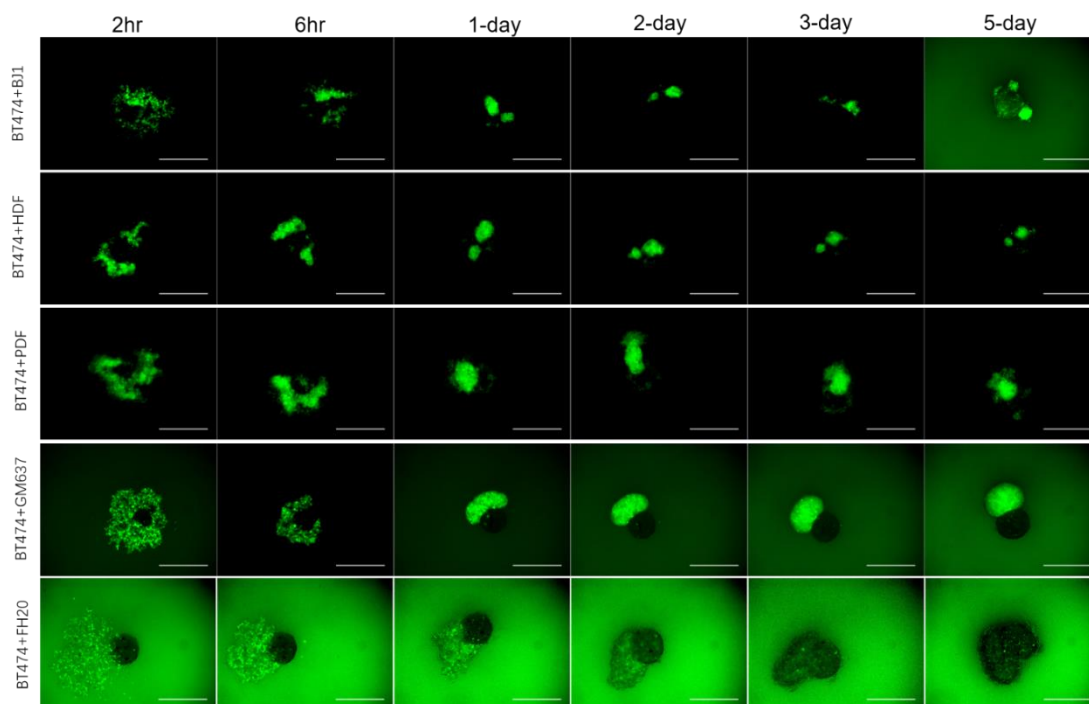


**Figure 4.18:** Migration behavior of BJ1-hTert, HDF, PDF, GM637 and FH20-2 fibroblasts into BT474 spheroids. Upper panel shows red and green merged images, lower panel shows green channel only. All fibroblasts were stained in green with Vybrant™ CFDA SE Cell Tracer and BT474 were stained in red with CellTracker™ Orange CMTMR. Fibroblasts were added 2 days after formation of BT474 spheres. Images were documented 2 h, 6 h, 1 d, 2 d, 3 d and 5 d after adding fibroblasts using epi-fluorescence microscopy. Magnification is 2.5X. Scale bar is 500  $\mu\text{m}$ .

To further elucidate recruitment of BJ1-hTert fibroblasts into MCF-7 spheroids, one coculture spheroid was observed by live-cell imaging over 50 hours. Cell line MCF-7 tagRFP was used and fibroblasts were stained with Vybrant™ CFDA SE Cell Tracer Kit into green color 1 day before adding them to preformed MCF-7 tagRFP spheroids. Immediately after having seeded the green fibroblasts, the plate was placed on the stage of an epifluorescence microscope (Zeiss) with incubation chamber which can provide 5 % CO<sub>2</sub> aeration and a stationary temperature of 37°C. The first image was photographed right after placing the setup, as “0 hour” post co-culture. Then the 3D spheres were imaged every 30 minutes until 100 pictures were captured, which is 50 hours

after seeding in total (for movie see Movie S4.1). Figure 4.19 shows still frames of the time series. Invagination of fibroblast clusters appears complete between 20 and 32 hours after their addition to the cancer cell spheroid. However, it is peculiar that in this approach several fibroblast clusters with comparable sizes formed, whereas normally one large cluster forms. One possible explanation for this behavior could be phototoxic stress or other factors of the imaging set-up. There was no spreading of fibroblasts within the spheroid detectable in the time period observed.

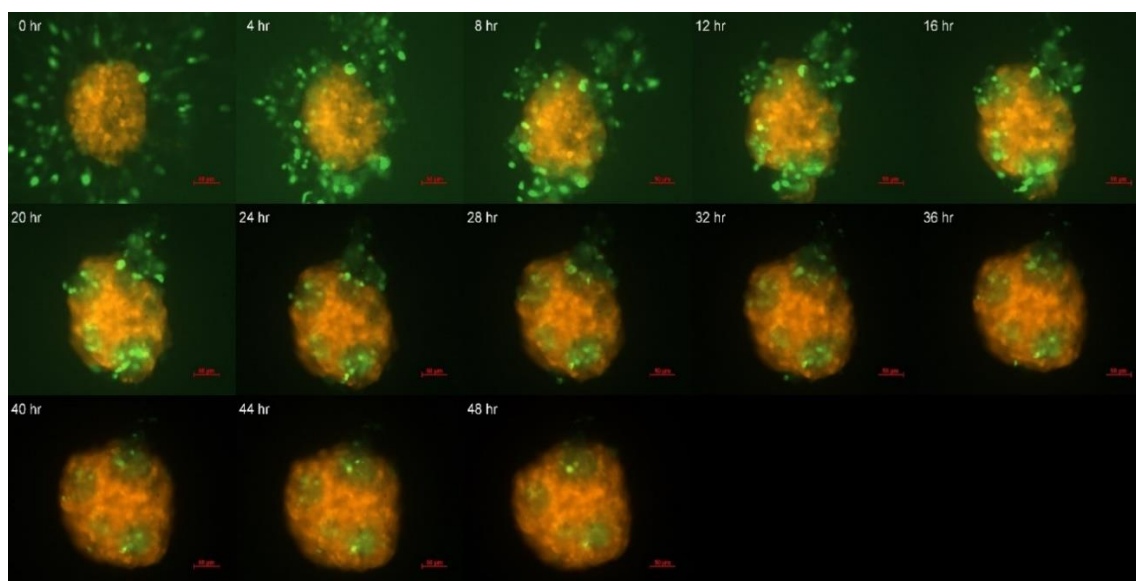
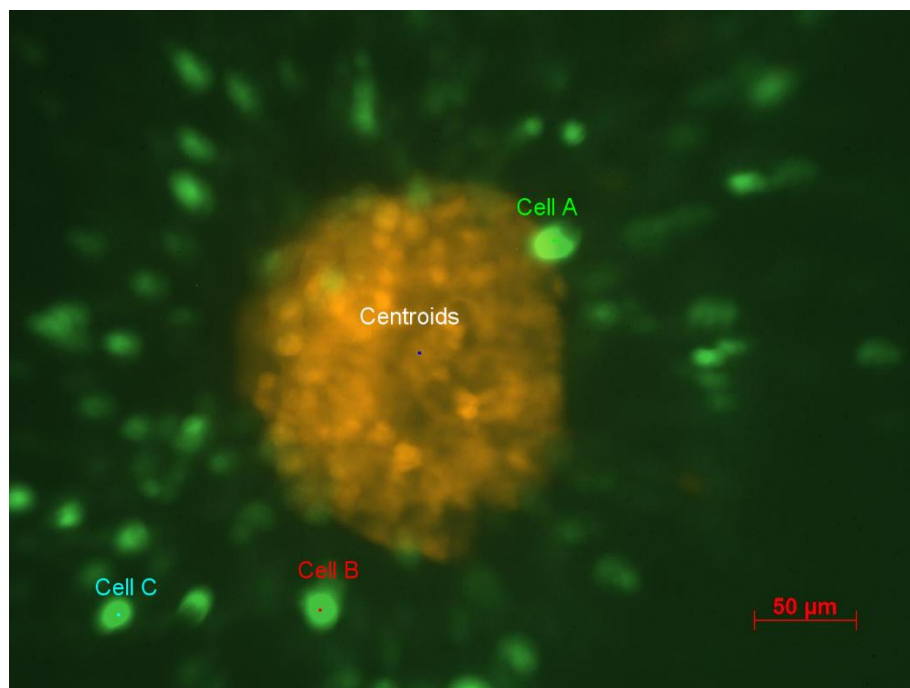


**Figure 4.19:** Snapshots of BJ1-hTert fibroblasts migrating into the MCF-7 tag-RFP spheroids. MCF-7 spheroids were generated 1 day before adding BJ1-hTert. Depicted are images taken every 4 hours until 50 hours. Images were captured by Axio observer Z1 epifluorescence microscope (Zeiss) with 10x objective. Red size bar is 50  $\mu\text{m}$ .

To further characterize if the final localization of fibroblasts is due to the migration of fibroblasts or overgrowing of MCF-7 breast cancer cells, 3 single fibroblasts were tracked manually in the microscopic images over time. The distance to the centroid was calculated in each frame. Figure 4.20 shows the initial position of the 3 fibroblasts and their distance to the centroids as function of frame number, i.e., time. The results suggest that cells first aggregate at the

spheroid and attach to the surface. Thereafter the distance to the centroid further decreases, but only slightly. This suggests that active movement of fibroblasts towards the spheroid center occurs, but that overgrowth by cancer cells plays a more prominent role for the final fibroblast localization.

(A)



(B)

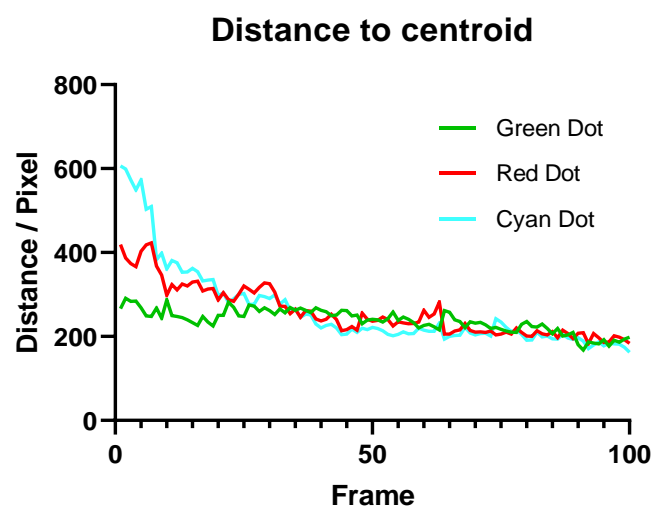


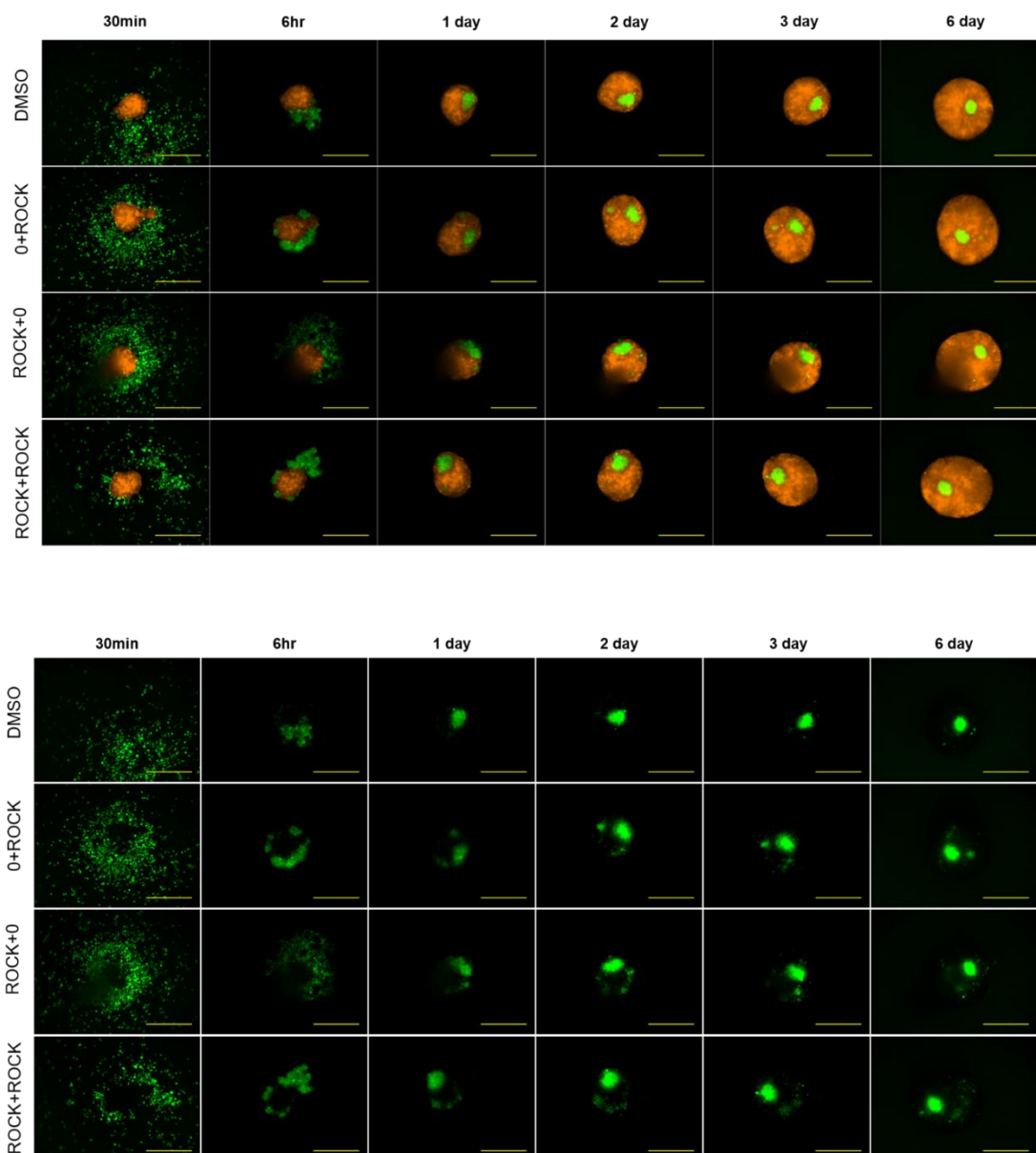
**Figure 4.20:** (A) Initial position of three tracked fibroblasts (B) Plot of distance of

---

*three tracked fibroblasts to the centroid of the spheroid in 100 frames of a movie taken after adding fibroblasts to 1-day old tagRFP MCF-7 spheroids. Images were taken every 30 minutes until 50 hours after seeding. Fibroblasts were tracked manually by the “Tracking” plugin in ImageJ.*

#### **4.4.2 The effects of ROCK-inhibitor on the migration behavior of fibroblasts**

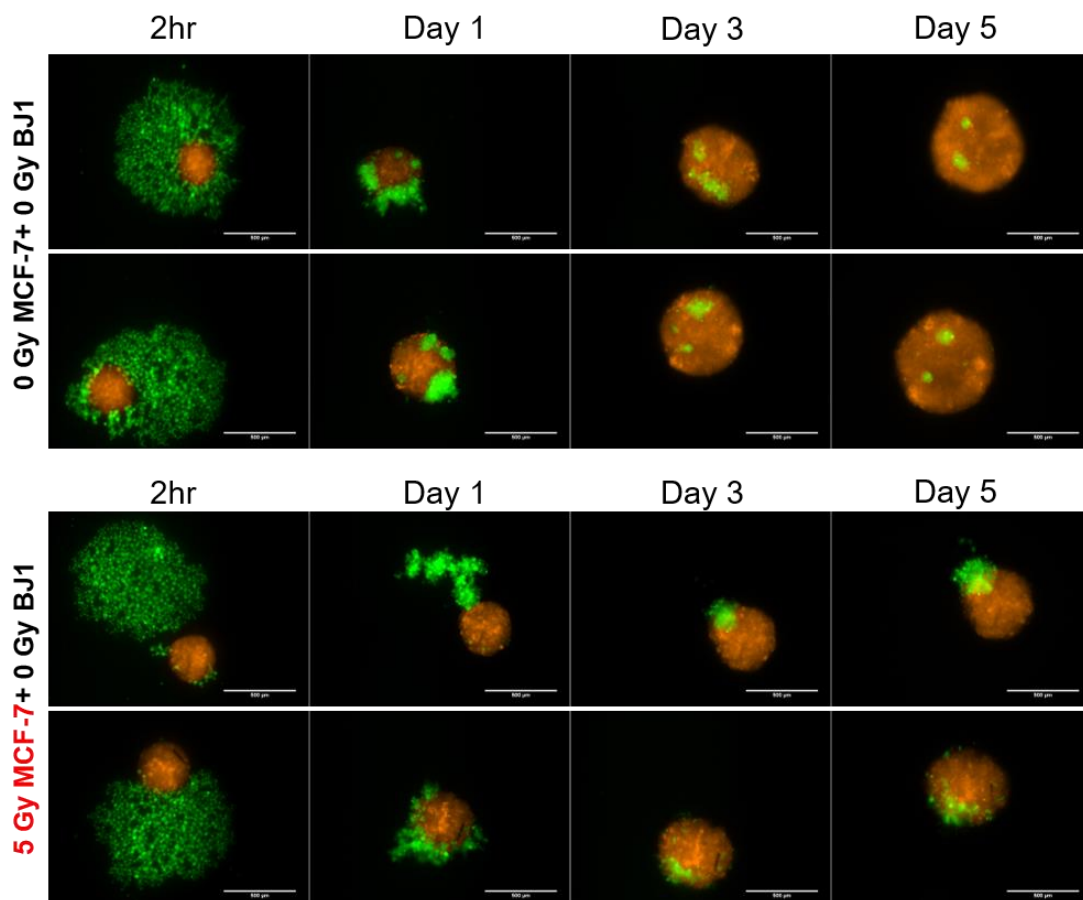
A preferential localization of fibroblast clusters within breast cancer spheroids has been seen by several authors with different types of skin fibroblasts, fetal fibroblasts or mesenchymal stem cells (Fang et al. 2019), (Brechtbuhl et al. 2020), (Ralph et al. 2020), (Pal et al. 2020), (Yakovets et al. 2020), while dispersion of fibroblasts within the spheroid is more rarely seen (Roberts et al. 2016). Wenzel and co-workers (2015) find that fibroblast clustering and invagination are not inhibited by Rho/ROCK inhibitors, while the dispersion step is. Rho-ROCK signaling regulates actomyosin contractility and increases the motility of cancer-associated fibroblasts (Johan and Samuel 2019). To verify that fibroblast clustering on the spheroid surface and apparent invagination are not depending on ROCK signaling, Y-27362, an inhibitor of ROCK1 and ROCK2, was added 30 min after staining to BJ1-hTert cells. After 1 day, the fibroblasts were harvested and added to preformed MCF-7 tagRFP spheroids (sample ROCKi+0). Alternatively, the fibroblasts were not treated with Y-27362 before adding, but after addition of fibroblasts to the spheroids, Y-27362 was added (sample 0+ROCKi). In the third sample, both fibroblasts before adding and the cocultures were treated with ROCK inhibitor (ROCKi+ROCKi). As a solvent control, cells were treated with 0.1 % DMSO. Figure 4.21 shows no effect of treatment with the ROCK inhibitor between day 1 and day 6 after adding of fibroblasts to the cancer cell spheroids. Reproducibly, there was a slight delay in the first hours of fibroblast clustering on the spheroid surface when fibroblasts were pretreated with the inhibitor (sample ROCKi+0). Since this effect was not seen when in addition inhibitor was added to the coculture (sample ROCKi+ROCKi), the biological significance of this observation remains to be elucidated.

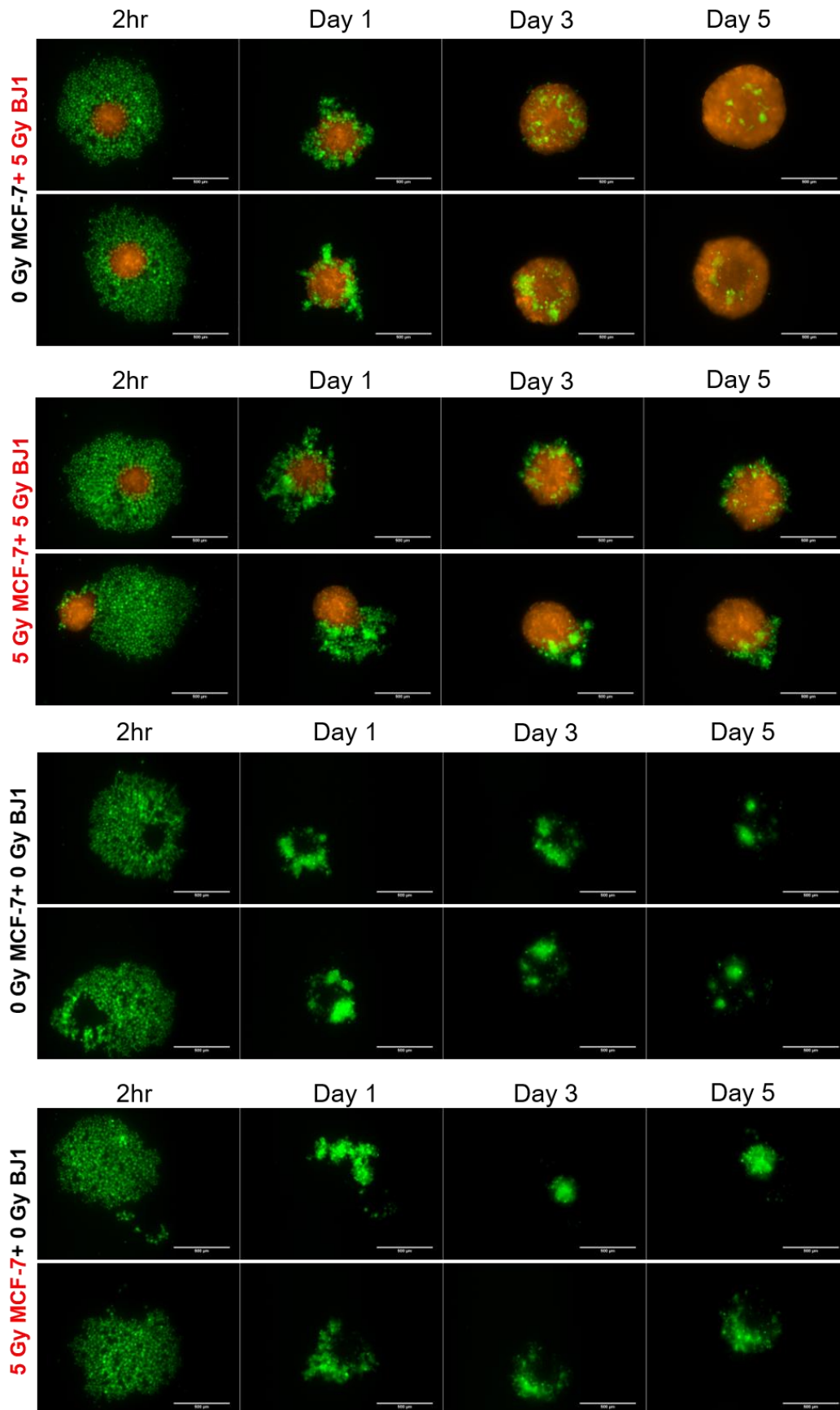


**Figure 4.21:** Effects of ROCK inhibitor Y-27632 on the migration behavior of BJ1-hTert fibroblasts. MCF-7 cells stably expressing tagRFP were seeded to form spheroids in ULA plates. BJ1-hTert fibroblasts were stained in green with Vybrant<sup>TM</sup> CFDA SE Cell Tracer and 24 h later added to 2-day old MCF-7 spheroids. Images were taken 30 min, 6 h, 1 day, 2 days, 3 days and 5 days after adding the fibroblasts using epi-fluorescence microscopy. Magnification is 2.5x. Scale bar is 500  $\mu$ m. The upper panel shows merged images from red and green channels while the lower panel shows the green channel only. Representative pictures from two independent experiments with four samples for each treatment group are shown.

#### 4.4.3 The radiation effects on the migration behavior of fibroblasts

Finally, in a pilot experiment, the effect of irradiation on fibroblast recruitment was investigated. Two-day old MCF-7 tagRFP spheroids and/or Vybrant-stained fibroblasts were irradiated with 5 Gy before adding of the fibroblasts to the spheroids. If fibroblasts are irradiated before adding them to unirradiated cancer cell spheroids, clustering on the spheroids appears to be slightly delayed (Figure 4.22). While invagination occurs on days 3-5, in general the irradiated fibroblasts appear to form more and smaller foci within the coculture spheroid than the unirradiated control fibroblasts. It remains to be tested whether this effect and the generation of multiple fibroblast foci under live-cell imaging (Figure 4.19) have the same mechanistic basis. If spheroids are irradiated before addition of fibroblasts, because of the growth delay apparent invagination is delayed and fibroblast clusters remain on the periphery (Figure 4.22). In the double-treated sample, both effects combine.





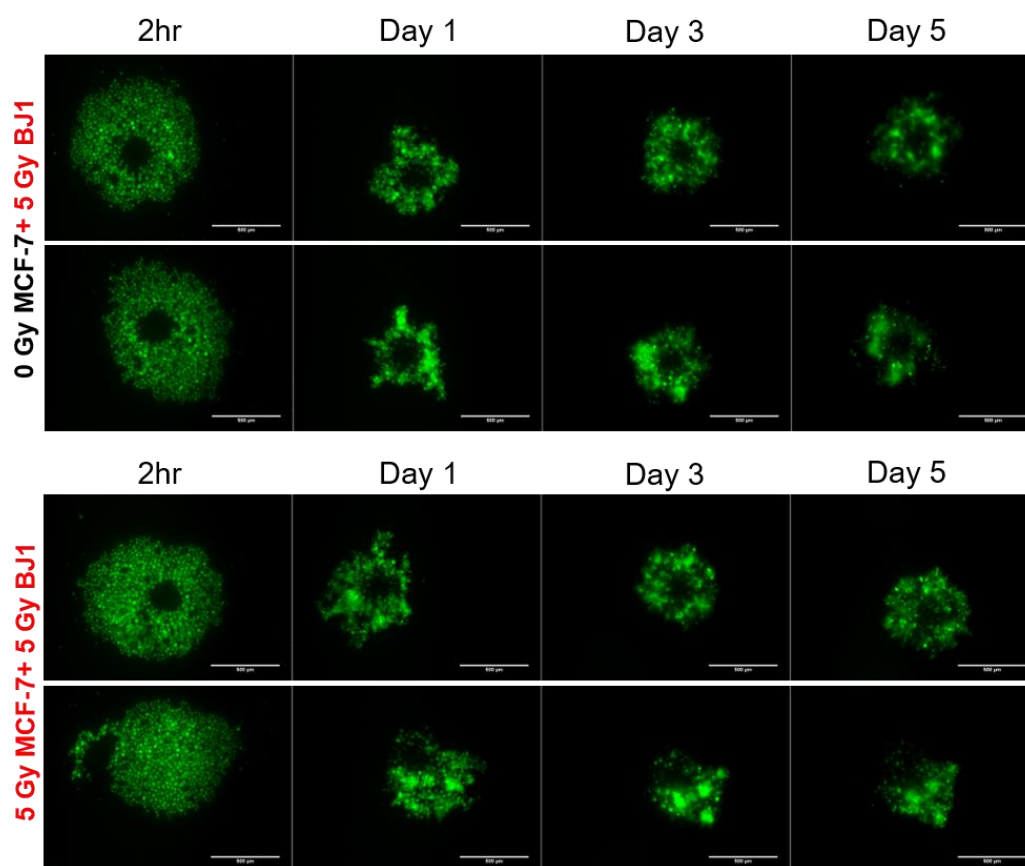


**Figure 4.22:** Radiation effects on the migration behavior of BJ1-hTert fibroblasts. MCF-7 cells stably expressing tagRFP were seeded to form spheroids in ULA plates. BJ1-hTert fibroblasts were stained in green with Vybrant™ CFDA SE Cell Tracer and 24 h later added to 2-day old MCF-7 spheroids. Either fibroblasts alone, cancer cell spheroids alone, or both cell compartments were irradiated with X-rays at a dose of 5 Gy before adding the fibroblasts. Images were taken 30 min, 6 h, 1 day, 2 days, 3 days and 5 days after adding the fibroblasts using epi-fluorescence microscopy. The upper panel shows merged images from red and green channels while the lower panel shows the green channel only. Magnification is 2.5x. Scale bar is 500 µm. Shown are each two representative spheroids taken from 1 experiment with 4 samples for each treatment group.

#### Conclusion of Chapter 4.4

Fibroblasts added to preformed MCF-7 or BT474 spheroids first cluster on the spheroid surface and then are invaginated to result in one or a few fibroblast clusters in the coculture spheroid. Overgrowth by cancer cells contributes to the

invagination process. Pre-treatment of BJ1-hTert fibroblasts with ROCK inhibitor has a small and transient effect on the clustering stage. Irradiation of BJ1-hTert fibroblasts before seeding may have a longer-lasting effect on clustering and lead to more dispersed fibroblast localization within the coculture spheroid. Possibly, phototoxicity results in similar effects, but further experiments will be needed for clarification.

#### **4.5 Fibroblast-mediated invasion of mammary carcinoma cells**

In chapter 4.1 it was shown that mammary carcinoma cell lines MCF-7 and BT474 are unable to invade into invasion matrix after embedding of cancer cell spheroids. Thus, it was hypothesized that these cell lines should be suitable for the development of a model for fibroblast-mediated cancer cell invasion. Since the main interest of the present work is opportunistic invasion, which relies on mesenchymal cells forming tracks in the matrix that allow cancer cells to follow, cocultures were set up with normal fibroblast strains BJ1-hTert and HDF rather than CAFs.

##### **4.5.1 Low- and high-resolution imaging of fibroblast-led invasion model**

Both, BJ1-hTert and HDF fibroblasts show invasiveness after embedding as fibroblast monoculture spheroids in Spheroid Invasion Matrix (Figure 4.23 A). HDF cells apparently migrate longer distances than BJ1-hTert cells in the same time period. Star-like track patterns suggest that often fibroblasts tend to follow in tracks formed by leader cells rather than producing their own track. Similar patterns are observed after embedding of coculture spheroids (Figure 4.23 A). All four combinations (MCF-7 + BJ1-hTert, MCF-7 + HDF, BT474 + BJ1-hTert, BT474 + HDF) resulted in invasion.

To elucidate if cancer cells can also follow in fibroblast tracks, MCF-7 and BT474 cancer cells were stained red by CellTracker™ Orange CMTMR Dye and BJ1-hTert and HDF fibroblasts were stained green with Vybrant™ CFDA

SE Cell Tracer Kit. Stained cells were cocultured in ULA plates for one day and then embedded in the invasion matrix. Again, all 4 combinations were tested. Confocal microscopy on day 5 after embedding shows that in coculture spheroids the presence of fibroblasts enables MCF-7 and BT474 cells to invade into the matrix (Figure 4.23 B). In general, in these structures the distance of the cancer cells to the solid spheroids is lower than the fibroblast distance, and in individual tracks it is evident that chains or clusters of cancer cells directly follow a fibroblast when invading into the matrix.

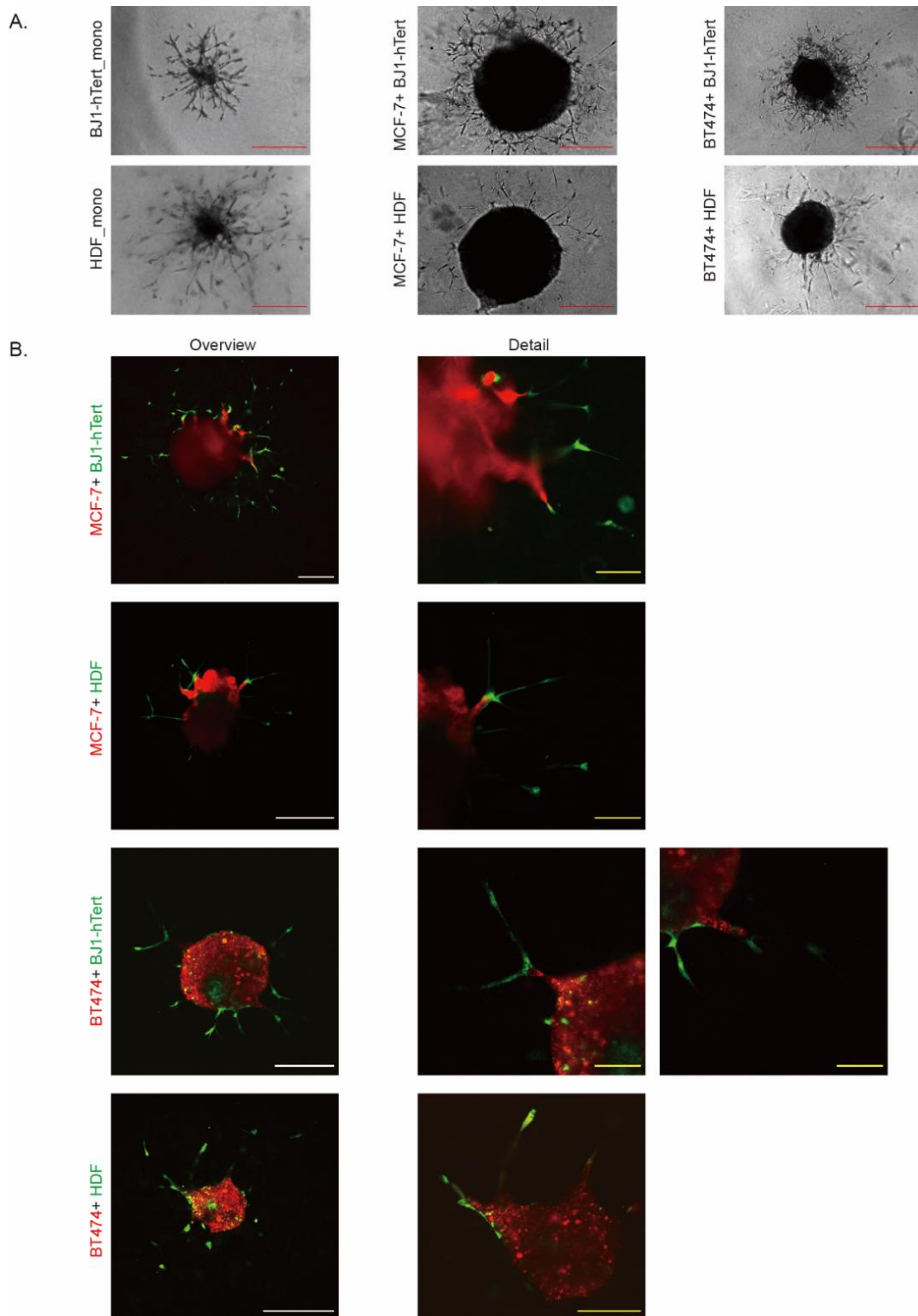


**Figure 4.23:** Fibroblast-led invasion of breast cancer cells into Spheroid Invasion Matrix. A. Monocultured BJ1-hTert and HDF fibroblast spheroids and coculture spheroids with mammary carcinoma cells MCF-7 and BT474, respectively, were embedded in matrix one day after seeding. Bright field images were taken on day 7 after embedding. Size bar is 500  $\mu$ m. B. Cancer cells stained red by expression of

*tagRFP (MCF-7) or by live-cell staining (BT474) were seeded with green fibroblasts obtained by live-cell staining in ULA plates. Spheroids were embedded in matrix one day after seeding and confocal images were taken on day 5 after embedding.*

*Overviews and close-ups of fibroblast-led collective cancer cell migration are shown for all coculture combinations. White size bar is 500  $\mu\text{m}$  and yellow bar is 200  $\mu\text{m}$ .*

## **Conclusion of chapter 4.5**

High-resolution imaging demonstrates that epithelial-like cancer cells together with normal fibroblasts can serve as a model for fibroblast-led collective invasion that is easy to set up and flexible. In the following, this model is used to study the effect of irradiation.

## **4.6 Radiation effects on fibroblast-led invasion**

### **4.6.1 Radiation effects on the number of invading cells**

To investigate the effect of irradiation on fibroblast-led invasion, BJ1-hTert and HDF fibroblast monoculture spheroids and coculture spheroids consisting of MCF-7 + BJ1-hTert or BT474 + HDF were irradiated with 5 Gy or mock-treated one day after adding the fibroblasts. Then they were embedded in matrix and invasion was observed by brightfield microscopy over 14 days (Figure 4.24). The visual impression suggested that fewer cells were able to invade the matrix after irradiation in the case of BJ1-hTert-containing spheroids, but not in the case of HDF-containing spheroids. Therefore, in a first analysis, in the microscopic image the area occupied by cells beyond the limits of the solid spheroid cores was determined by segmentation-based image analysis. Assuming that the size of cells remains largely constant, the area occupied by invading cells serves as a measure for the number of invading cells. After irradiation with 5 Gy, invaded area originating from BJ1-hTert fibroblast monoculture spheroids or MCF-7 + BJ1-hTert coculture spheroids was reduced to about half (Figure 4.25), suggesting that part of the cells lost their ability to

migrate. In contrast, no radiation effect on the number of invading cells originating from HDF fibroblast monoculture spheroids or BT474 + HDF coculture spheroids was seen (Figure 4.25).

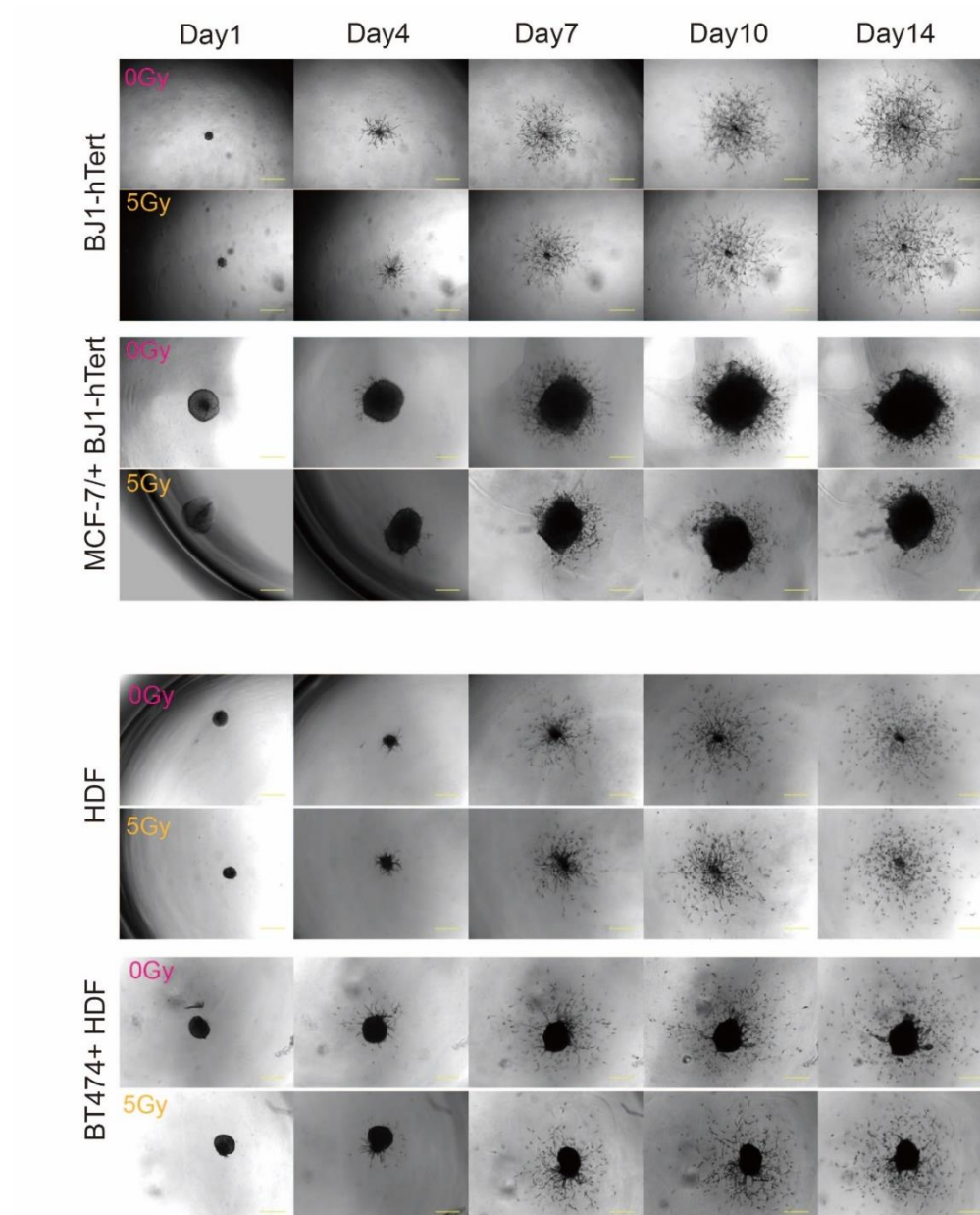


**Figure 4.24:** Radiation effects on invasion in fibroblast monoculture and cancer cell + fibroblast coculture. 1000 cancer cells per well were seeded in ULA plates 1 day before addition of 1000 fibroblasts. Spheroids were irradiated with 5 Gy or mock-treated 1 day after addition of fibroblasts and embedded in matrix after 30 min recovery incubation at 37° C. Invasion was recorded up to day 14. Size bars are 200  $\mu\text{m}$ .

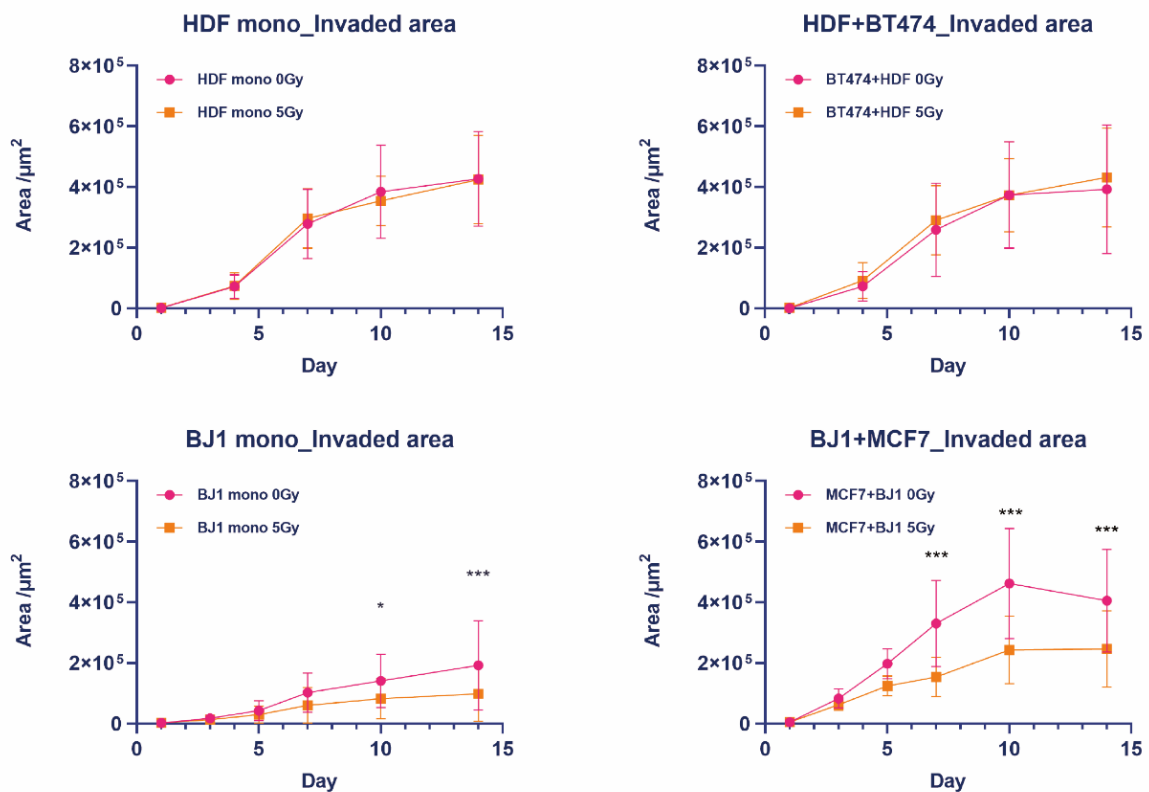


**Figure 4.25:** Invasion behavior after irradiation - area occupied by invading cells. The area occupied by invading cells surrounding the solid spheroidal core was measured by image analysis and plotted as function of invasion day. Indicated are means  $\pm$  SD from 5 independent experiments with each 6-8 replicates. Sidak's test following two-way ANOVA was used to detect significant differences between the means of 3 or more independent groups. A  $p$  value  $\leq 0.05$  was considered statistically significant. Single, double and triple asterisks indicate significant differences with  $p$ -values of  $<0.05$ ,  $<0.01$  and  $<0.001$ , respectively.

#### 4.6.2. Radiation effects on invasion distance

Radiation may not only have an effect on the binary ability of cells to invade or not, but also on invasion velocity. Therefore, the effect of irradiation on the invasion radius travelled by invading cells was investigated. In collaboration with Dr. Christian Siebenwirth, Institut für Radiobiologie der Bundeswehr, I developed a method for estimation of maximum invasion distances from

microscopic images. A potential pitfall when measuring the distance of individual invading cells to the spheroid is that some cells may already have left the camera field. I therefore determined the yield of pixels occupied by invaded cells as a function of radius from the centroid after polar transformation. By regression analysis then the x-intercept of the curve, i.e., the maximum radius migrated, was estimated. Figure 3.3 depicts the steps of the evaluation.

The maximum invasion radius from the centroid,  $r_{max\_invasion}$ , in pixels are shown in Figure 4.26 and Table 4.2. Analysis was performed on images taken on day 7 and on day 14 after embedding. In unirradiated controls, the maximum invasion radii (mean  $\pm$  SD) are higher for HDF (410  $\pm$  100 pixels) than BJ1-hTert cells (200  $\pm$  50 pixels) on day 7. In the second week of observation, the maximum invasion radii increase by another 50 % in HDF and about 100 % in BJ1-hTert. In HDF monoculture and BT474 + HDF coculture samples maximum invasion radii are comparable. In contrast, in MCF-7 + BJ1-hTert coculture samples (470  $\pm$  60 pixels) larger maximum invasion radii are seen on day 7 than in BJ1-hTert monoculture (200  $\pm$  50 pixels). This presumably reflects the differences in size of the solid spheroid core. The differences between mono- and coculture decrease in the second week.

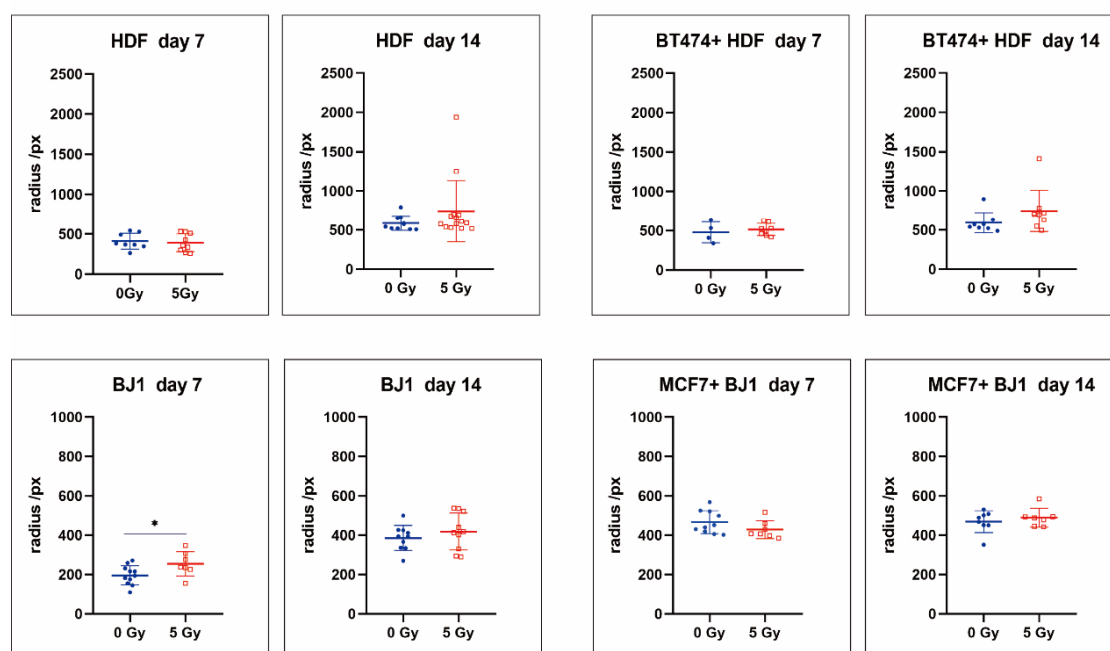


**Figure 4.26:** Invasion behavior after irradiation - Maximum invasion radius. Maximum

*invasion radius was measured from spheroid centroid on days 7 and 14 after irradiation with 5 Gy or mock-treatment and embedding. Data from 7-12 spheroids per data point (except for BT474 + HDF, day 7: 4 spheroids) are shown as swarm plot, together with mean and SD. Unpaired, two-tailed Students' t-test was performed with Graphpad Prism8. A p value  $\leq 0.05$  was considered statistically significant. Single asterisk indicates significant difference with p-value of  $<0.05$ .*

Irradiation with 5 Gy had no significant effect on maximum invasion radius in HDF monoculture or BT474 + HDF spheroids. In BJ1-hTert monoculture, irradiation resulted in a small, but statistically significant increase in maximum invasion radius on day 7 ( $200 \pm 50$  pixels at 0 Gy vs  $255 \pm 70$  pixels at 5 Gy). This increase was, however, not anymore apparent on day 14. In MCF-7 + BJ1-hTert cocultures radiation did not significantly affect maximum invasion radius.

For further clarification, the minimum differences in  $r_{max\_invasion}$  between irradiated and unirradiated samples that can be excluded at  $\alpha < 0.05$  were estimated. Considering the variances and sample sizes of the distributions for BJ1-hTert monocultures on day 14, a difference in  $r_{max\_invasion}$  of more than 20 % can be excluded, while the respective value for cocultures is 12 %.

<b>sample</b>	<b>HDF mono d7, 0 Gy n=8</b>	<b>HDF mono d7, 5 Gy n=9</b>	<b>HDF + BT474 d7, 0 Gy n=4</b>	<b>HDF + BT474 d7, 5 Gy n=8</b>
$r_{max\_invasion} / \text{px}$	$410 \pm 100$	$390 \pm 120$	$480 \pm 140$	$510 \pm 80$
$r_{core} / \text{px}$	$63 \pm 9$	$58 \pm 7$	$119 \pm 7$	$122 \pm 8$
<b>sample</b>	<b>HDF mono d14, 0 Gy n=10</b>	<b>HDF mono d14, 5 Gy n=14</b>	<b>HDF + BT474 d14, 0 Gy n=8</b>	<b>HDF + BT474 d14, 5 Gy n=9</b>
$r_{max\_invasion} / \text{px}$	$590 \pm 100$	$700 \pm 400$	$590 \pm 130$	$750 \pm 270$
$r_{core} / \text{px}$	$51 \pm 11$	$51 \pm 11$	$140 \pm 26$	$122 \pm 6$

<b>sample</b>	<b>BJ1 mono d7, 0 Gy n=11</b>	<b>BJ1 mono d7, 5 Gy n=7</b>	<b>BJ1 + MCF-7 d7, 0 Gy n=10</b>	<b>BJ1 + MCF-7 d7, 5 Gy n=7</b>
$r_{max\_invasion} / \mu\text{m}$	200 ± 50	255 ± 70	470 ± 60	430 ± 50
$r_{core} / \mu\text{m}$	41 ± 8	40 ± 13	220 ± 18	171 ± 17
<b>sample</b>	<b>BJ1 mono d14, 0 Gy n=10</b>	<b>BJ1 mono d14, 5 Gy n=10</b>	<b>BJ1 + MCF-7 d14, 0 Gy n=8</b>	<b>BJ1 + MCF-7 d14, 5 Gy n=7</b>
$r_{max\_invasion} / \mu\text{m}$	390 ± 70	410 ± 100	470 ± 60	490 ± 50
$r_{core} / \mu\text{m}$	36 ± 5	37 ± 10	264 ± 20	203 ± 14

**Table 4.2:** Maximum invasion radius and core radius measured from spheroid centroid on days 7 and 14 after irradiation with 5 Gy or mock-treatment followed by embedding. Data from  $n$  spheroids per data point were obtained in 3 independent experiments. Mean and SD are given after rounding according to JCGM 100 (2008).

#### 4.6.3 Sensitivity to DSB induction by NCS treatment in BJ1-hTert and HDF fibroblasts

The observed difference in number of invading cells between BJ1-hTert containing spheroids and those containing HDF could reflect different sensitivity of BJ1-hTert and HDF cells towards radiation-induced cell death. The gold standard for determining radiosensitivity is the colony-formation assay where single adherent cells are seeded and allowed to form colonies with > 50 cells upon incubation for 10-20 days, depending on growth rate. Since BJ1-hTert cells did not form colonies but rather spread over the whole dish surface, growth curves were analyzed rather than colony formation. Since, due to the pandemic situation, irradiation experiments were not possible at this stage, the sensitivity of BJ1-hTert and HDF cells to the radiomimetic drug neocarzinostatin (NCS) was determined. NCS is an enediyne antibiotics which produces DSB due to

radical attack (Povirk 1996).

In preliminary experiments, 2D cultured fibroblasts were treated with different concentrations of NCS (1:500, 1:1000 and 1:2000 dilution) for 60 min and then incubated for 8 days, then cells were harvested and counted. Since the 1:1000 and 1:2000 dilutions had only little effect, further experiments were carried out with 1:500 diluted NCS (equivalent to 1  $\mu$ g/mL). Previous work in the lab with a variety of different cell lines suggests that this concentration induces a number of DSB foci comparable to those seen after 5 Gy irradiation.

As expected, NCS treatment had an inhibitory effect on the proliferation in both fibroblast strains. Compared to the solvent control, only 41.5 %  $\pm$  9.3 % of BJ1-hTert cells and 36.0 %  $\pm$  6.0 % of HDF cells were obtained. This difference is not significant, indicating that these two cell lines have comparable sensitivity to the damage induced by NCS (Table 4.3 and Figure 4.27). These results suggest that the reduced number of invading BJ1-hTert cells may not simply be a result of cell death, but of active modulation of the decision to invade and that this modulation differs in BJ1-hTert and HDF cells. It cannot be excluded at the present stage, however, that the reactions towards radiation and NCS differ.

	DMSO control			NCS (1:500)		
	Mean %	SD %	N	Mean %	SD %	N
<b>BJ1-hTert</b>	100	0	3	41.5	9.3	3
<b>HDF</b>	100	0	4	36.0	5.9	4

**Table 4.3:** Sensitivity of BJ1-hTert and HDF fibroblasts towards treatment with the radiomimetic. Data are from 3 (BJ1-hTert) or 4 (HDF) independent experiments.

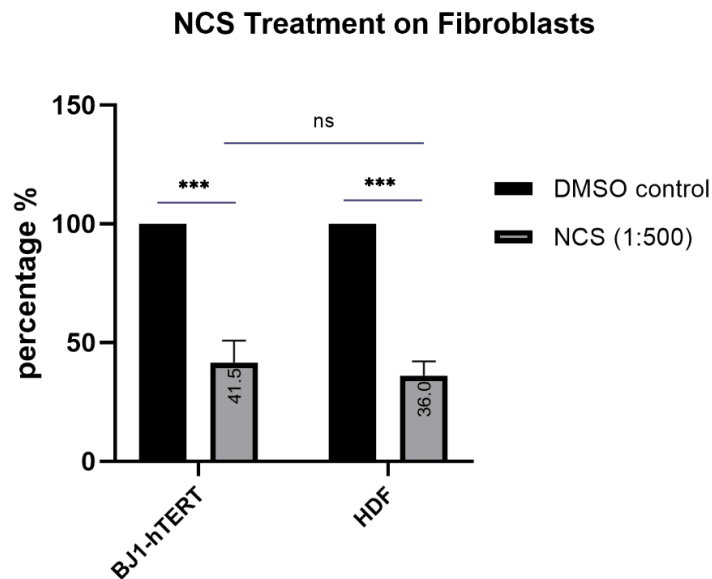


**Figure 4.27:** Inhibition of fibroblast proliferation by radiomimetic treatment. One day after 2D seeding, BJ1-hTert and HDF fibroblasts were treated with NCS (1:500 dilution, 60 min) and then incubated for 8 days. Sidak's test following two-way ANOVA was used to detect significant differences between the means of 4 (HDF) or 3 (BJ1-hTert) independent groups. A  $p$  value  $\leq 0.05$  was considered statistically significant. Triple asterisks indicate  $p$  values  $< 0.001$ , ns indicates non-significant differences.

### Conclusion of Chapter 4.6

To sum up, radiation effects on number of invading cells and invasion distance can be uncoupled by the presented method. No major promoting effect of irradiation on fibroblast-mediated invasion could be detected.

#### 4.7 Investigation of invasion and radiation effects with non-linear optical methods – proof of concept studies

3D tissue culture models are an important improvement compared to 2D cultures, but in the end complex reactions such as invasion should be investigated *in vivo*. Invasion processes are energy-demanding and it has been reported that invasiveness is associated with metabolic alterations, including altered distribution of mitochondria in cancer cells (Cunniff et al. 2016, Commander et al. 2020, Nagai et al. 2020, Mosier et al. 2021). A high-resolution, label-free method for non-invasive investigation of metabolic processes and alterations in invasiveness is needed for *in vivo* and complex 3D *in vitro* studies. Based on autofluorescence of NAD(P)H and FAD, two-photon excited fluorescence (TPEF) microscopy allows determining an optical redox ratio (ORR), defined as the TPEF intensity of FAD/ [NAD(P)H+FAD] (Varone et al. 2014). Furthermore, fluorescence lifetime imaging (FLIM) of NAD(P)H can be used as a metabolic indicator, since fluorescence lifetime in the protein-bound state (e.g., in mitochondria) is longer than in the free state (e.g., in the cytoplasm). Hypoxia and glucose starvation elicit opposite changes, with reduced ORR and reduced relative levels of bound NAD(P)H under hypoxia, and increased ORR with relatively increased bound NAD(P)H after glucose starvation. Interestingly, mitochondrial clustering, which can also be detected via analysis of NAD(P)H TPEF images, yields additional information: strong perinuclear clustering of mitochondria increases when glycolytic metabolism increases and mitochondria have a more fragmented organization, while an increase in mitochondrial fused networks associated with increased oxidative phosphorylation results in lower perinuclear clustering (Liu et al. 2018). FAD fluorescence lifetime alterations are less well characterized than NAD(P)H fluorescence lifetime alterations. Free FAD, which has longer lifetimes than protein-bound FAD, has been associated by some authors with oxidative phosphorylation, but its association with glycolytic metabolism has also been proposed (Kalinina et al. 2021).

In several proof-of-principle experiments, which were performed in the lab of Prof. J. Popp, Jena, it was investigated if breast cancer cells and fibroblasts differ in TPEF and NAD(P)H or FAD fluorescence lifetime in a 3D coculture invasion model of MCF-7 and BJ1-hTert. In addition, in 2D cultures of these cell lines, it was investigated if radiation effects are detectable with these methods. Unfortunately, in the course of this thesis it was not possible to perform several complete sets of experiments, therefore the data presented in the following have preliminary character.

#### **4.7.1 Investigation of the collective invasion model by FLIM**

First the fibroblast-led invasion model of embedded MCF-7 and BJ1-hTert cells was investigated by fluorescence lifetime microscopy with two-photon excitation coupled with 458/64 nm emission filter for NAD(P)H and 525/30 nm emission filter for FAD signal. The decay components were separated by double-exponential decay analysis by SPCImage software. For each molecule, NAD(P)H or FAD, the short-lifetime component (free NAD(P)H, bound FAD) or long-lifetime component (bound NAD(P)H or free FAD) was estimated. The images were color-coded according to the mean lifetime of the components.

Images were taken at two protrusion positions where elongated presumed fibroblasts at the leading edge of the protrusions are followed by stockier presumed cancer cells. The results (Figure 4.28) show that in the NAD(P)H channel, there is little difference in mean fluorescence lifetimes between elongated leader cells and stocky followers, apart from the intracellular distribution of the signal, which is compatible with a lower perinuclear mitochondrial clustering in fibroblasts (see arrow in Figure 4.28) compared to cancer cells (see also chapter 4.7.2). In contrast, the mean fluorescence lifetime of FAD differs largely in these two kinds of cells. Unfortunately, whether OXPHOS is associated with increased or decreased levels of bound FAD is still a matter of debate (Kalinina et al. 2021) and inference of metabolic status by FAD fluorescence lifetime is further complicated by influence of pH and contributions of FMN. The elongated leading cells show a rather long mean

FAD fluorescence lifetime (blue), suggesting a higher ratio of free vs. bound FAD in the cells. The homogeneous signal distribution in the cell may be explained by the fact that FAD synthesis is not only found in cytosol, but in cell nuclei (Giancaspero et al. 2013). The bulk of the stocky cells have a much shorter mean FAD fluorescence lifetime (greenish color). Interestingly, the first few cancer cells immediately following the fibroblasts exhibit very short mean fluorescence lifetime (orange in Figure 4.28). While the biological significance of this observation is not yet clear, it may indicate that distinct metabolic changes occur at the junction of mammary carcinoma cells and fibroblasts. In this context, it is interesting that enhanced glycolysis and lactate production have been associated with activation of matrix-metalloproteinases (Romero-Garcia et al. 2016), which have been shown to trigger and enhance the invasion of cancer cells (Björklund and Koivunen 2005).

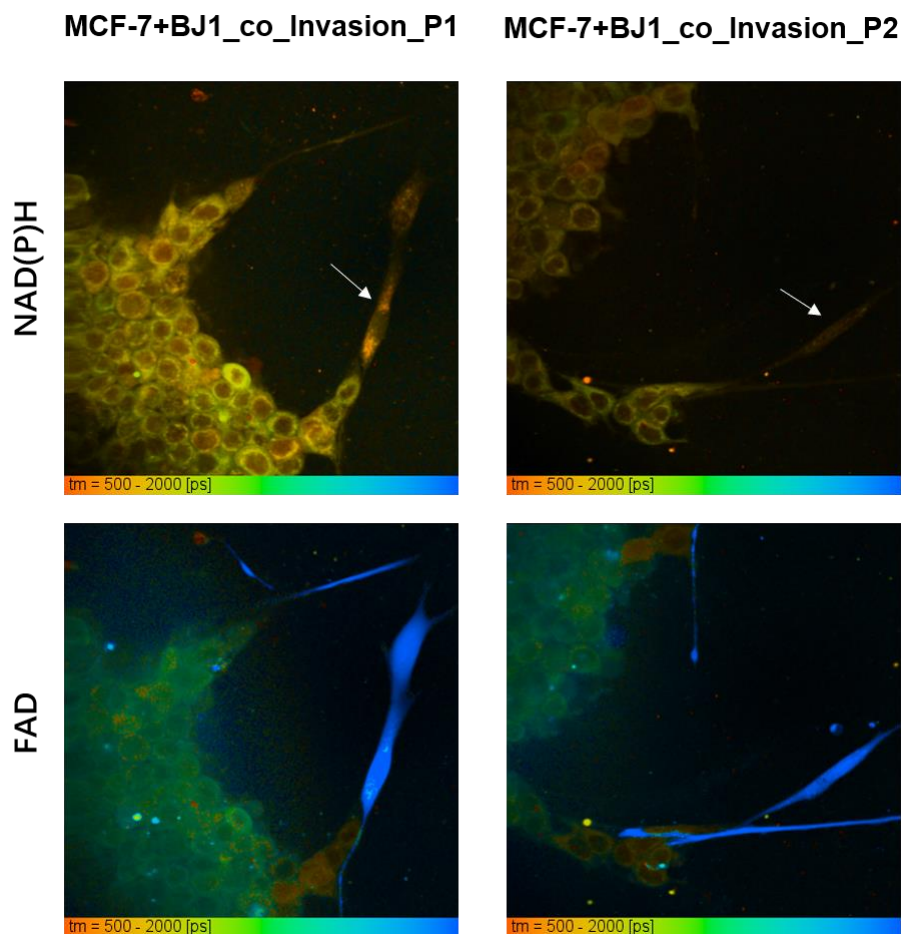


**Figure 4.28:** MCF-7 + BJ1-hTert collective invasion model observed by fluorescent

*life-time imaging microscopy. 3D coculture collective invasion models were excited with 672 nm light (TPEF), and fluorescence emission was collected with two-photon FLIM detector coupled with 458/464 nm (NAD(P)H) and 525/530 nm (FAD) emission filters. Two different sites of invasion protrusions (P1 and P2) were imaged. Magnification is 40x.*

#### **4.7.2 Radiation effects on NAD(P)H and FAD fluorescence lifetime**

For a preliminary assessment if radiation induces metabolic alterations that can be detected by alterations in NAD(P)H or FAD fluorescence lifetimes, 2D monocultures of MCF-7 cells were irradiated with 15 Gy and then incubated for different periods of time before fixation with 4 % PFA. The decay components were separated by double-exponential decay analysis by SPCImage software. For each molecule, NAD(P)H or FAD, the short-lifetime component (free NAD(P)H, bound FAD) or long-lifetime component (bound NAD(P)H or free FAD) was estimated. The images were color-coded according to the mean lifetime of the components.

First the radiation influence on the mean NAD(P)H lifetime was assessed. Figure 4.29 shows that even in the unirradiated control (left panels) there is some variation of mean lifetime  $\tau_m$  over time, which presumably reflects the influence of cell density and cell cycle distribution (Chacko and Eliceiri 2019). Still, the mean lifetime in all samples is found roughly in the range of 1100 – 2000 ps. In contrast, the irradiated cells appear to show longer mean fluorescence lifetime after 2 h which may be indicative of a shift towards energy production by oxidative phosphorylation, followed by a much shorter mean lifetime after 24 h (Figure 4.29, right panels and Figure S4.1). In contrast, there was little variation on FAD lifetime over time and little difference between irradiated samples and controls (Figure 4.30).

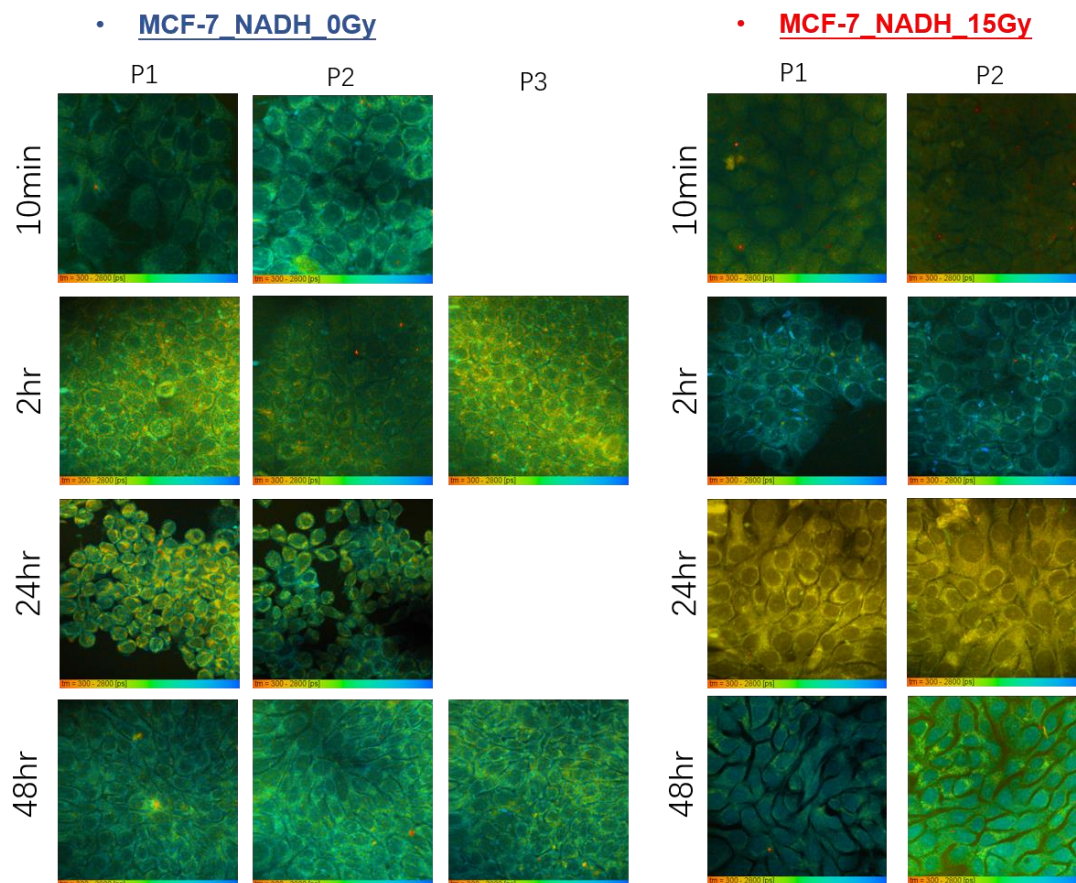


**Figure 4.29:** Detection of NAD(P)H lifetime in 2D-cultured MCF-7 cells fixed 10 min, 2 h, 24 h and 48 h after 15 Gy X-ray irradiation or mock-treatment. MCF-7 cells were excited with 672 nm light (TPEF), and fluorescence emission was collected with two-photon FLIM detector coupled with 458/464 nm (NAD(P)H) emission filters. For each time point two or three regions were investigated. The magnification is 40x.

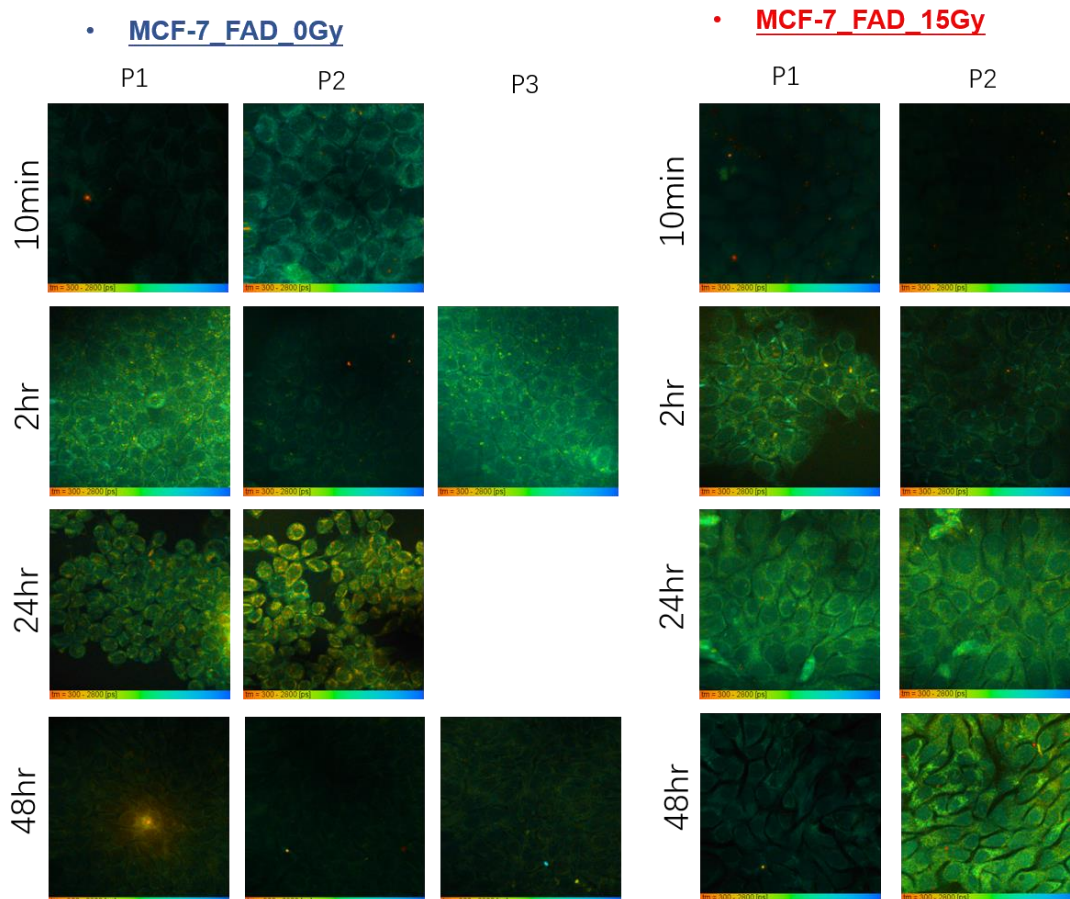


**Figure 4.30:** Detection of FAD life-time in the 2D-cultured, fixed MCF-7 cells 10 min, 2 h, 24 h and 48 h after 15 Gy X-ray irradiation or mock-treatment. MCF-7 cells were excited with 672 nm light (TPEF), and fluorescence emission was collected with two-photon detector FLIM coupled with 525/530 nm (FAD) emission filters. For each time point two or three regions were investigated. For each time point or two or three regions were investigated. The magnification is 40x.

NAD(P)H and FAD fluorescence lifetimes were also investigated in BJ1-hTert cells (Figures S4.2, 4.31 and 4.32). The distribution of mitochondria exhibits a lower degree of perinuclear clustering than is seen in the cancer cells and mitochondrial structures appear larger, which is compatible with energy production depending more on oxidative phosphorylation than in the cancer cells (Figure 4.31). An overall bluish pseudo-coloring, signifying rather long mean NAD(P)H fluorescence lifetimes, is also compatible with increased oxidative phosphorylation. However, individual cells exhibit yellowish pseudo-

coloring indicative of more free-NAD(P)H and thus suggesting glycolytic energy production, and over time yellowish coloring takes over in all cells. Little difference was, however, seen between irradiated and unirradiated cells. FAD fluorescence lifetime measurements also did not yield indications for large differences between unirradiated and irradiated BJ1-hTert cells, and overall variation was smaller than seen for NAD(P)H fluorescence lifetime (Figure 4.32).

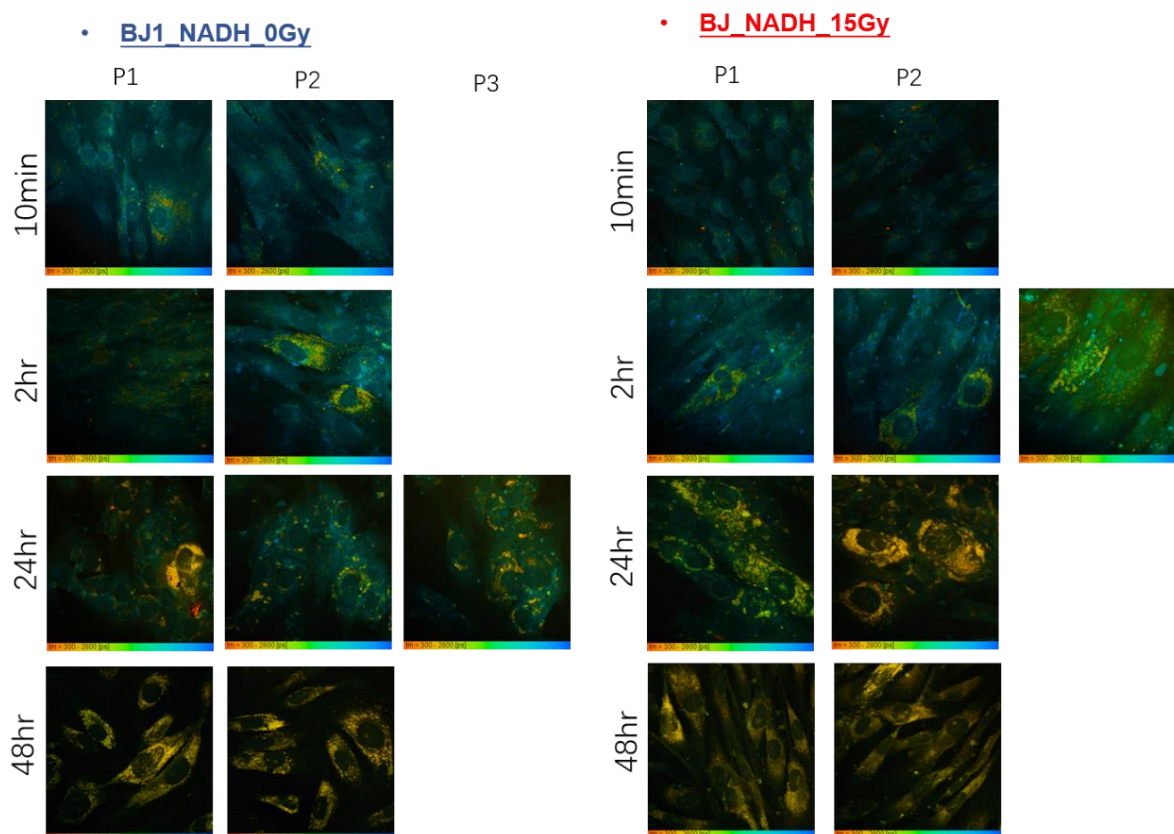


**Figure 4.31:** Detection of NAD(P)H lifetime in 2D-cultured, fixed BJ1-hTert cells 10 min, 2 h, 24 h and 48 h after 15 Gy X-ray irradiation or mock-treatment. BJ1-hTert cells were excited with 672 nm light (TPEF), and fluorescence emission was collected with two-photon FLIM detector with 458/464 nm (NAD(P)H) emission filters. For each time point two or three regions were investigated. The magnification is 40x.

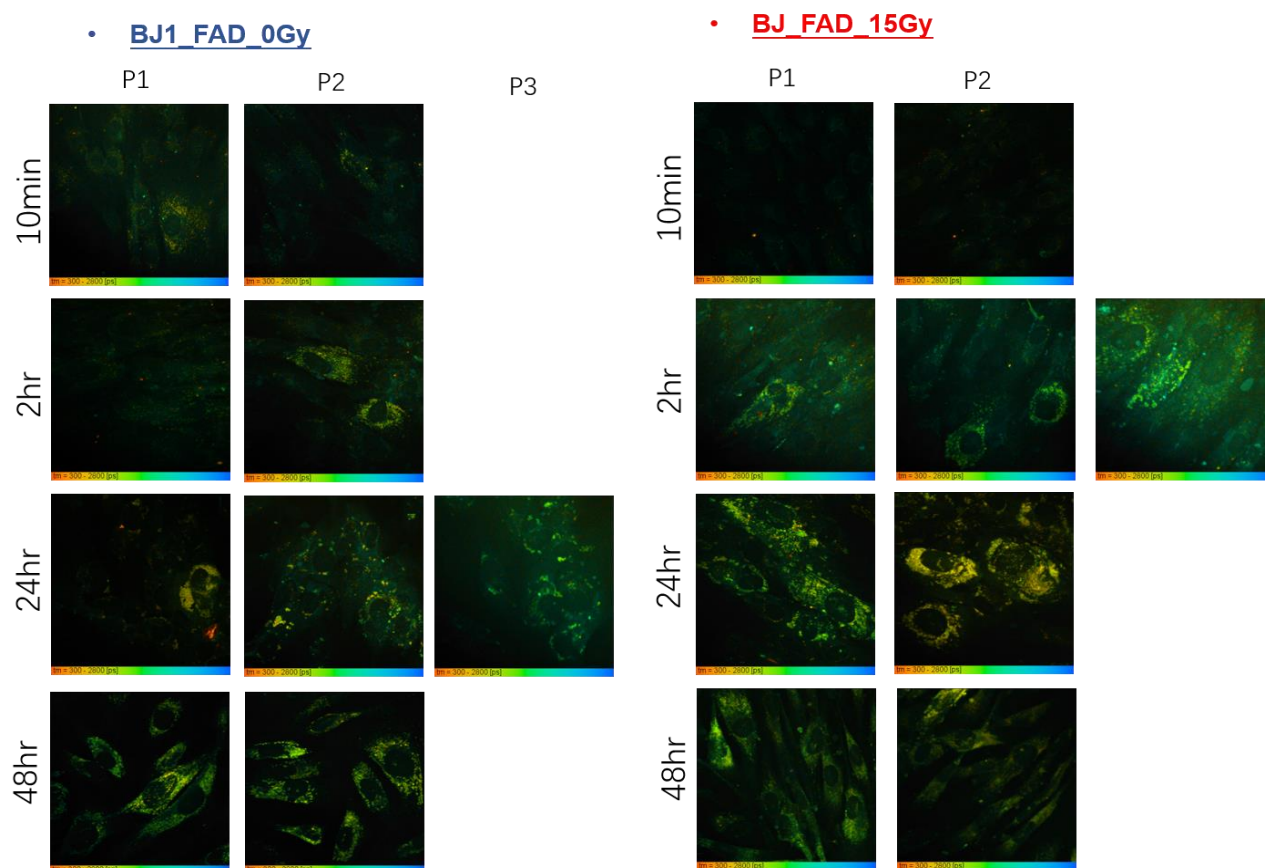


**Figure 4.32:** Detection of FAD life-time in 2D-cultured, fixed BJ1-hTert cells 10 min, 2 h, 24 h and 48 h after 15 Gy X-ray irradiation or mock-treatment. BJ1-hTert cells were excited with 672 nm light (TPEF), and fluorescence emission was collected with two-photon FLIM detector coupled with 525/530 nm (FAD) emission filters. For each time point two or three regions were investigated. The magnification is 40x.

FLIM data were also analyzed by 'phasor plot' analysis, using the SPCImage built-in program. Phasor analysis expresses the decay data in the individual pixels as phase and amplitude values in a polar diagram. Pixels with similar lifetime form a cluster, and they can be selected and reflexed on the images to further investigate the region of interests. Here, I focused on the NAD(P)H signal in the cytoplasm, which is related to energy production, and excluded the nuclear signal. It was found that the cytosolic NAD(P)H signal exhibits a similar vibration trend as the overview NAD(P)H signal (for example plots, see Appendix Figure S4.1, S4.2).

The metabolic shifts suggested by analysis of NAD(P)H fluorescence lifetime should be verified by independent methods. For example, they should be reflected in changes of mitochondrial characteristics such as size and perimeter lengths of mitochondrial structures. As the resolution of the FLIM picture is not sufficient to allow detailed determination of these parameters, in the next step mitochondria characteristics after irradiation were investigated after specific fluorescence staining.

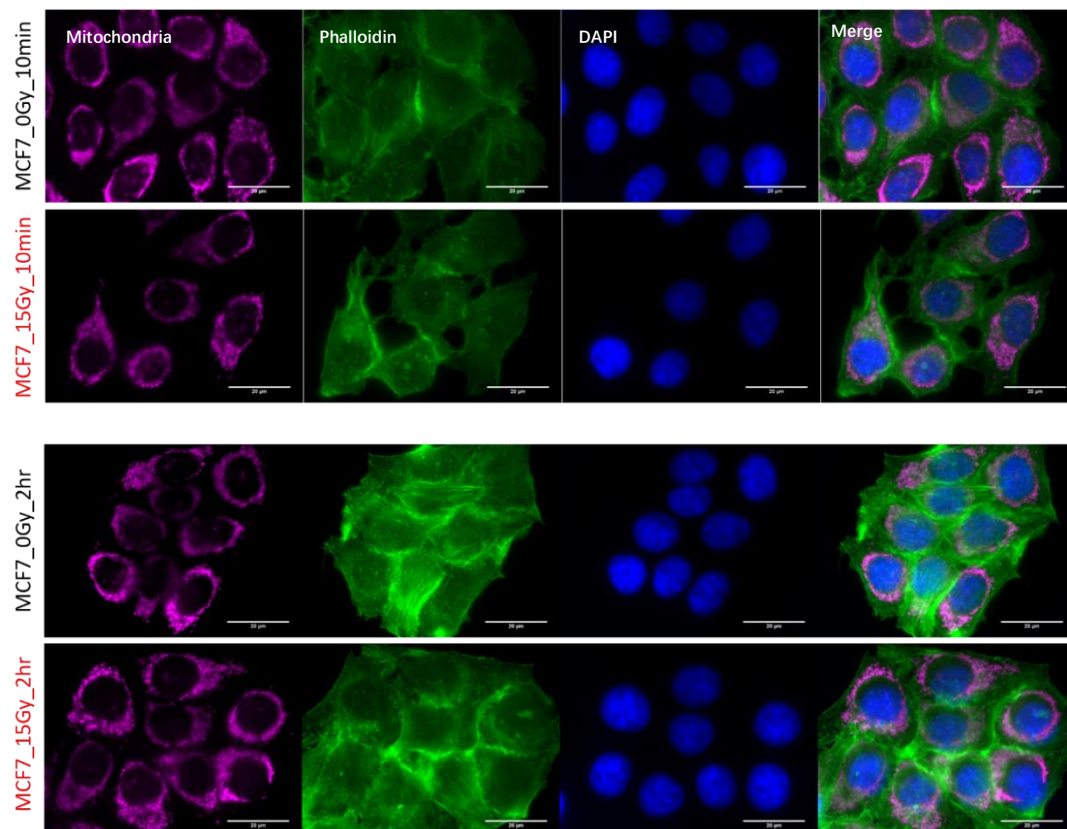
### 4.7.3 Radiation effects on mitochondrial morphology

MCF-7 and BJ1-hTert cells grown in 2D were treated with or without 15 Gy X-ray irradiation and fixed after 10 min, 2 h, 24 h, and 48 h. Cells were stained with MitoTracker dye (magenta), phalloidin (to show F-actin, in green) and DAPI (for MCF-7 see Figure 4.33, for BJ1-hTert see Figure 4.36).

Images were analyzed by ImageJ-based Macro Mito-Morphology, which was inspired by Stefan Strack, Ph.D., University of Iowa; and modified by Ruben K. Dagda at the University of Pittsburgh ([https://imagejdocu.tudor.lu/plugin/morphology/mitochondrial\\_morphology\\_macro\\_plugin/start](https://imagejdocu.tudor.lu/plugin/morphology/mitochondrial_morphology_macro_plugin/start)). In the analysis, the following parameters were calculated: number of mitochondrial particles, average area of particles and average perimeter of particles. For each data point, 20-30 cells were analyzed and statistical analysis was done by GraphPad Prism 8. Data are shown in Figure 4.34 for MCF-7 and Figure 4.37 for BJ1-hTert.

In unirradiated MCF-7 cells, the mitochondrial parameters do not alter over time in the 48 h observation period (Figure 4.34). However, in irradiated cells already at 10 min after irradiation, significant changes occur. At the early time points (10 min and 2 h), in MCF-7 cells, the number of mitochondrial particles decreases and their average size and perimeter increase. This suggests that mitochondrial fusion occurs, associated with increased use of oxidative phosphorylation. At later time points (24 h and 48 h), the number of mitochondrial particles increases while size and perimeter decrease in comparison to early time points, hinting at a fission process. However, number and size of particles remain

higher than in unirradiated controls – this could hint at an increase of total mitochondria mass. Indeed, an increase in total mitochondria mass is seen after irradiation that is more pronounced at 24 h and 48 h (Figure 4.35). This increase may in part be explained by G2-phase accumulation after irradiation. In support of this explanation, many MCF-7 nuclei increase in size after 24 h or 48 h, which may indicate G2-arrest.



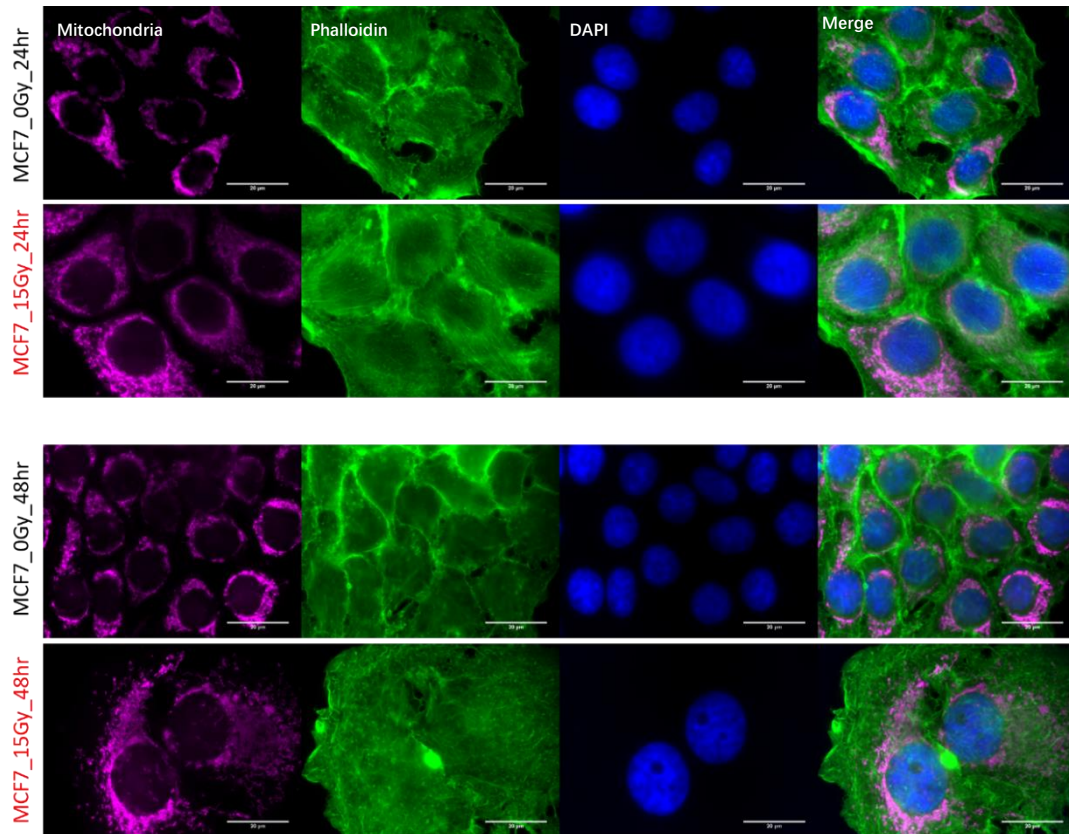


**Figure 4.33:** Mitochondria staining of MCF-7 cells with and without 15 Gy X-ray radiation treatment. Cells were fixed 10 min, 2 h, 24 h and 48 h post-irradiation. Mitochondria were stained with MitoTracker, F-actin was stained with phalloidin and nuclei were stained with DAPI. Scale bar is 20  $\mu\text{m}$

## Parameters of Mitochondria in MCF-7

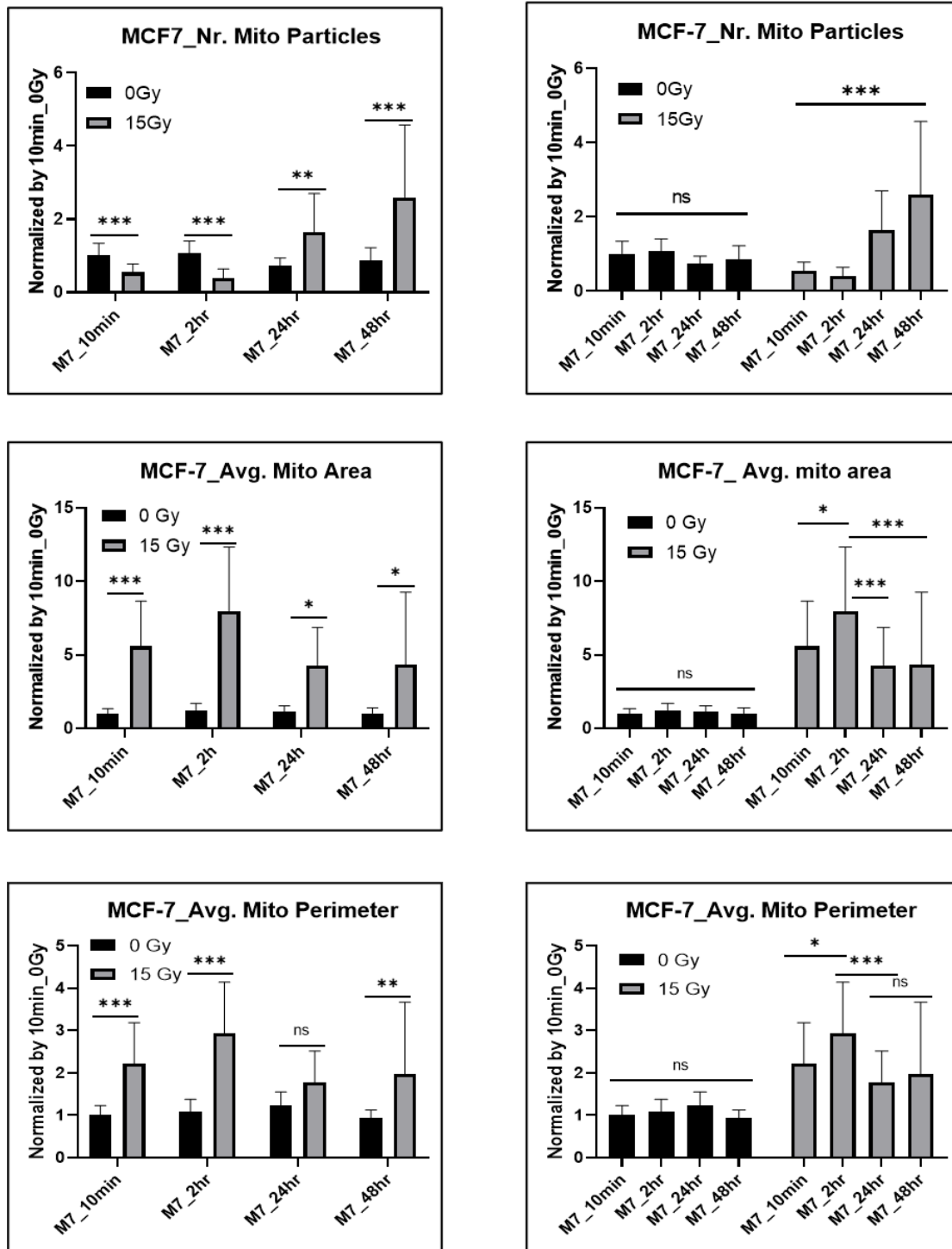


**Figure 4.34:** Morphological parameters (mitochondrial particle number, average mitochondrial area and average perimeter of mitochondrial particles) in MCF-7 cells after irradiation with 15 Gy. Mean and SD values of all groups are normalized to the mean of MCF-7 at 0 Gy, 10 min. To facilitate comparison, left panels compare unirradiated and

irradiated sample for each time point, while right panels display evolution over time. Tukey's test following two-way ANOVA was used to detect significant differences between the means of 3 or more independent groups. A  $p$  value  $\leq 0.05$  was considered statistically significant. Single, double and triple asterisks indicate significant differences with  $p$ -values of  $<0.05$ ,  $<0.01$  and  $<0.001$ , respectively.

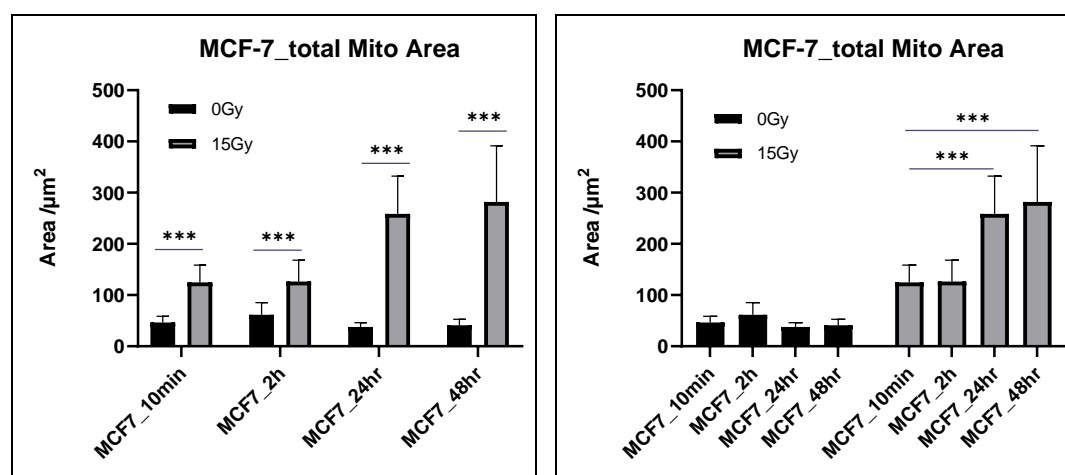


**Figure 4.35:** Total mitochondria area in MCF-7 cells after irradiation with 15 Gy. Mean and SD values of all groups are normalized to the mean of MCF-7 at 0 Gy, 10 min. Tukey's test following two-way ANOVA was used to detect significant differences between the means of 3 or more independent groups. A  $p$  value  $\leq 0.05$  was considered statistically significant. Single, double and triple asterisks indicate significant differences with  $p$ -values of  $<0.05$ ,  $<0.01$  and  $<0.001$ , respectively.

Overall, there is no significant difference between irradiated and unirradiated BJ1-hTert cells regarding the morphological parameters, except for a statistically significant increase of particle number after 48 h in irradiated cells (Figures 4.36, 4.37 and 4.38). Concerning particle area and perimeter, significant alterations are however seen over time, with smaller particle area and shorter perimeter at later time points (24 h and 48 h). While in the irradiated sample, this is accompanied by an increase in particle number, in the unirradiated sample only a non-significant trend is seen. Increased fragmentation of mitochondria over time suggests increased use of glycolytic energy generation and thus these observations support the NAD(P)H FLIM

results described above. Interestingly, perinuclear clustering appears not to increase at these later time points.

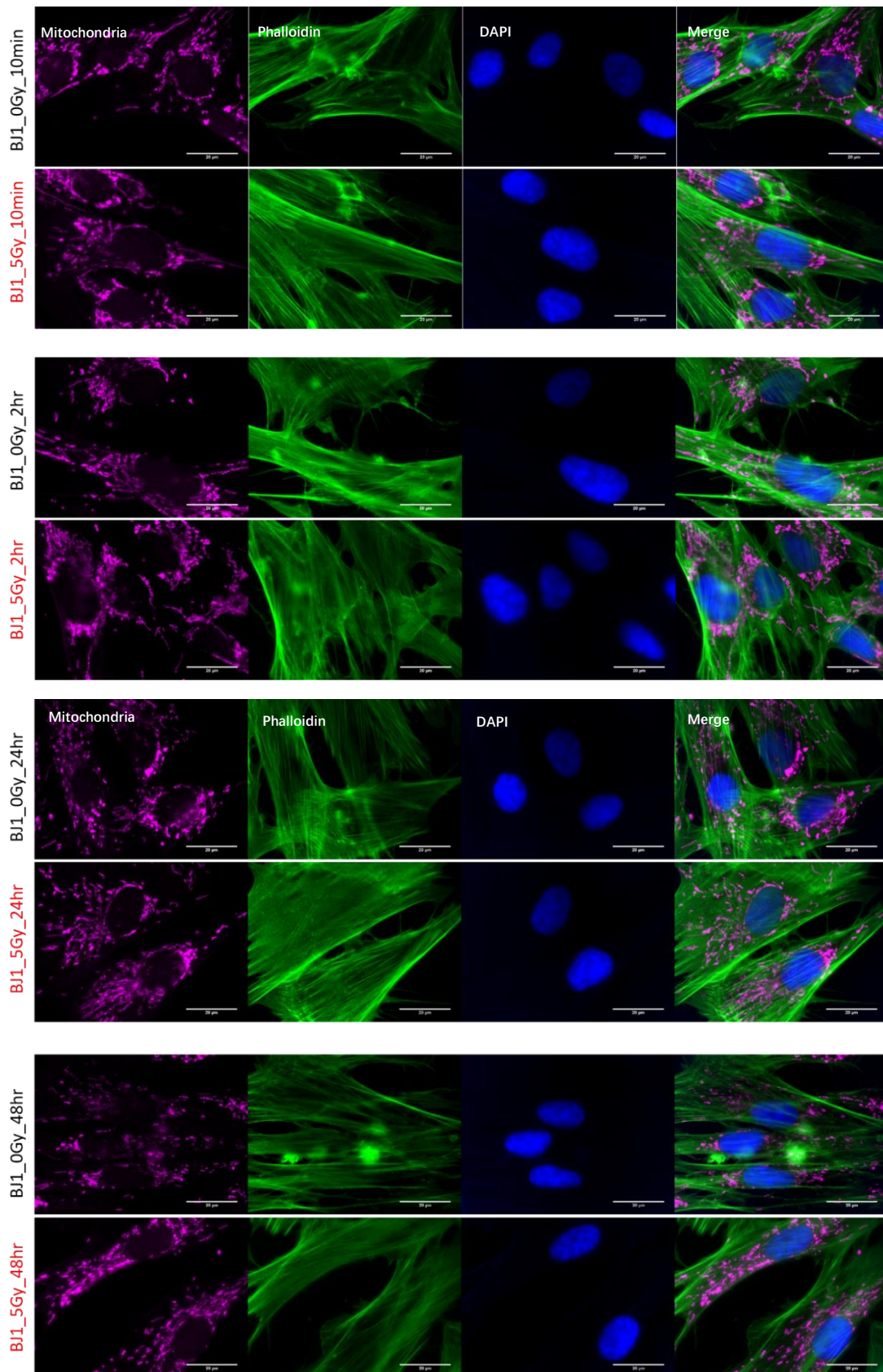


**Figure 4.36:** Mitochondria staining of BJ1-hTert cells with and without 15 Gy X-ray radiation treatment. Cells were fixed 10 min, 2 h, 24 h and 48 h post-irradiation. Mitochondria were stained with MitoTracker, F-actin was stained with phalloidin and nuclei were stained with DAPI. Scale bar is 20  $\mu$ m.

### Parameters of Mitochondria in BJ1-hTert

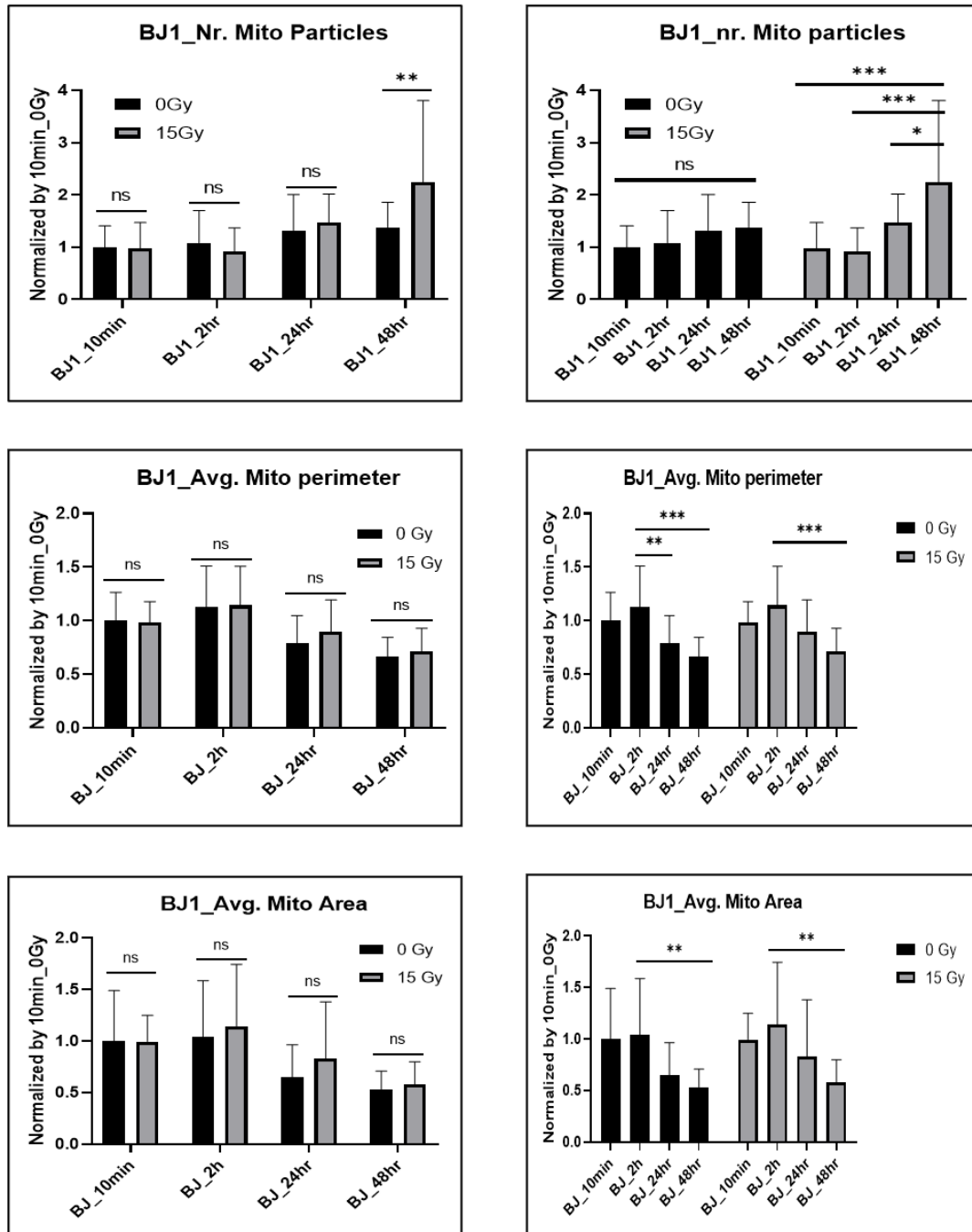


**Figure 4.37:** Morphological parameters (mitochondrial particle number, average

mitochondrial area and average perimeter of mitochondrial particles) in BJ1-hTert cells after irradiation with 15 Gy. Mean and SD values of all groups are normalized to the mean of BJ1-hTert at 0 Gy, 10 min. To facilitate comparison, left panels compare unirradiated and irradiated sample for each time point, while right panels display evolution over time. Tukey's test following two-way ANOVA was used to detect significant differences between the means of 3 or more independent groups. A  $p$  value  $\leq 0.05$  was considered statistically significant. Single, double and triple asterisks indicate significant differences with  $p$ -values of  $<0.05$ ,  $<0.01$  and  $<0.001$ , respectively.

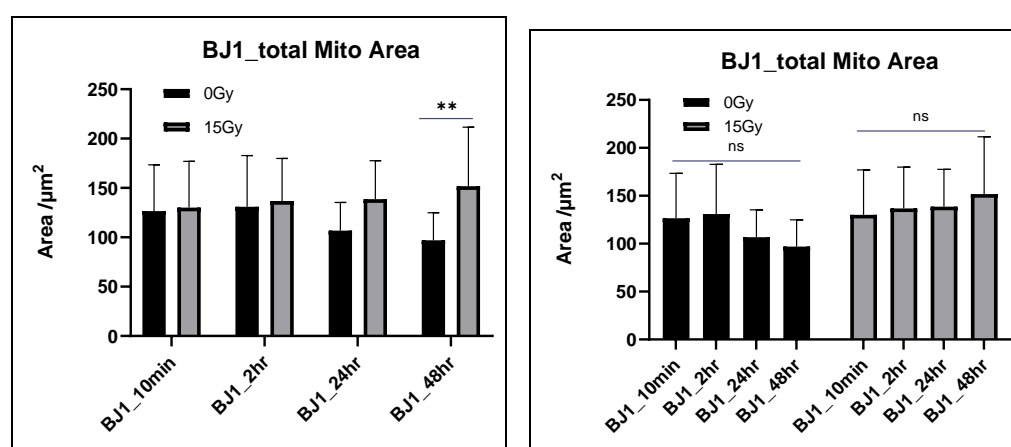


**Figure 4.38:** Total mitochondria area in BJ1-hTert cells after irradiation with 15 Gy. Mean and SD values of all groups are normalized to the mean of BJ1-hTert at 0 Gy, 10 min. Tukey's test following two-way ANOVA was used to detect significant differences between the means of 3 or more independent groups. A  $p$  value  $\leq 0.05$  was considered statistically significant. Single, double and triple asterisks indicate significant differences with  $p$ -values of  $<0.05$ ,  $<0.01$  and  $<0.001$ , respectively.

### Conclusion of 4.7

In this chapter, preliminary experiments were performed to test the applicability of TPEF and FLIM to investigate the fibroblast-led collective invasion models and radiation effects. The results obtained suggest that by FLIM, cancer cells and fibroblasts can be differentiated in a label-free manner and that information about metabolic processes can be gained. In addition, preliminary FLIM data suggest that MCF-7 cells undergo a transient metabolic shift towards oxidative

phosphorylation after irradiation, which could be verified by mitochondrial staining experiments. In contrast, in BJ1-hTert radiation had little effect on the investigated metabolic parameters.

## 5. Discussion

### 5.1 Choosing of 3D cell culture methods

*In vitro* cell culture methods are now universally used in biological and pharmaceutical research. They are robust tools for pre-clinical investigation which can help scientists to understand the fundamental biophysical and biomolecular mechanisms that occur *in vivo*. During last decades, 2D culturing has predominated and developed. However, recently, 3D cells culture methods are getting increasingly preferred by many researchers over conventional 2D culturing. It is assumed that 3D cultured cells are more physiologically relevant, mimicking better the cellular microenvironment and natural tissues. Therefore, turning 2D into 3D is necessary for robustly predicting the results of *in vitro* experiments and guiding the clinical research.

Many types of 3D culture methods have been developed. Choosing the appropriate method for investigation is critical. The decision of the right 3D culture method depends on the experimental goals, the experimental model system and the number of samples. Scaffold-free techniques provide single spheroids per well in multi-well plates. The size of spheroids can be easily controlled by the initial seeded cell numbers and cultivation timing. Spheroids are formed from a population of cells, rather than growing from a single cell with distinct properties. These cultivation means are appropriate for cell-based assays which require higher cell numbers, e.g., lysis of spheroids. A second advantage is that it is easier to generate co-culture structures when culturing in matrix-free 3D culture, where the real cell-cell contact is established. The influence of physical contact between two different types of cell lines is preserved, as well as the influence of soluble factors. This also holds for analysis of invasiveness, where spheroids grown by matrix-free techniques are subsequently embedded in matrix. In contrast, traditional transwell assays enable the investigation of only soluble factors effects on the other cell lines (Bogdanowicz and Lu 2013). Since a major aim of this study was to investigate invasion, I chose low adhesion plates to generate the 3D structures.

## 5.2 EMT marker expression vs. features of 3D spheroids

### Spheroid formation and invasiveness

Invasiveness of cancer cells is largely influenced by their epithelial vs. mesenchymal expression patterns. I chose 3 breast cancer cell lines described as having a more epithelial phenotype (MCF-7 (Luminal A), BT474 (Luminal B), and SkBr3 (HER-2 positive)) and for comparison one line with a more mesenchymal phenotype (MDA-MB-231 (triple Negative B)). Normally, luminal types of breast cancers are more differentiated and have tight cell-cell junctions, whereas triple-negative types are less differentiated, having a more mesenchymal-like appearance and higher invasive potential (Dai et al. 2017). A loss of epithelial differentiation and a shift towards a mesenchymal phenotype is correlated with malignancy and worse prognosis (Christiansen and Rajasekaran 2006). Three-dimensional tissue architecture is assembled and controlled by intercellular adhesion (Alimperti and Andreadis 2015), where E-cadherin as a type of cell adhesion molecule is important for binding cells with each other. Also, earlier results from Manuel Iglesias (Manuel Iglesias et al. 2013) indicated that the capability to form 3D structures is related to the expression of cadherins and integrins.

In a first step the growth behavior and expression patterns of these cell lines were verified. The western blotting results confirmed the distinct phenotypes of these four different cell lines, in which MCF-7 and BT474 expressed the epithelial markers E-Cadherin, Cytokeratin 18 and EpCAM. On the contrary, MDA-MB 231 expressed no epithelial markers but the mesenchymal marker vimentin. SkBr3 neither expressed E-cadherin nor vimentin. The morphology of these four breast cancer lines cultured both in 2D and 3D, as well as their invasiveness, corresponded highly to their EMT marker expression pattern. E-cadherin expressing MCF-7 and BT474 formed colonies when cultured in 2D and tight spheroids when cultured in 3D, while SkBr3 and MDA-MB-231 formed aggregates, but not tight spheroids. Only the triple-negative cell line with mesenchymal phenotype, MDA-MB-231, invaded the invasion matrix exhibiting a star-like invasion pattern. The HER-2 positive lines SkBr3 showed some shedding. Further analysis is necessary to reveal if this is related to an

amoeboid single cell invasion/migration. Thus, the ability to form spheroids and the inability to invade seem to correlate with a strong epithelial expression pattern, as expected. Interestingly, I also found that the expression of some EMT markers shifts according to the culturing methods. Especially MCF-7 and SkBr3 express much higher levels of EpCAM when cultivated in 3D than in 2D. A similar result was recently reported in colorectal cancer cells (Gisina et al. 2020).

The fibroblasts, BJ1-hTert and HDF, exhibited mesenchymal phenotype as expressing Vimentin, N-Cadherin and  $\alpha$ -SMA in western blot and/or IF. Both of them formed solid spheroids but showed no proliferation when cultured in 3D. Strong invasiveness was observed in collagen-rich matrix. These evidences showed again that the mesenchymal phenotype is correlated to the morphology of spheroids and their invasiveness.

To further systematically confirm the correlation between EMT markers, spheroid formation and invasion capability, knock-down of these EMT markers or application of some specific inhibitors on EMT transition promoters, like Snail family members, SNAI1 and SNAI2 (Cho et al. 2019) or Transforming growth Factor- $\beta$ , *TGF- $\beta$*  (Kasai et al. 2005) (Muraoka et al. 2002) can be applied to confirm the relevance to the 3D spheroid forming and invasion.

### **Proliferation**

The correlation between EMT transition and proliferation has rarely been confirmed. Salt et al. have confirmed that EMT transition modified the PI3K-dependent proliferation pathway, showing a reduction of serum-independent proliferation after EMT (Salt et al. 2014). From my results one cannot infer a difference of proliferation rate among these cell lines, since the measuring of spheroid size is not a robust way to compare between more compact or loose forms. To further investigate growth rate influences by EMT, assays as MTT or 3D spheroid fluorometric proliferation/ viability assay could be performed to obtain an overview of cell growth.

### **5.3 Influence on carcinoma cell lines of co-culture with normal fibroblasts**

#### **Co-culture effects on spheroid formation and proliferation**

Since the fibroblasts do not grow significantly when cocultured in 3D, the spheroid sizes here defined were dominated by the breast cancer lines. Co-culture did not appreciably affect spheroid formation of MCF-7 and BT474 cells, but it enhanced the aggregation of MDA-MB-231, which was indicated by smaller spherical area in co-cultured groups. Interestingly, co-cultured SkBr3 spheroids increased in size faster than the mono-culture spheroids. Further experiments are required to determine if this effect is due to better growth of the cancer cells or growth of the fibroblasts. While for MCF-7 and BT474 final spheroid sizes after 14-day cultivation were the same for mono-culture and co-culture spheroids, fitting of growth rates showed slower growth in co-cultures, reflecting the differences in initial spheroid size. Overall, adding fibroblasts just had a slight influence on spheroid growth in these cancer cell lines. Since normal fibroblasts rather than CAFs were used, limited paracrine signaling and secreted factors might be an explanation of why adding fibroblasts had little influence on the growth in the co-culture models (Räsänen and Vaheri 2010). Regarding radiation influence on spheroids growth, as expected, irradiation reduced spheroid growth significantly.

#### **Co-culture effects on invasiveness and its response to radiation**

The influence of fibroblasts on tumor progression has well been investigated. The impact of fibroblasts on the proliferation or response to radiation treatment depends on the cancer cell lines, and both pro- and anti-tumorigenic effects have been seen (Steer et al. 2019). Orimo and colleagues verified the promotion effects on growth and angiogenesis of human breast carcinomas by paracrine stimulation of stromal fibroblasts (Orimo et al. 2005) (Krakhmal et al. 2015). Recently, the function of human normal fibroblasts and rat normal fibroblasts to degrade the stromal matrix and enhance the invasiveness of cancer cells was described (Cao et al. 2016). This raises the question, whether this invasion promoting behavior is influenced positively or negatively by irradiation. Therefore, I established a direct co-culture model with normal fibroblast together with breast cancer cell lines to see how they respond to the

radiation treatment. I co-seeded fibroblasts and breast cancer cells together to generate “fibroblasts + breast cancer cells” spheroids. My findings indicated that adding normal fibroblasts helps the non-invasive cancer cells invade into surrounding matrix. Depending on fibroblast type, the number of invading cells was reduced or unaffected by the radiation treatment; the distance migrated by those cells which still remained invading was not significantly influenced by IR.

Previously, the invasion promoting effects of cancer-associated fibroblasts was reported to relate to the MMPs-mediated proteolysis (Liu T et al. 2010). To observe if the invasion enhancing mechanism is dependent on MMP related pathways, MMP inhibitors could be applied to investigate the promoting effects in further experiments.

### **Co-culture effects on fibroblast migration**

Addition of fibroblasts to pre-formed cancer cell spheroids has been proposed as a model for fibrotic processes (Wenzel et al. 2015). In MCF-7 and BT474 spheroids, addition of both fibroblast strains resulted in agglomeration of cells at the spheroid surface, followed by invagination and overgrowth by the cancer cells, resulting in one or a few fibroblast clusters in the co-culture spheroids. In contrast to Wenzel et al. (2015), I could not observe dissemination of the fibroblasts within the spheroids at later time points. The reason for this discrepancy is not clear.

There is accumulating evidence that the Rho/ROCK pathway is involved in processes like cell migration, invasion and metastasis. ROCK1 and ROCK2 expression is positively correlated to the tumor size of laryngeal squamous cell carcinoma; and ROCK1 is additionally correlated with lymph node metastasis (Zhang et al. 2015). The inhibitory effects on cell proliferation, migration and invasion by ROCK inhibitor, Y-27632, has been reported frequently (Wang et al. 2016) (Zhang et al. 2015). I applied Rho/ROCK inhibitor to investigate whether blocking the Rho/ROCK pathway will retard the migration of fibroblasts into the center of solid spheroids. The results show no influence on this process by adding ROCK inhibitor Y-27632, suggesting that the conglomeration of fibroblasts like BJ1-hTert and HDF on a cancer cell spheroid surface and their

---

movement into the interior of the spheroid is independent from this pathway.

#### **5.4 Dosages of radiation treatment**

Fractionated radiation treatment is the most common technique for cancer therapy. In contrast, in my research I applied just one single dose of 5 Gy or 15 Gy radiation during the experiments to investigate the radiation effects. 5 Gy was chosen since it is in the dose range where migration and invasion promoting effects of low LET irradiation were found with wound healing assays and Boyden Chamber assays (Li et al. 2020). Also, sublethal doses of irradiation enhance the invasion and dissemination is verified *in vivo* (Pei et al. 2015).

While logistically more difficult, it will be interesting to investigate in future whether fractionated irradiation affects invasiveness in the coculture model presented here. Fractionated irradiation, delivering 45 to 50 Gy accumulated dose in fractions of 2 Gy per day, is normally applied in radiotherapy (Buchholz 2009).

#### **5.5 New methods for estimating proliferation of spheroids and invasion in 3D model**

For estimating invasiveness, traditional 2D invasion assays in the Boyden Chamber only observe whether cells invade into the matrix or not, and determine the number of invaded cells from images from stained membranes. The observation of the invasion process cannot be real-time tracked and it is difficult to differentiate different invasion modes. Therefore, an important achievement in this thesis was to establish robust and powerful methods to estimate invasiveness happening in 3D.

To quantify invasiveness in 3D models, Liu et. al regarded the invasion area as total distributed area of tumor spheroids migrating in a micro-fluidic chamber and identified the invasion distance as the longest length measured from the

contact line to the location of the tumor spheroid migrating into micro-fluidic chamber (Liu et al. 2010). Others defined in 3D spherical invasion models the invasion distance as the distance from the spheroid edge to the population of invasive cells most distant from the spheroids edge (Tamaki et al. 1997) (Aw Yong et al. 2017).

I determined number of invading cells and invasion distance, using approaches that can differentiate between treatment effects on the binary ability of cells to invade and the distance invaded by those cells that can invade. With this I could show that radiation effects differ with these two endpoints, which thus can be uncoupled. For measuring the invasion distance, a new method was developed in collaboration with Christian Siebenwirth. The advantage of this method is that it considers the distance travelled by all invading cells, not only the furthest ones, thus reducing errors resulting from out-of-camera-field location of cells.

## **5.6 Imaging of 3D structures**

The biggest challenges to overcome when investigating 3D spheroids is to visualize the 3D structures. Poor penetration of light, optical light scattering and long acquisition times make the imaging of spheroids especially difficult (Białkowska et al. 2020). Thickness of 3D structures represents a technical challenge for assays like immunofluorescence detection within the spheroids and tissues. To overcome these problems, large structures need to be embedded in paraffin and then sectioned in order to have a better view inside the spheroids by conventional fluorescence microscopy. Alternatively, high resolution confocal images and non-linear optics imaging techniques are developed to enhance the observation inside the spheroids. In my thesis I applied normal light microscopy to get a rough overview of spheroids, epifluorescence microscopy with z-stack scanning to observe residual foci in spheroids, confocal microscopy to acquire high-resolution images of collective invasion models and FLIM and multi-modal microscopy to investigate the radiation effects on 3D models.

## 5.7 Imaging of NAD(P)H and FAD

NAD(P)H and FAD serve as metabolic co-enzymes which are associated with ATP production within cells. The concept of an Optical Redox Ratio (ORR) derived from autofluorescence intensity was firstly introduced by Chance (Chance et al. 1979). It is calculated as  $ORR = \text{Intensity of FAD} / [\text{Intensity of NAD(P)H} + \text{Intensity of FAD}]$ . This method depends on the ratio of concentrations rather than absolute concentrations and therefore facilitates comparisons between different cell types. Potential problems arise because the quantum yield of both FAD and NAD(P)H is low and other endogenous auto-fluorescent molecules, such as lipofuscin, collagen or hemoglobin can interfere (Kolenc and Quinn 2019).

Detection of these endogenous fluorophores by fluorescence lifetime imaging (FLIM) can overcome some of the problems associated with the ORR. FLIM exploits the difference in decay time between free and protein-bound FAD or NAD(P)H. Shifts in the mean decay time indicate metabolic shifts. FLIM became an effective tool for studying cellular metabolic dynamics in both *in vivo* and *ex vivo* conditions. The application of FLIM was shown to differentiate non-cancerous, low-grade or high-grade cancer cells or tissues by various researchers (Skala et al. 2007). Also, it has been applied to estimate the effects of anti-cancer drugs on organoids in chemotherapy (Sharick et al. 2019). However, its potential application to investigate radiation effects on cells or 3D spheroids has received little attention so far. Therefore, in this work originally a more extensive analysis of radiation effects and real-time dynamic changes of metabolic states in 3D models by FLIM and other forms of non-linear microscopy was planned. Unfortunately, after a few proof-of-principle experiments the project, which was performed in Jena in collaboration with the group of Prof. J. Popp, had to be discontinued due to the pandemic travel restrictions.

FLIM detection by time-correlated single photon counting (TCSPC) creates for each pixel a histogram of lifetimes that is fit by a bi-exponential function to determine lifetime and relative contribution of both components as well as a

mean lifetime. Compared to cells that perform oxidative phosphorylation (OXPHOS), a shift towards glycolysis results in more free-NADH and thus a shorter mean lifetime. Such a shift may be caused by hypoxia or by increased cellular demand for materials associated with high proliferation rates. The changes in mean NAD(P)H lifetime resulting from different metabolic situations are rather well understood. In contrast, FAD FLIM is less well understood.

My preliminary results suggest a transient metabolic shift towards OXPHOS in cancer cells after irradiation, which was not evident in fibroblasts. This shift was also reflected in changes in mitochondrial behavior, demonstrating that both methods can complement each other.

## 6. Prospects

In this research, I focused on MCF-7 and BT474 breast cancer cell lines in 3D culture and their fibroblasts-led collective invasion behavior. More epithelial-type cell lines should be investigated with regard to their invasiveness if co-cultivated with fibroblasts. Also, using other types of fibroblasts or even other types of stromal cells to co-culture with carcinoma cells in 3D would be a good idea to investigate generalization of the effects. The two fibroblast lines used here differed in their radiation response regarding invasiveness, but did not differ in sensitivity towards a radiomimetic drug with regard to viability. Here it has to be clarified if the discrepancy reflects differences of radiation vs radiomimetic drug, or different effects on viability vs invasive behavior. If the reduction in number of invading cells seen for BJ1-hTert after irradiation is not caused by loss of viability, but by radiation effects on the ability or decision to invade, investigation of the pathways involved would be important. The radiation effects on invasiveness of 3D cultured mesenchymal-type breast cancer lines, such as MDA-MB-231, which do not rely on fibroblasts is also interesting, necessary and crucial to understand which factors determine radiation effects on invasiveness.

Concerning the model of fibroblast-led collective invasion, it should be investigated if cancer cells simply and opportunistically follow in tracks provided by fibroblasts, or if there is some physical contact, e.g., via cadherin connections. Furthermore, it should be clarified if the generation of tracks and matrix remodeling by normal fibroblasts depends on MMPs, ROCK pathway, integrin  $\alpha 3$ ,  $\alpha 5$  and Rho-mediated regulation of myosin light chain (MLC), as reported by Gaggioli (Gaggioli et al. 2007) for cancer-associated fibroblasts.

Concerning the investigation of radiation effects on metabolism states by FLIM, more replicates should be imaged for quantification and controls should be included where metabolic pathways are disturbed by chemical inhibitors. Also, the original aim of my work, which was to investigate by non-linear optical methods the radiation effects on 3D spheroids and which could not proceed

due to the pandemic situation, should be followed in further work. Since the application of non-linear optical methods and staining-free imaging techniques will enable *in vivo* studies of radiation response, this is an important technique.

## 7. Reference

1. Alberts B, Johnson A, Lewis J, et al. 2002. "The Mitochondrion." *Molecular Biology of the Cell. 4th edition*. <https://www.ncbi.nlm.nih.gov/books/NBK26894/>. (last access 23 January 2023)
2. Alimperti S, Andreadis ST. CDH2 and CDH11 act as regulators of stem cell fate decisions. *Stem Cell Res.* 2015;14(3):270-282. doi:10.1016/j.scr.2015.02.002
3. Alkasalias T, Moyano-Galceran L, Arsenian-Henriksson M, Lehti K. Fibroblasts in the Tumor Microenvironment: Shield or Spear?. *Int J Mol Sci.* 2018;19(5):1532. doi:10.3390/ijms19051532
4. Ansems M, Span PN. The tumor microenvironment and radiotherapy response; a central role for cancer-associated fibroblasts. *Clin Transl Radiat Oncol.* 2020;22:90-97. doi:10.1016/j.ctro.2020.04.001
5. Atun R, Jaffray DA, Barton MB, et al. Expanding global access to radiotherapy. *Lancet Oncol.* 2015;16(10):1153-1186. doi:10.1016/S1470-2045(15)00222-3
6. Aw Yong KM, Li Z, Merajver SD, Fu J. Tracking the tumor invasion front using long-term fluidic tumoroid culture. *Sci Rep.* 2017;7(1):10784. doi:10.1038/s41598-017-10874-1
7. Becker, W. 2010. "The Bh TCSPC Handbook.", *9th edition, 2021, Scanning (800):* 1–566. <http://www.becker-hickl.de/handbook.htm>.
8. Benninger RKP, Piston DW. Two-photon excitation microscopy for the study of living cells and tissues. *Curr Protoc Cell Biol.* 2013; Chapter 4: Unit-4.11.24. doi:10.1002/0471143030.cb0411s59
9. Berezin MY, Achilefu S. Fluorescence lifetime measurements and biological imaging. *Chem Rev.* 2010;110(5):2641-2684. doi:10.1021/cr900343z
10. Białkowska K, Komorowski P, Bryszewska M, Miłowska K. Spheroids as a Type of Three-Dimensional Cell Cultures-Examples of Methods of Preparation and the Most Important Application. *Int J Mol Sci.* 2020;21(17):6225. doi:10.3390/ijms21176225
11. Birchmeier W, Behrens J. Cadherin expression in carcinomas: role in the formation of cell junctions and the prevention of invasiveness. *Biochim Biophys Acta.* 1994;1198(1):11-26. doi:10.1016/0304-419x(94)90003-5
12. Björklund M, Koivunen E. Gelatinase-mediated migration and invasion of cancer cells. *Biochim Biophys Acta.* 2005;1755(1):37-69. doi:10.1016/j.bbcan.2005.03.001
13. Blyth BJ, Cole AJ, MacManus MP, Martin OA. Radiation therapy-induced metastasis: radiobiology and clinical implications. *Clin Exp Metastasis.* 2018;35(4):223-236. doi:10.1007/s10585-017-9867-5

14. Bogdanowicz DR, Lu HH. Studying cell-cell communication in co-culture. *Biotechnol J*. 2013;8(4):395-396. doi:10.1002/biot.201300054
15. Bothmer A, Robbiani DF, Feldhahn N, Gazumyan A, Nussenzweig A, Nussenzweig MC. 53BP1 regulates DNA resection and the choice between classical and alternative end joining during class switch recombination. *J Exp Med*. 2010;207(4):855-865. doi:10.1084/jem.20100244
16. Bott K, Upton Z, Schrobback K, et al. The effect of matrix characteristics on fibroblast proliferation in 3D gels. *Biomaterials*. 2010;31(32):8454-8464. doi:10.1016/j.biomaterials.2010.07.046
17. Bratic I, Trifunovic A. Mitochondrial energy metabolism and ageing. *Biochim Biophys Acta*. 2010;1797(6-7):961-967. doi:10.1016/j.bbabi.2010.01.004
18. Bravo-Cordero JJ, Hodgson L, Condeelis J. Directed cell invasion and migration during metastasis. *Curr Opin Cell Biol*. 2012;24(2):277-283. doi:10.1016/j.ceb.2011.12.004
19. Brechbuhl HM, Barrett AS, Kopin E, et al. Fibroblast subtypes define a metastatic matrix in breast cancer. *JCI Insight*. 2020;5(4):e130751. doi:10.1172/jci.insight.130751
20. Buchholz TA. Radiation therapy for early-stage breast cancer after breast-conserving surgery. *N Engl J Med*. 2009;360(1):63-70. doi:10.1056/NEJMct0803525
21. Buchsbaum RJ, Oh SY. Breast Cancer-Associated Fibroblasts: Where We Are and Where We Need to Go. *Cancers (Basel)*. 2016;8(2):19. doi:10.3390/cancers8020019
22. Bunting SF, Callén E, Wong N, et al. 53BP1 inhibits homologous recombination in Brca1-deficient cells by blocking resection of DNA breaks. *Cell*. 2010;141(2):243-254. doi:10.1016/j.cell.2010.03.012
23. Cao H, Eppinga RD, Razidlo GL, et al. Stromal fibroblasts facilitate cancer cell invasion by a novel invadopodia-independent matrix degradation process. *Oncogene*. 2016;35(9):1099-1110. doi:10.1038/onc.2015.163
24. Cao L, Xu X, Bunting SF, et al. A selective requirement for 53BP1 in the biological response to genomic instability induced by Brca1 deficiency. *Mol Cell*. 2009;35(4):534-541. doi:10.1016/j.molcel.2009.06.037
25. Chacko JV, Eliceiri KW. Autofluorescence lifetime imaging of cellular metabolism: Sensitivity toward cell density, pH, intracellular, and intercellular heterogeneity. *Cytometry A*. 2019;95(1):56-69. doi:10.1002/cyto.a.23603
26. Chance B, Schoener B, Oshino R, Itshak F, Nakase Y. Oxidation-reduction ratio studies of mitochondria in freeze-trapped samples. NADH and flavoprotein fluorescence signals. *J Biol Chem*. 1979;254(11):4764-4771.
27. Chen H, Lisby M, Symington LS. RPA coordinates DNA end resection and prevents formation of DNA hairpins. *Mol Cell*. 2013;50(4):589-600.

- doi:10.1016/j.molcel.2013.04.032
28. Chitcholtan K, Asselin E, Parent S, Sykes PH, Evans JJ. Differences in growth properties of endometrial cancer in three dimensional (3D) culture and 2D cell monolayer. *Exp Cell Res*. 2013;319(1):75-87. doi:10.1016/j.yexcr.2012.09.012
  29. Cho ES, Kang HE, Kim NH, Yook JI. Therapeutic implications of cancer epithelial-mesenchymal transition (EMT). *Arch Pharm Res*. 2019;42(1):14-24. doi:10.1007/s12272-018-01108-7
  30. Christiansen JJ, Rajasekaran AK. Reassessing epithelial to mesenchymal transition as a prerequisite for carcinoma invasion and metastasis. *Cancer Res*. 2006;66(17):8319-8326. doi:10.1158/0008-5472.CAN-06-0410
  31. Clark AG, Vignjevic DM. Modes of cancer cell invasion and the role of the microenvironment. *Curr Opin Cell Biol*. 2015;36:13-22. doi:10.1016/j.ceb.2015.06.004
  32. Commander R, Wei C, Sharma A, et al. Subpopulation targeting of pyruvate dehydrogenase and GLUT1 decouples metabolic heterogeneity during collective cancer cell invasion. *Nat Commun*. 2020;11(1):1533. doi:10.1038/s41467-020-15219-7
  33. Correa Geyer F, Reis-Filho JS. Microarray-based gene expression profiling as a clinical tool for breast cancer management: are we there yet?. *Int J Surg Pathol*. 2009;17(4):285-302. doi:10.1177/1066896908328577
  34. Cunniff B, McKenzie AJ, Heintz NH, Howe AK. AMPK activity regulates trafficking of mitochondria to the leading edge during cell migration and matrix invasion. *Mol Biol Cell*. 2016;27(17):2662-2674. doi:10.1091/mbc.E16-05-0286
  35. Dai X, Cheng H, Bai Z, Li J. Breast Cancer Cell Line Classification and Its Relevance with Breast Tumor Subtyping. *J Cancer*. 2017;8(16):3131-3141. doi:10.7150/jca.18457
  36. Daley JM, Sung P. 53BP1, BRCA1, and the choice between recombination and end joining at DNA double-strand breaks. *Mol Cell Biol*. 2014;34(8):1380-1388. doi:10.1128/MCB.01639-13
  37. Dasika GK, Lin SC, Zhao S, Sung P, Tomkinson A, Lee EY. DNA damage-induced cell cycle checkpoints and DNA strand break repair in development and tumorigenesis. *Oncogene*. 1999;18(55):7883-7899. doi:10.1038/sj.onc.1203283
  38. Dvorak KM, Pettee KM, Rubinic-Minotti K, Su R, Nestor-Kalinowski A, Eisenmann KM. Carcinoma associated fibroblasts (CAFs) promote breast cancer motility by suppressing mammalian Diaphanous-related formin-2 (mDia2). *PLoS One*. 2018;13(3):e0195278. doi:10.1371/journal.pone.0195278
  39. Eliyatkin N, Yalçın E, Zengel B, Aktaş S, Vardar E. Molecular Classification of Breast Carcinoma: From Traditional, Old-Fashioned Way to A New Age, and A New Way. *J*

- Breast Health*. 2015;11(2):59-66. doi:10.5152/tjbh.2015.1669
40. Escribano-Díaz C, Orthwein A, Fradet-Turcotte A, et al. A cell cycle-dependent regulatory circuit composed of 53BP1-RIF1 and BRCA1-CtIP controls DNA repair pathway choice. *Mol Cell*. 2013;49(5):872-883. doi:10.1016/j.molcel.2013.01.001
  41. Fang G, Lu H, Law A, Gallego-Ortega D, Jin D, Lin G. Gradient-sized control of tumor spheroids on a single chip. *Lab Chip*. 2019;19(24):4093-4103. doi:10.1039/c9lc00872a
  42. Fontana F, Raimondi M, Marzagalli M, Sommariva M, Limonta P, Gagliano N. Epithelial-To-Mesenchymal Transition Markers and CD44 Isoforms Are Differently Expressed in 2D and 3D Cell Cultures of Prostate Cancer Cells. *Cells*. 2019;8(2):143. doi:10.3390/cells8020143
  43. Foty RA, Steinberg MS. The differential adhesion hypothesis: a direct evaluation. *Dev Biol*. 2005;278(1):255-263. doi:10.1016/j.ydbio.2004.11.012
  44. Fujita M, Yamada S, Imai T. Irradiation induces diverse changes in invasive potential in cancer cell lines. *Semin Cancer Biol*. 2015;35:45-52. doi:10.1016/j.semcancer.2015.09.003
  45. Gaedtke L, Thoenes L, Culmsee C, Mayer B, Wagner E. Proteomic analysis reveals differences in protein expression in spheroid versus monolayer cultures of low-passage colon carcinoma cells. *J Proteome Res*. 2007;6(11):4111-4118. doi:10.1021/pr0700596
  46. Gaggioli C, Hooper S, Hidalgo-Carcedo C, et al. Fibroblast-led collective invasion of carcinoma cells with differing roles for RhoGTPases in leading and following cells. *Nat Cell Biol*. 2007;9(12):1392-1400. doi:10.1038/ncb1658
  47. Gaggioli C. Collective invasion of carcinoma cells: when the fibroblasts take the lead. *Cell Adh Migr*. 2008;2(1):45-47. doi:10.4161/cam.2.1.5705
  48. Geiger Anika, Protein expression, growth and invasion behaviour of mamma carcinoma cells after irradiation in 3D spheroids. Master thesis, Faculty of Biology, Ludwig-Maximilians-University, Munich, 2019
  49. Giancaspero TA, Busco G, Panebianco C, et al. FAD synthesis and degradation in the nucleus create a local flavin cofactor pool. *J Biol Chem*. 2013;288(40):29069-29080. doi:10.1074/jbc.M113.500066
  50. Gisina AM, Kim YS, Gabashvili AN, et al. Expression of Epithelial Cell Adhesion Molecule (EpCAM) in Tumor Spheroids of Human Colorectal Adenocarcinoma Cells. *Bull Exp Biol Med*. 2020;170(1):135-141. doi:10.1007/s10517-020-05018-x
  51. Grünert S, Jechlinger M, Beug H. Diverse cellular and molecular mechanisms contribute to epithelial plasticity and metastasis. *Nat Rev Mol Cell Biol*. 2003;4(8):657-665. doi:10.1038/nrm1175
  52. Huang H, Manton KG. The role of oxidative damage in mitochondria during aging: a

- review. *Front Biosci.* 2004;9:1100-1117. doi:10.2741/1298
53. Hooper S, Gaggioli C, Sahai E. A chemical biology screen reveals a role for Rab21-mediated control of actomyosin contractility in fibroblast-driven cancer invasion. *Br J Cancer.* 2010;102(2):392-402. doi:10.1038/sj.bjc.6605469
54. Houtgraaf JH, Versmissen J, van der Giessen WJ. A concise review of DNA damage checkpoints and repair in mammalian cells. *Cardiovasc Revasc Med.* 2006;7(3):165-172. doi:10.1016/j.carrev.2006.02.002
55. Herrmann JM, Riemer J. The intermembrane space of mitochondria. *Antioxid Redox Signal.* 2010;13(9):1341-1358. doi:10.1089/ars.2009.3063
56. Johan MZ, Samuel MS. Rho-ROCK signaling regulates tumor-microenvironment interactions. *Biochem Soc Trans.* 2019;47(1):101-108. doi:10.1042/BST20180334
57. Justus CR, Leffler N, Ruiz-Echevarria M, Yang LV. In vitro cell migration and invasion assays. *J Vis Exp.* 2014;(88):51046. doi:10.3791/51046
58. Kalinina S, Freymueller C, Naskar N, et al. Bioenergetic Alterations of Metabolic Redox Coenzymes as NADH, FAD and FMN by Means of Fluorescence Lifetime Imaging Techniques. *Int J Mol Sci.* 2021;22(11):5952. doi:10.3390/ijms22115952
59. Kam WW, Banati RB. Effects of ionizing radiation on mitochondria. *Free Radic Biol Med.* 2013;65:607-619. doi:10.1016/j.freeradbiomed.2013.07.024
60. Kasai H, Allen JT, Mason RM, Kamimura T, Zhang Z. TGF-beta1 induces human alveolar epithelial to mesenchymal cell transition (EMT). *Respir Res.* 2005;6(1):56. doi:10.1186/1465-9921-6-56
61. Kenny PA, Lee GY, Myers CA, et al. The morphologies of breast cancer cell lines in three-dimensional assays correlate with their profiles of gene expression. *Mol Oncol.* 2007;1(1):84-96. doi:10.1016/j.molonc.2007.02.004
62. Kolenc OI, Quinn KP. Evaluating Cell Metabolism Through Autofluorescence Imaging of NAD(P)H and FAD. *Antioxid Redox Signal.* 2019;30(6):875-889. doi:10.1089/ars.2017.7451
63. Koontongkaew S. The tumor microenvironment contribution to development, growth, invasion and metastasis of head and neck squamous cell carcinomas. *J Cancer.* 2013;4(1):66-83. doi:10.7150/jca.5112
64. Krajewska M, Fehrmann RS, de Vries EG, van Vugt MA. Regulators of homologous recombination repair as novel targets for cancer treatment. *Front Genet.* 2015;6:96. doi:10.3389/fgene.2015.00096
65. Krakhmal NV, Zavyalova MV, Denisov EV, Vtorushin SV, Perelmuter VM. Cancer Invasion: Patterns and Mechanisms. *Acta Naturae.* 2015;7(2):17-28.
66. Kühlbrandt W. Structure and function of mitochondrial membrane protein complexes. *BMC Biol.* 2015;13:89. doi:10.1186/s12915-015-0201-x
67. Kunz-Schughart LA, Kreutz M, Knuechel R. Multicellular spheroids: a three-

- dimensional in vitro culture system to study tumour biology. *Int J Exp Pathol*. 1998;79(1):1-23. doi:10.1046/j.1365-2613.1998.00051.x
68. Labernadie A, Kato T, Brugués A, et al. A mechanically active heterotypic E-cadherin/N-cadherin adhesion enables fibroblasts to drive cancer cell invasion. *Nat Cell Biol*. 2017;19(3):224-237. doi:10.1038/ncb3478
69. Lackner LL. Shaping the dynamic mitochondrial network. *BMC Biol*. 2014;12:35. doi:10.1186/1741-7007-12-35
70. Li J, Wu DM, Han R, et al. Low-Dose Radiation Promotes Invasion and Migration of A549 Cells by Activating the CXCL1/NF- $\kappa$ B Signaling Pathway. *Onco Targets Ther*. 2020;13:3619-3629. doi:10.2147/OTT.S243914
71. Li S, Lao J, Chen BP, et al. Genomic analysis of smooth muscle cells in 3-dimensional collagen matrix [published correction appears in *FASEB J*. 2003 Jul;17(10):1376]. *FASEB J*. 2003;17(1):97-99. doi:10.1096/fj.02-0256fje
72. Lin RZ, Chang HY. Recent advances in three-dimensional multicellular spheroid culture for biomedical research [published correction appears in *Biotechnol J*. 2008 Oct;3(9-10): 1172-1184. doi:10.1002/biot.200700228
73. Lin RZ, Chou LF, Chien CC, Chang HY. Dynamic analysis of hepatoma spheroid formation: roles of E-cadherin and beta1-integrin. *Cell Tissue Res*. 2006;324(3):411-422. doi:10.1007/s00441-005-0148-2
74. Liu J, Doty T, Gibson B, Heyer WD. Human BRCA2 protein promotes RAD51 filament formation on RPA-covered single-stranded DNA. *Nat Struct Mol Biol*. 2010;17(10):1260-1262. doi:10.1038/nsmb.1904
75. Liu T, Lin B, Qin J. Carcinoma-associated fibroblasts promoted tumor spheroid invasion on a microfluidic 3D co-culture device. *Lab Chip*. 2010;10(13):1671-1677. doi:10.1039/c000022a
76. Liu Z, Pouli D, Alonzo CA, et al. Mapping metabolic changes by noninvasive, multiparametric, high-resolution imaging using endogenous contrast. *Sci Adv*. 2018;4(3):eaap9302. doi:10.1126/sciadv.aap9302
77. Madri JA, Graesser D. Cell migration in the immune system: the evolving inter-related roles of adhesion molecules and proteinases. *Dev Immunol*. 2000;7(2-4):103-116. doi:10.1155/2000/79045
78. Mah LJ, El-Osta A, Karagiannis TC. gammaH2AX: a sensitive molecular marker of DNA damage and repair. *Leukemia*. 2010;24(4):679-686. doi:10.1038/leu.2010.6
79. Manuel Iglesias J, Beloqui I, Garcia-Garcia F, et al. Mammosphere formation in breast carcinoma cell lines depends upon expression of E-cadherin. *PLoS One*. 2013;8(10):e77281. doi:10.1371/journal.pone.0077281
80. Marková E, Schultz N, Belyaev IY. Kinetics and dose-response of residual 53BP1/gamma-H2AX foci: co-localization, relationship with DSB repair and

- clonogenic survival. *Int J Radiat Biol.* 2007;83(5):319-329.  
doi:10.1080/09553000601170469
81. Mishra P, Chan DC. Metabolic regulation of mitochondrial dynamics. *J Cell Biol.* 2016;212(4):379-387. doi:10.1083/jcb.201511036
82. Moncharmont C, Levy A, Guy JB, et al. Radiation-enhanced cell migration/invasion process: a review. *Crit Rev Oncol Hematol.* 2014;92(2):133-142.  
doi:10.1016/j.critrevonc.2014.05.006
83. Mosier JA, Schwager SC, Boyajian DA, Reinhart-King CA. Cancer cell metabolic plasticity in migration and metastasis. *Clin Exp Metastasis.* 2021;38(4):343-359.  
doi:10.1007/s10585-021-10102-1
84. Mueller-Klieser W. Method for the determination of oxygen consumption rates and diffusion coefficients in multicellular spheroids. *Biophys J.* 1984;46(3):343-348.  
doi:10.1016/S0006-3495(84)84030-8
85. Muraoka RS, Dumont N, Ritter CA, et al. Blockade of TGF-beta inhibits mammary tumor cell viability, migration, and metastases. *J Clin Invest.* 2002;109(12):1551-1559. doi:10.1172/JCI15234
86. Nagai T, Ishikawa T, Minami Y, Nishita M. Tactics of cancer invasion: solitary and collective invasion. *J Biochem.* 2020;167(4):347-355. doi:10.1093/jb/mvaa003
87. Nakamura K, Kogame T, Oshiumi H, et al. Collaborative action of Brca1 and CtIP in elimination of covalent modifications from double-strand breaks to facilitate subsequent break repair. *PLoS Genet.* 2010;6(1):e1000828.  
doi:10.1371/journal.pgen.1000828
88. Neupert W, Herrmann JM. Translocation of proteins into mitochondria. *Annu Rev Biochem.* 2007;76:723-749. doi:10.1146/annurev.biochem.76.052705.163409
89. Olumi AF, Grossfeld GD, Hayward SW, Carroll PR, Tlsty TD, Cunha GR. Carcinoma-associated fibroblasts direct tumor progression of initiated human prostatic epithelium. *Cancer Res.* 1999;59(19):5002-5011. doi:10.1186/bcr138
90. Orimo A, Gupta PB, Sgroi DC, et al. Stromal fibroblasts present in invasive human breast carcinomas promote tumor growth and angiogenesis through elevated SDF-1/CXCL12 secretion. *Cell.* 2005;121(3):335-348. doi:10.1016/j.cell.2005.02.034
91. Orth M, Lauber K, Niyazi M, et al. Current concepts in clinical radiation oncology. *Radiat Environ Biophys.* 2014;53(1):1-29. doi:10.1007/s00411-013-0497-2
92. Pal A, Ashworth JC, Collier P, et al. A 3D Heterotypic Breast Cancer Model Demonstrates a Role for Mesenchymal Stem Cells in Driving a Proliferative and Invasive Phenotype. *Cancers (Basel).* 2020;12(8):2290.  
doi:10.3390/cancers12082290
93. Palumbo MO, Kavan P, Miller WH Jr, et al. Systemic cancer therapy: achievements and challenges that lie ahead. *Front Pharmacol.* 2013;4:57.

- doi:10.3389/fphar.2013.00057
94. Pampaloni F, Reynaud EG, Stelzer EH. The third dimension bridges the gap between cell culture and live tissue. *Nat Rev Mol Cell Biol.* 2007;8(10):839-845. doi:10.1038/nrm2236
  95. Pei J, Park IH, Ryu HH, et al. Sublethal dose of irradiation enhances invasion of malignant glioma cells through p53-MMP 2 pathway in U87MG mouse brain tumor model. *Radiat Oncol.* 2015;10:164. doi:10.1186/s13014-015-0475-8
  96. Poincloux R, Collin O, Lizárraga F, et al. Contractility of the cell rear drives invasion of breast tumor cells in 3D Matrigel. *Proc Natl Acad Sci U S A.* 2011;108(5):1943-1948. doi:10.1073/pnas.1010396108
  97. Povirk LF. DNA damage and mutagenesis by radiomimetic DNA-cleaving agents: bleomycin, neocarzinostatin and other enediynes. *Mutat Res.* 1996;355(1-2):71-89. doi:10.1016/0027-5107(96)00023-1
  98. Quail DF, Joyce JA. Microenvironmental regulation of tumor progression and metastasis. *Nat Med.* 2013;19(11):1423-1437. doi:10.1038/nm.3394
  99. Ralph ACL, Valadão IC, Cardoso EC, et al. Environmental control of mammary carcinoma cell expansion by acidification and spheroid formation in vitro. *Sci Rep.* 2020;10(1):21959. doi:10.1038/s41598-020-78989-6
  100. Ranjit S, Malacrida L, Jameson DM, Gratton E. Fit-free analysis of fluorescence lifetime imaging data using the phasor approach. *Nat Protoc.* 2018;13(9):1979-2004. doi:10.1038/s41596-018-0026-5
  101. Räsänen K, Vaheri A. Activation of fibroblasts in cancer stroma. *Exp Cell Res.* 2010;316(17):2713-2722. doi:10.1016/j.yexcr.2010.04.032
  102. Ravi M, Paramesh V, Kaviya SR, Anuradha E, Solomon FD. 3D cell culture systems: advantages and applications. *J Cell Physiol.* 2015;230(1):16-26. doi:10.1002/jcp.24683
  103. Roberts GC, Morris PG, Moss MA, et al. An Evaluation of Matrix-Containing and Humanised Matrix-Free 3-Dimensional Cell Culture Systems for Studying Breast Cancer. *PLoS One.* 2016;11(6):e0157004. doi:10.1371/journal.pone.0157004
  104. Rockwell S, Dobrucki IT, Kim EY, Marrison ST, Vu VT. Hypoxia and radiation therapy: past history, ongoing research, and future promise. *Curr Mol Med.* 2009;9(4):442-458. doi:10.2174/156652409788167087
  105. Romero-Garcia S, Moreno-Altamirano MM, Prado-Garcia H, Sánchez-García FJ. Lactate Contribution to the Tumor Microenvironment: Mechanisms, Effects on Immune Cells and Therapeutic Relevance. *Front Immunol.* 2016;7:52. doi:10.3389/fimmu.2016.00052
  106. Rose AA, Siegel PM. Emerging therapeutic targets in breast cancer bone metastasis. *Future Oncol.* 2010;6(1):55-74. doi:10.2217/fon.09.138

107. Roussos ET, Condeelis JS, Patsialou A. Chemotaxis in cancer. *Nat Rev Cancer*. 2011;11(8):573-587. doi:10.1038/nrc3078
108. Rubart M. Two-photon microscopy of cells and tissue. *Circ Res*. 2004;95(12):1154-1166. doi:10.1161/01.RES.0000150593.30324.42
109. Rupp AM. Vermessung von Tumorzell-Sphäroiden mit Hilfe von entwickelten Plug-Ins. Bachelor Thesis, Faculty of Physics, LMU University Munich (2019).
110. Salt MB, Bandyopadhyay S, McCormick F. Epithelial-to-mesenchymal transition rewires the molecular path to PI3K-dependent proliferation. *Cancer Discov*. 2014;4(2):186-199. doi:10.1158/2159-8290.CD-13-0520
111. Schaefer PM, Kalinina S, Rueck A, von Arnim CAF, von Einem B. NADH Autofluorescence-A Marker on its Way to Boost Bioenergetic Research. *Cytometry A*. 2019;95(1):34-46. doi:10.1002/cyto.a.23597
112. Schipper JH, Frixen UH, Behrens J, Unger A, Jahnke K, Birchmeier W. E-cadherin expression in squamous cell carcinomas of head and neck: inverse correlation with tumor dedifferentiation and lymph node metastasis. *Cancer Res*. 1991;51(23 Pt 1):6328-6337.
113. Schnitt SJ. Will molecular classification replace traditional breast pathology?. *Int J Surg Pathol*. 2010;18(3 Suppl):162S-166S. doi:10.1177/1066896910370771
114. Seluanov A, Mittelman D, Pereira-Smith OM, Wilson JH, Gorbunova V. DNA end joining becomes less efficient and more error-prone during cellular senescence. *Proc Natl Acad Sci U S A*. 2004;101(20):7624-7629. doi:10.1073/pnas.0400726101
115. Sharick JT, Jeffery JJ, Karim MR, et al. Cellular Metabolic Heterogeneity In Vivo Is Recapitulated in Tumor Organoids. *Neoplasia*. 2019;21(6):615-626. doi:10.1016/j.neo.2019.04.004
116. Siegel RL, Miller KD, Jemal A. Cancer statistics, 2020. *CA Cancer J Clin*. 2020;70(1):7-30. doi:10.3322/caac.21590
117. Skala MC, Riching KM, Bird DK, et al. In vivo multiphoton fluorescence lifetime imaging of protein-bound and free nicotinamide adenine dinucleotide in normal and precancerous epithelia. *J Biomed Opt*. 2007;12(2):024014. doi:10.1117/1.2717503
118. Smolková K, Plecítá-Hlavatá L, Bellance N, Benard G, Rossignol R, Ježek P. Waves of gene regulation suppress and then restore oxidative phosphorylation in cancer cells. *Int J Biochem Cell Biol*. 2011;43(7):950-968. doi:10.1016/j.biocel.2010.05.003
119. Souza GR, Molina JR, Raphael RM, et al. Three-dimensional tissue culture based on magnetic cell levitation. *Nat Nanotechnol*. 2010; 5(4):291-296. doi:10.1038/nnano.2010.23
120. Steer A, Cordes N, Jendrossek V, Klein D. Impact of Cancer-Associated Fibroblast on the Radiation-Response of Solid Xenograft Tumors. *Front Mol Biosci*. 2019;6:70. doi:10.3389/fmolb.2019.00070

121. Stone RC, Pastar I, Ojeh N, et al. Epithelial-mesenchymal transition in tissue repair and fibrosis. *Cell Tissue Res.* 2016;365(3):495-506. doi:10.1007/s00441-016-2464-0
122. Svoboda K, Yasuda R. Principles of two-photon excitation microscopy and its applications to neuroscience. *Neuron.* 2006;50(6):823-839. doi:10.1016/j.neuron.2006.05.019
123. Tahtamouni L, Ahram M, Koblinski J, Rolfo C. Molecular Regulation of Cancer Cell Migration, Invasion, and Metastasis. *Anal Cell Pathol (Amst).* 2019;2019:1356508. doi:10.1155/2019/1356508
124. Tamaki M, McDonald W, Amberger VR, Moore E, Del Maestro RF. Implantation of C6 astrocytoma spheroid into collagen type I gels: invasive, proliferative, and enzymatic characterizations. *J Neurosurg.* 1997;87(4):602-609. doi:10.3171/jns.1997.87.4.0602
125. Thiery JP. Epithelial-mesenchymal transitions in tumour progression. *Nat Rev Cancer.* 2002;2(6):442-454. doi:10.1038/nrc822
126. Timmins NE, Harding FJ, Smart C, Brown MA, Nielsen LK. Method for the generation and cultivation of functional three-dimensional mammary constructs without exogenous extracellular matrix. *Cell Tissue Res.* 2005;320(1):207-210. doi:10.1007/s00441-004-1064-6
127. Varone A, Xylas J, Quinn KP, et al. Endogenous two-photon fluorescence imaging elucidates metabolic changes related to enhanced glycolysis and glutamine consumption in precancerous epithelial tissues. *Cancer Res.* 2014;74(11):3067-3075. doi:10.1158/0008-5472.CAN-13-2713
128. Viallard C, Larrivée B. Tumor angiogenesis and vascular normalization: alternative therapeutic targets. *Angiogenesis.* 2017;20(4):409-426. doi:10.1007/s10456-017-9562-9
129. Wang ZM, Yang DS, Liu J, Liu HB, Ye M, Zhang YF. ROCK inhibitor Y-27632 inhibits the growth, migration, and invasion of Tca8113 and CAL-27 cells in tongue squamous cell carcinoma. *Tumour Biol.* 2016;37(3):3757-3764. doi:10.1007/s13277-015-4115-6
130. Warburg, O. Über den Stoffwechsel der Carcinomzelle. *Naturwissenschaften* 12, 1131–1137 (1924). doi.org/10.1007/BF01504608
131. Wenzel C, Otto S, Prechtel S, Parczyk K, Steigemann P. A novel 3D high-content assay identifies compounds that prevent fibroblast invasion into tissue surrogates. *Exp Cell Res.* 2015;339(1):35-43. doi:10.1016/j.yexcr.2015.10.003
132. Willers H, Dahm-Daphi J, Powell SN. Repair of radiation damage to DNA. *Br J Cancer.* 2004;90(7):1297-1301. doi:10.1038/sj.bjc.6601729
133. Wolf K, Wu YI, Liu Y, et al. Multi-step pericellular proteolysis controls the transition from individual to collective cancer cell invasion. *Nat Cell Biol.* 2007;9(8):893-904. doi:10.1038/ncb1616

- 
134. Wu JS, Jiang J, Chen BJ, Wang K, Tang YL, Liang XH. Plasticity of cancer cell invasion: Patterns and mechanisms. *Transl Oncol.* 2021;14(1):100899. doi:10.1016/j.tranon.2020.100899
135. Xu B, Fan D, Zhao Y, et al. Three-Dimensional Culture Promotes the Differentiation of Human Dental Pulp Mesenchymal Stem Cells Into Insulin-Producing Cells for Improving the Diabetes Therapy. *Front Pharmacol.* 2020;10:1576. doi:10.3389/fphar.2019.01576
136. Yakavets I, Francois A, Benoit A, Merlin JL, Bezdetnaya L, Vogin G. Advanced co-culture 3D breast cancer model for investigation of fibrosis induced by external stimuli: optimization study. *Sci Rep.* 2020;10(1):21273. doi:10.1038/s41598-020-78087-7
137. Yamada KM, Sixt M. Mechanisms of 3D cell migration. *Nat Rev Mol Cell Biol.* 2019;20(12):738-752. doi:10.1038/s41580-019-0172-9
138. Yu L, Lu M, Jia D, et al. Modeling the Genetic Regulation of Cancer Metabolism: Interplay between Glycolysis and Oxidative Phosphorylation. *Cancer Res.* 2017;77(7):1564-1574. doi:10.1158/0008-5472.CAN-16-2074
139. Zhang J, He X, Ma Y, et al. Overexpression of ROCK1 and ROCK2 inhibits human laryngeal squamous cell carcinoma. *Int J Clin Exp Pathol.* 2015;8(1):244-251.
140. Zhang Z, Nagrath S. Microfluidics and cancer: are we there yet?. *Biomed Microdevices.* 2013;15(4):595-609. doi:10.1007/s10544-012-9734-8
141. Zhao F, Kim W, Kloeber JA, Lou Z. DNA end resection and its role in DNA replication and DSB repair choice in mammalian cells. *Exp Mol Med.* 2020;52(10):1705-1714. doi:10.1038/s12276-020-00519-1

## 8. Abbreviation

°C	Degree Celsius
µg	Microgram
µL	Microliter
µm	Micrometer
mg	Milligram
mL	Milliliter
nm	Nanometer
mm	Millimeter
mM	Millimolar
µM	Micromolar
HCl	Hydrogen chloride
RPMI-1640	Cell culture medium from Roswell Park Memorial Institute
FBS	Fetal Bovine Serum
CO <sub>2</sub>	Carbon dioxide
Pen/Strep	Penicillin- Streptomycin
DMEM	Dulbecco's Modified Eagle Medium
SDS-PAGE	Sodium dodecyl sulfate polyacrylamide Gel electrophoresis
NaCl	Natrium chloride
DNA	Deoxyribonucleic acid
EDTA	Ethylenediaminetetraacetic acid
EtOH	Ethanol
HRP	Horseradish Peroxidase
min	Minute
sec	Second
x g	Times gravity
ECM	Extracellular matrix
ddH <sub>2</sub> O	Double distilled water
NP-40	Nonyl phenoxy polyethoxy ethanol
PBS	Phosphate buffered saline
BSA	Bovine serum albumin
PFA	Perfluoroalkoxy alkanes
rcf	Relative centrifugal Force
rpm	Revolutions per minute
Gy	Grey
RT	Room temperature
o.n	Over night

Cy3	Cyanine 3
ULA	Ultra-low adhesion
NCS	Neocarzinostatin
SD	Standard deviation

## 9. List of figures and tables

### 9.1 Figures

**Figure 1.1:** Model of the regulatory circuit controlling DSB repair pathway choice

**Figure 1.2:** Scheme of heterogenous insight of 3D cultured spheroid

**Figure 1.3:** Current and emerging targets for the management of breast cancer bone metastasis

**Figure 1.4:** Types of cell migration and typical cell types

**Figure 1.5:** Scheme of membrane protein complex of electron transport chain

**Figure 1.6:** FLIM image color scheme

**Figure 1.7:** Determination from metabolic state from NADH lifetimes

**Figure 1.8:** Theoretical positions of fluorescence lifetimes in phasor plot

**Figure 3.1:** Schematic diagram of the ImageJ based plugins for spheroids area measurement

**Figure 3.2:** Schematic diagram of the ImageJ based plugins for invasion area measurement

**Figure 3.3:** Schematic diagram of the ImageJ based plugins for invasion radius measurement

**Figure 4.1:** Transmission light images of different mammary carcinoma cell lines in 2D cell culture.

**Figure 4.2:** Spheroid formation of four breast cancer cell lines MCF-7, BT474, MDA-MB-231 and SkBr3 mono-cultured in ultra-low adhesion plates.

**Figure 4.3:** Spheroid formation of MCF-7, MDA-MB-231 and SkBr3 mono-cultured in 3D CoSeedies™ scaffolds.

**Figure 4.4:** Spheroid formation of breast cancer cell line MCF-7 in scaffold - based 3D VitroGel™ (TheWell Bioscience) matrix.

**Figure 4.5:** HE staining of cryosections of spheroids grown for 15 days on ULA plates (left) or of cell aggregates grown for 9 days in 3D CoSeedis™ scaffolds (right).

**Figure 4.6:** Western blot of EMT markers in mammary carcinoma cell lines MCF-7, BT474, MDA-MB-231, and SkBr3 cultured in 2D and 3D conditions.

**Figure 4.7:** Invasion capability of breast cancer cells after embedding of spheroids / 3D aggregates into Spheroid Invasion Matrix.

**Figure 4.8:** Expression of EMT markers vimentin (58 kDa), N-cadherin (140 kDa) and marker of fibroblast activation,  $\alpha$ -SMA (42 kDa), in BJ1-hTert and HDF fibroblasts cultivated in 2D

**Figure 4.9:** Expression of multi-polar growth in BJ1-hTert and HDF

**Figure 4.10:** Spheroid growth in BJ1-hTert and HDF fibroblasts in ULA plates.

**Figure 4.11:** Spheroid growth in breast cancer cell lines MCF-7, BT474, MDA-MD-231 and SkBr3 in coculture with fibroblast strains BJ1-hTert and HDF.

**Figure 4.12:** Growth curve of 4 mammary carcinoma cell lines in monoculture or coculture with BJ1-hTert and HDF

**Figure 4.13:** Spheroid growth delay after irradiation.

**Figure 4.14:** Spheroid area was determined by image analysis and recorded as function of time after 5 Gy irradiation.

**Figure 4.15:** Foci formation 24 hours post 5 Gy irradiation treatment in MCF-7 monoculture and MCF-7 + BJ1-hTert coculture spheroids.

**Figure 4.16:** Levels of residual 53BP1 foci in MCF-7 monoculture and MCF-7 + BJ1-hTert coculture spheroids.

**Figure 4.17:** Migration behavior of BJ1-hTert, HDF, PDF, GM637 and FH20-2 fibroblasts into RFP-MCF-7 spheroids.

**Figure 4.18:** Migration behavior of BJ1-hTert, HDF, PDF, GM637 and FH20-2 fibroblasts into BT474 spheroids.

**Figure 4.19:** Snapshots of BJ1-hTert fibroblasts migrating into the MCF-7 tag-RFP spheroids.

**Figure 4.20:** (A) Initial position of three tracked fibroblasts (B) Plot of distance of three tracked fibroblasts to the centroid of the spheroid in 100 frames of a movie taken after adding fibroblasts to 1-day old tagRFP MCF-7 spheroids.

**Figure 4.21:** Effects of ROCK inhibitor Y-27632 on the migration behavior of BJ1-hTert fibroblasts.

**Figure 4.22:** Radiation effects on the migration behavior of BJ1-hTert fibroblasts.

**Figure 4.23:** Fibroblast-led invasion of breast cancer cells into Spheroid Invasion Matrix.

**Figure 4.24:** Radiation effects on invasion in fibroblast monoculture and cancer

cell + fibroblast coculture.

**Figure 4.25:** Invasion behavior after irradiation - area occupied by invading cells.

**Figure 4.26:** Schematic diagram of the ImageJ based plugins for invasion radius measurement written by our group.

**Figure 4.27:** Invasion behavior after irradiation - Maximum invasion radius. Maximum invasion radius was measured from spheroid centroid on days 7 and 14 after irradiation with 5 Gy or mock-treatment and embedding.

**Figure 4.28:** Inhibition of fibroblast proliferation by radiomimetic treatment.

**Figure 4.29:** MCF-7 + BJ1-hTert collective invasion model observed by fluorescent life-time imaging microscopy

**Figure 4.30:** Detection of NAD(P)H lifetime in 2D-cultured MCF-7 cells fixed 10 min, 2 h, 24 h and 48 h after 15 Gy X-ray irradiation or mock-treatment.

**Figure 4.31:** Detection of FAD life-time in the 2D-cultured, fixed MCF-7 cells 10 min, 2 h, 24 h and 48 h after 15 Gy X-ray irradiation or mock-treatment.

**Figure 4.32:** Detection of NAD(P)H lifetime in 2D-cultured, fixed BJ1-hTert cells 10 min, 2 h, 24 h and 48 h after 15 Gy X-ray irradiation or mock-treatment.

**Figure 4.33:** Detection of FAD life-time in 2D-cultured, fixed BJ1-hTert cells 10 min, 2 h, 24 h and 48 h after 15 Gy X-ray irradiation or mock-treatment.

**Figure 4.34:** Mitochondria staining of MCF-7 cells with and without 15 Gy X-ray radiation treatment. Cells were fixed 10 min, 2 h, 24 h and 48 h post-irradiation.

**Figure 4.35:** Morphological parameters (mitochondrial particle number, average mitochondrial area and average perimeter of mitochondrial particles) in MCF-7 cells after irradiation with 15 Gy.

**Figure 4.36:** Total mitochondria area in MCF-7 cells after irradiation with 15 Gy.

**Figure 4.37:** Mitochondria staining of BJ1-hTERT cells with and without 15 Gy X-ray radiation treatment.

**Figure 4.38:** Morphological parameters (mitochondrial particle number, average mitochondrial area and average perimeter of mitochondrial particles) in BJ1-hTert cells after irradiation with 15 Gy.

**Figure 4.39:** Total mitochondria area in BJ1-hTert cells after irradiation with 15 Gy.

**Figure S4.1:** Phasor plot analysis of NAD(P)H lifetime in cytoplasm of MCF-7 cells at 10 min, 2 h, 24 h and 48 h after irradiation with 15 Gy.

**Figure S4.2:** Phasor plot analysis of NAD(P)H lifetime in cytoplasm of BJ1-hTert irradiated cells at 10 min, 2 h, 24 h and 48 h after 15 Gy radiation.

**Movie S4.1:** Migration of 3 single fibroblasts into the tagRFP MCF-7 spheroids.

## 9.2 Table

**Table 1.1:** Spectral characteristics and lifetimes of endogenous fluorophores

**Table 3.1:** Antibody dilution conditions for immunofluorescence

**Table 3.2:** Blocking and antibody dilution conditions for Western Blot analysis

**Table 4.1:** Quantification of Foci formation 24 hours post 5 Gy irradiation treatment in MCF-7 monoculture and MCF-7 + BJ1-hTert coculture spheroids.

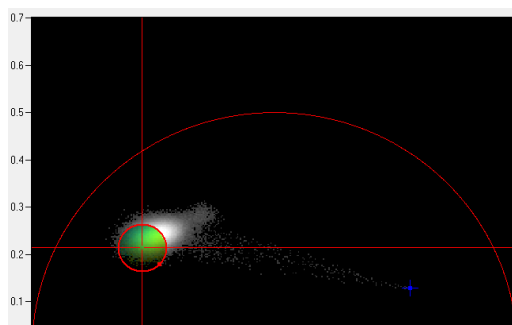
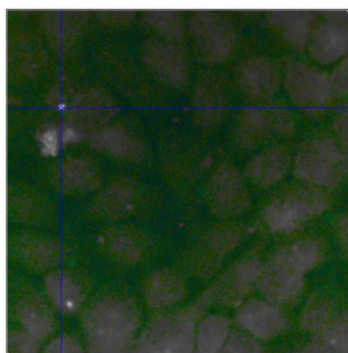
**Table 4.2:** Maximum invasion radius and core radius measured from spheroid centroid on days 7 and 14 after irradiation with 5 Gy or mock-treatment followed by embedding.

**Table 4.3:** Sensitivity of BJ1-hTert and HDF fibroblasts towards treatment with the radiomimetic.

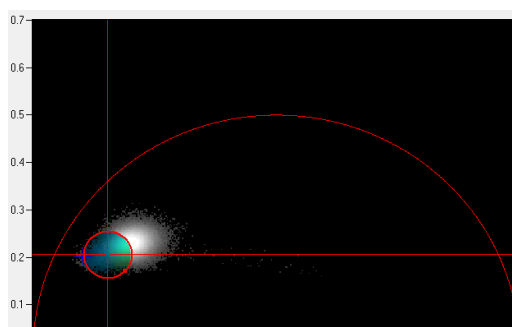
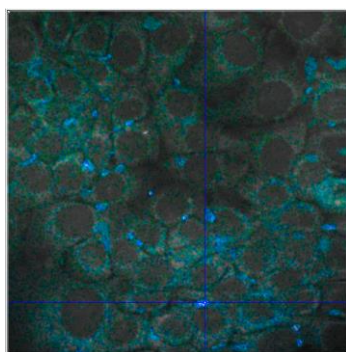
## 10. Appendix

### 10.1 Phasor plots of FLIM data on radiation effects

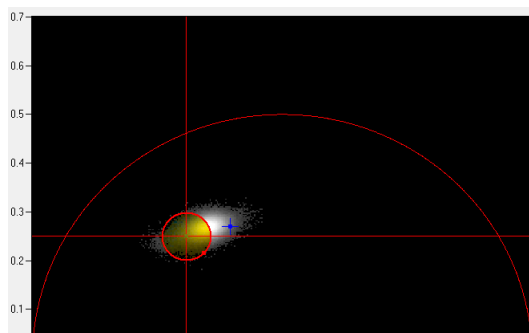
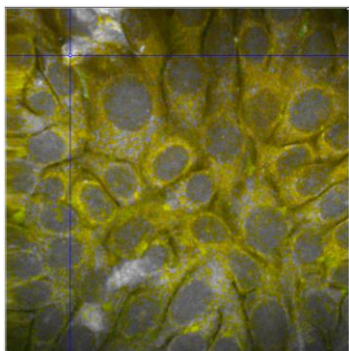
#### 10 min post-irradiation

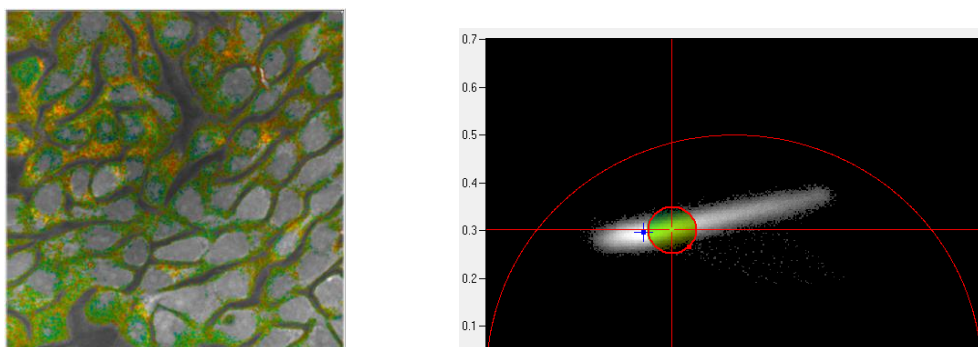


#### 2 h post-irradiation

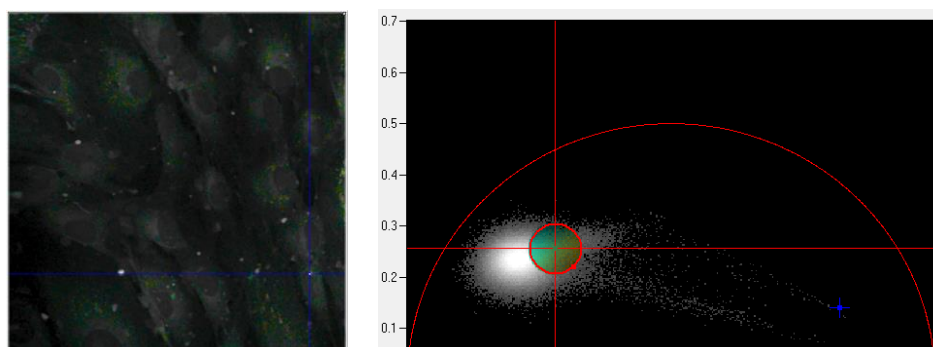
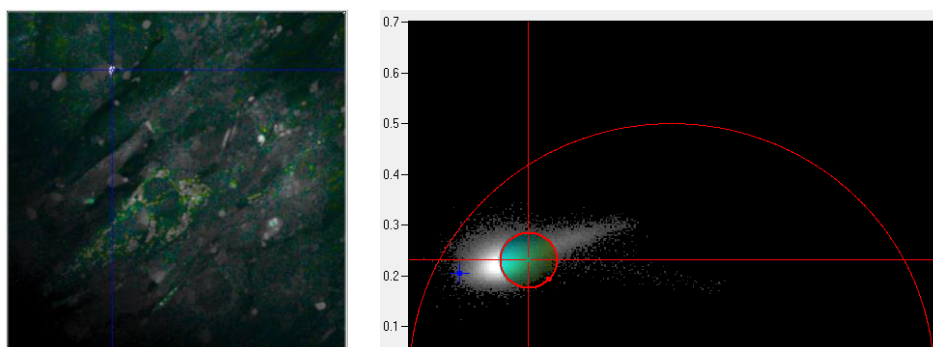


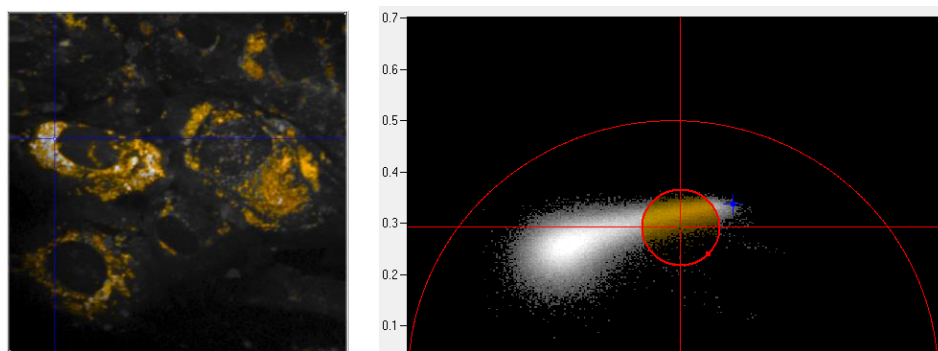
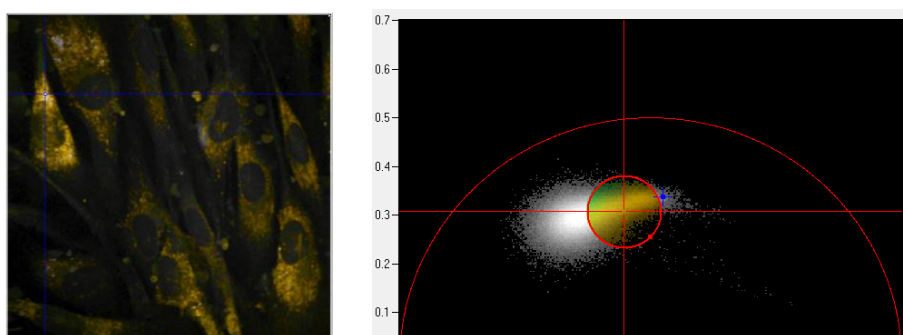
#### 24 h post-irradiation



**48 h post-irradiation**

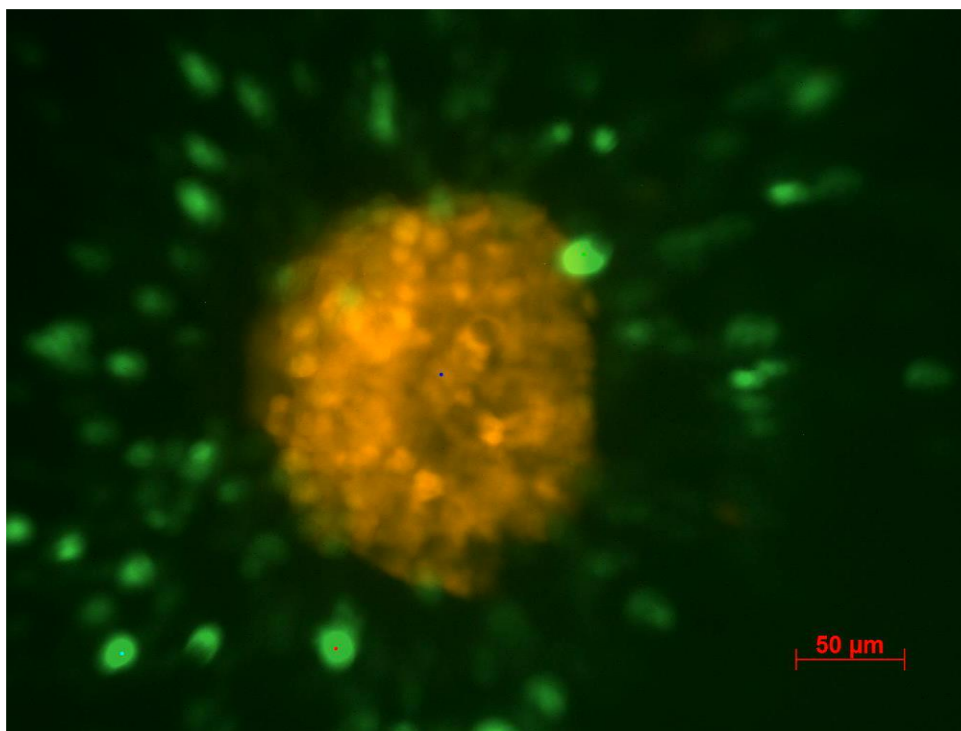
**Figure S4.1:** Phasor plot analysis of NAD(P)H lifetime in cytoplasm of MCF-7 cells at 10 min, 2 h, 24 h and 48 h after irradiation with 15 Gy. Selected regions in the plot reflects the cytosolic NAD(P)H. Blueish color stands for longer lifetime and yellowish for shorter lifetime.

**10 min post-irradiation****2 h post-irradiation**

**24 h post-irradiation****48h post-irradiation**

**Figure S4.2:** Phasor plot analysis of NAD(P)H lifetime in cytoplasm of BJ1-hTert irradiated cells at 10 min, 2 h, 24 h and 48 h after 15 Gy radiation. Selected region in the plot reflects the cytosolic NAD(P)H. Blueish stands for longer lifetime and yellowish is shorter lifetime.

## 10.2 Migration Movie



**Movie S4.1:** Migration of 3 single fibroblasts into the tagRFP MCF-7 spheroids.

## Acknowledgement

There are many who helped me along the way on this journey. I want to take a moment to thank them. This project would not have been possible without the support of many people.

Firstly, I wish to thank my dissertation committee. Without their guidance, I would not have made it. Many thanks to PD Dr. Anna Friedl, my supervisor, who gave me most direct guidance, read my numerous revisions, helped make some sense of the confusions. And she went above and beyond to help me reach my goal. Prof. Dr. Matthias F. Kling, who employed me as a PhD student and, together with Dr. Mihaela Zigman, provided me with additional financial support to finish my studies. Prof. Kling also expanded my knowledge of biological application of optics. Prof. Dr. Heinrich Leonhardt served as a wise committee member and gave me a lot of useful suggestions during the progress of the project.

Second, I deeply appreciate the constant support, encouragement and advice I have received from the colleagues and members of the Friedl lab, especially from the technicians Claudia Böhland and Iris Baur. I also want to thank those students whom I supervised or guided, who did excellent jobs during their training and contributed to the present work. Many thanks to Dr. Christian Siebenwirth, who invested his time and experience to help me solve analyzing and programming problems. I also appreciate the support by members of the Kling lab, especially Marcel Neuhaus, in performing the non-linear microscopy experiments.

I would also like to thank the members of the group of Prof. Dr. Jürgen Popp from the Institute for Physical Chemistry (IPC) of Friedrich-Schiller-Universität Jena, with whom we collaborated on the non-linear microscopy projects. Their experience made our cooperation go smoothly and helped make a breakthrough.

Finally, thanks to my parents and friends: your love and understanding helped me through the dark times. I am grateful for your assistance, understanding and patience. Without you believing in me, I never would have made it.